Conception de cavités optiques à résonance élargie avec des miroirs de Bragg à pas variable

Grigore-Adrian Iordachescu

▶ **To cite this version:**

Grigore-Adrian Iordachescu. Conception de cavités optiques à résonance élargie avec des miroirs de Bragg à pas variable. Autre. Supélec, 2013. Français. NNT : 2013SUPL0021 . tel-00966886

HAL Id: tel-00966886

https://theses.hal.science/tel-00966886

Submitted on 27 Mar 2014

HAL is a multi-disciplinary open access archive for the deposit and dissemination of scientific research documents, whether they are published or not. The documents may come from teaching and research institutions in France or abroad, or from public or private research centers.

L'archive ouverte pluridisciplinaire **HAL**, est destinée au dépôt et à la diffusion de documents scientifiques de niveau recherche, publiés ou non, émanant des établissements d'enseignement et de recherche français ou étrangers, des laboratoires publics ou privés.

N° d'ordre: 2013-21-TH

SUPELEC

Ecole Doctorale EMMA
« Énergie, Mécanique et Matériaux»

THÈSE DE DOCTORAT

DOMAINE : SPI
Spécialité : Photonique

Soutenue le 21 octobre 2013

par

Grigore-Adrian IORDACHESCU

Conception de cavités optiques à résonance élargie avec des miroirs de Bragg à pas variable

Directeur de thèse :	Joël JACQUET	Professeur (SUPELEC)
Composition du jury :		
Président du jury :	Frédéric GENTY	Professeur (SUPELEC)
Rapporteurs :	Arnaud GARNACHE	HDR (Université Montpellier 2)
	Joseph HARARI	HDR (U.M.R C.N.R.S 8520)
Examinateurs :	Véronique BARDINAL	Directeur de Recherche (LAAS-CNRS)
	Guang-Hua DUAN	HDR (Alcatel Thales III-V Lab)
	Paul SCHIOPU	Professeur (UPB Bucharest)
	Delphine WOLFERSBERGER	Professeur (SUPELEC)
Membres invités :	Frederic VAN DIJK	Chercheur (Alcatel Thales III-V Lab)

Acknowledgements

First of all I would like to thank the people at SUPELEC for the warm working environment which was offered to me during the three years of the thesis. I am especially grateful to my supervisor, Prof. Dr. Jöel Jacquet, whose continuous support and advices were vital throughout the entire PhD. My colleague Xunqi Wu was also an inestimable help during our short but intense collaboration. He kindly offered me a very well organized laboratory to conduct my experiences after his departure. Other people who were of real support are my SUPELEC colleagues Nicolas Marsal, Delphine Wolfersberger, Marc Sciamanna and Gilles Berlin.

I would like to thank to all my colleagues in the Continuum team, especially to Yves Houzelle for his technical support and to Guanghua Duan for all the stimulating discussions. Other members taking an active participation in this project were Alain Accard, Arnaud Garnache and Guy Millot.

I would also like to thank the "Conseil Regional de Lorraine" (France) for financial support of this thesis. The work presented here was also financially supported by the French National Research Agency (ANR) through the project ANR-09-NANO-035 01. All partners of this project are kindly acknowledged.

Last, but not least, I would like to thank my parents and my fiancée for their moral support.

Abstract

This thesis proposes a novel method for generating continuum spectra with possible applications in WDM access networks. This new method would allow the development of a simple continuum laser structure with better performances in terms of cost and complexity than those of present supercontinuum sources. In this aim, we will analyze the possibility to broaden the resonant modes of a Fabry-Perot cavity by operating only on the design of one of the cavity's mirrors. The design of the mirror is realized in accordance to a desired reflectivity spectrum. This is made possible by the use of Bragg gratings, for which different synthesis methods have already been developed throughout the literature. First we have considered the conditions which a Bragg grating must satisfy in order to broaden the resonant modes of a resonant cavity. We then simulated the resonant spectra of all simple linearly chirped Bragg gratings (LCBG) in search for one satisfying those conditions. After having only negative results with the linearly chirped gratings, we have decided to generate our own gratings by a synthesis method, namely the genetic algorithm. An active medium is then added inside the cavity formed with such a synthesized grating and its behavior below threshold is simulated. The cavity spectra thus obtained are continuum over 5-15nm.

Some experiments will also be described, but the cavities concerned were not formed by genetic gratings, but with the LCBGs delivered at the beginning of the project. The experiments confirmed the simulations on LCBGs and they were further directed towards finding additional uses for this type of gratings. In function of their support medium, two types of LCBGs have been used: fiber gratings and semiconductor gratings. Two classes of applications found for the resonant cavities thus formed between LCBGs were tunable lasers and resonant amplifiers.

Declaration

I declare that the thesis here submitted is original except for the source materials explicitly acknowledged and that this thesis as a whole or any part of this thesis has not been previously submitted for the same degree or for a different degree.

Table of Contents

Acknowledgements ..... **i**
Abstract ..... **ii**
Declaration ..... **iii**
List of Tables and Figures ..... **v**
Symbols and Abbreviations ..... **ix**

PART 1 – Synopsis in French

1 Introduction **3**
2 Supercontinuum **4**
3 Réseaux à pas linéairement variable **8**
4 Réseaux génétiques **16**
5 Mesures expérimentales **23**
6 Conclusions **26**

PART 2 – Manuscript

1 Introduction **31**
1.1 Optical cavities **31**
1.2 Thesis History **34**
1.3 Outline **36**

2 Continuum spectra **38**
2.1 Supercontinuum **39**
2.1.1 Physics 40
2.1.2 History 42
2.1.3 Applications 43
2.1.4 Limitations 45
2.1.5 Alternatives 46
2.2 Continuum cavity **47**
2.2.1 Physics 48
2.2.2 Origin of the idea 50
2.2.3 Mathematical approximation 51

3 Linearly Chirped Gratings **55**
3.1 Description **56**
3.2 Cavity structures **58**
3.2.1 Hybrid cavity 58
3.2.2 Integrated cavity 59
3.3 Numerical methods for grating analysis **60**
3.3.1 Coupled-mode theory 61
3.3.2 Transfer matrix method 62
3.4 Exact mathematical condition **64**

3.5 Results 68

4 Genetic Gratings 75
4.1 Random gratings 76
4.2 Numerical methods for grating synthesis 77
4.2.1 Genetic Algorithm 79
4.2.2 Discrete Layer Peeling 85
4.3 Results 88
4.3.1 Genetic Algorithm 89
4.3.2 Discrete Layer Peeling 97

5 Measurements 101
5.1 Hybrid cavity 102
5.1.1 Description 102
5.1.2 Tunable Laser 104
5.1.3 Amplifier 108
5.2 Integrated cavity 110
5.2.1 Amplifier 110

6 Conclusions and Perspectives 113
6.1 Conclusions 113
6.2 Perspectives 114

References 116
List of Tables and Figures 121
Symbols and Abbreviations 125
Curriculum Vitae 127

PART 1

Synopsis

Conception de cavités optiques à résonance élargie avec des miroirs de Bragg à pas variable

Résumé de la thèse

1. Introduction

La thèse dont le résumé est présenté dans ce-texte a débuté dans le cadre du projet appelé Continuum, ayant comme but la création d'un laser à résonance élargie. Ce laser était imaginé comme une cavité Fabry Perot (FP) dans laquelle on remplace au moins une des miroirs avec un réflecteur de Bragg spécial, dont le rôle est d'élargir les modes de la cavité. Dans le haut de la Fig. 1 on a fait une comparaison entre la structure d'une cavité FP et la structure imaginée au début du projet Continuum pour un laser à modes élargis. En bas, une comparaison est faite entre leurs spectres idéals. Le premier type de réflecteur de Bragg considéré capable d'élargir les modes résonantes d'une cavité était le réseau de Bragg à pas linéairement variable (LCBG – *Linearly Chirped Bragg Grating*). Avant de présenter les résultats des simulations sur ce type de réflecteur dans le but de créer un laser continu (section 3) on va d'abord présenter dans la section suivante l'utilité d'avoir un tel laser.

Dans la section 4 on va changer notre approche sur le type de réseau de Bragg employé et on va tenter d'élargir les modes résonantes d'une cavité avec des réseaux

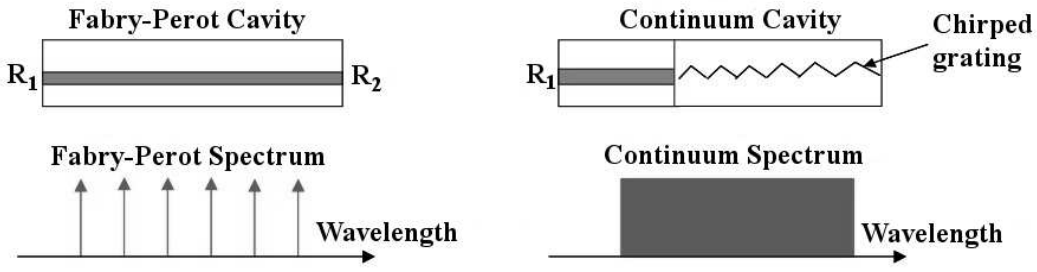

Fig. 1 Comparaison entre une cavité Fabry-Perot (et ses modes résonantes) et une cavité Continuum (et son mode élargi)

à périodes aléatoires. La section 5 décrira quelques nouvelles applications réalisées avec les LCBG de la section 3. Chaque section dans ce résumé corresponde à un chapitre entier du manuscrit original.

2. Supercontinuum

La conception d'une cavité à résonance élargie est le premier pas pour développer une alternative aux lasers supercontinuum (SC). Les SC sont des sources de lumière caractérisées par des émissions spectrales larges et très intenses. Ils ont été découverts pour la première fois dans les années 1970 par Alfano, après avoir injecté un faisceau laser très puissante et ultrarapide dans un cristal fortement non-linéaire. Le faisceau obtenu à la sortie gardait les propriétés modales du laser source utilisé pour sa création, mais il avait le spectre fortement élargie. Une comparaison entre les spectres d'un SC typique et celui du laser source est montrée dans la Fig. 2.

La physique cachée derrière la génération d'un SC n'est pas simple. En fait, sous le nom de «supercontinuum» nous comprenons aujourd'hui un grand nombre de phénomènes non linéaires qui interagissent de façon complexe et qui continuent

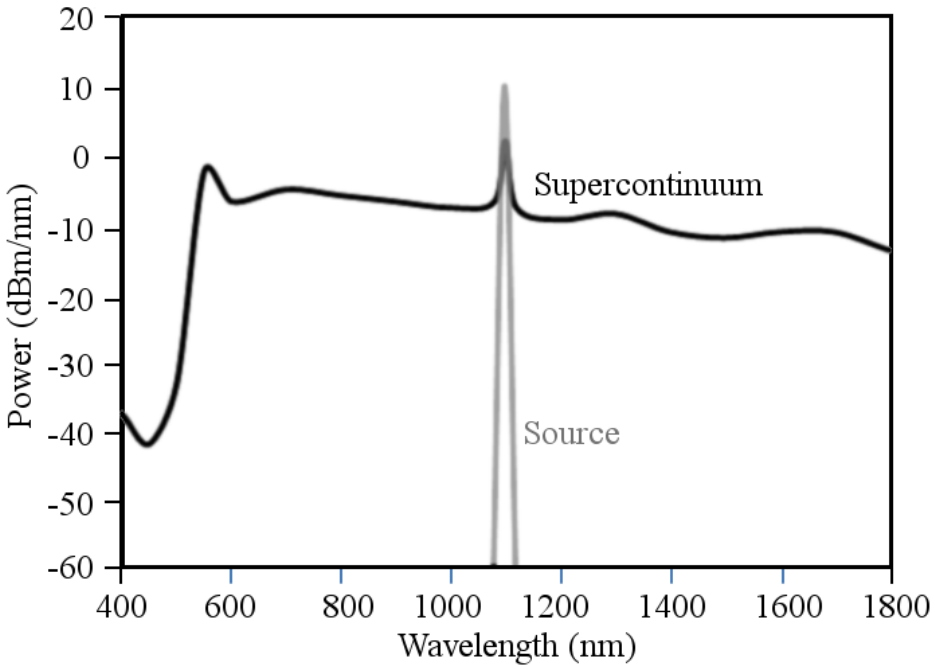

Fig. 2 Comparaison entre un spectre d'un supercontinuum typique et le spectre du laser source utilisé pour sa génération

d’être toujours l'objet de recherches scientifiques - quelques décennies après la découverte du premier SC.

Grâce à leurs spectres uniques, les sources supercontinuum ont été largement utilisées dans de nombreuses applications pendant les dernières décennies, ce qui a fait d'eux l’objet d’une attention croissante de la communauté scientifique. Une liste des applications de recherche nécessitant l'utilisation de sources SC comprend la diffusion Raman inverse, la recherche des processus de vision, des mécanismes de transfert d'énergie dans la photosynthèse et la liste continue.

Le manuscrit de cette thèse fait une description succincte des quatre plus importantes applications d’un SC : la tomographie par cohérence optique (OCT), la compression des pulses ultrarapides, la métrologie des fréquences optiques et dans les télécommunications par multiplexage en longueur d’onde (WDM). Une représentation schématique de la manière dont un supercontinuum peut être utilisé dans un système WDM est représentée dans la Fig. 3. Au lieu d'utiliser une source laser différente pour chaque utilisateur, une approche consistant à utiliser une source laser SC unique qui est ensuite découpée en plusieurs parties par des filtres optiques est préférée en raison de sa plus grande fiabilité. Après découpage, chaque longueur d’onde est modulée en amplitude avec l'information utile et ensuite envoyée à un multiplexeur WDM avant que l’information soit transmise sur la fibre optique vers

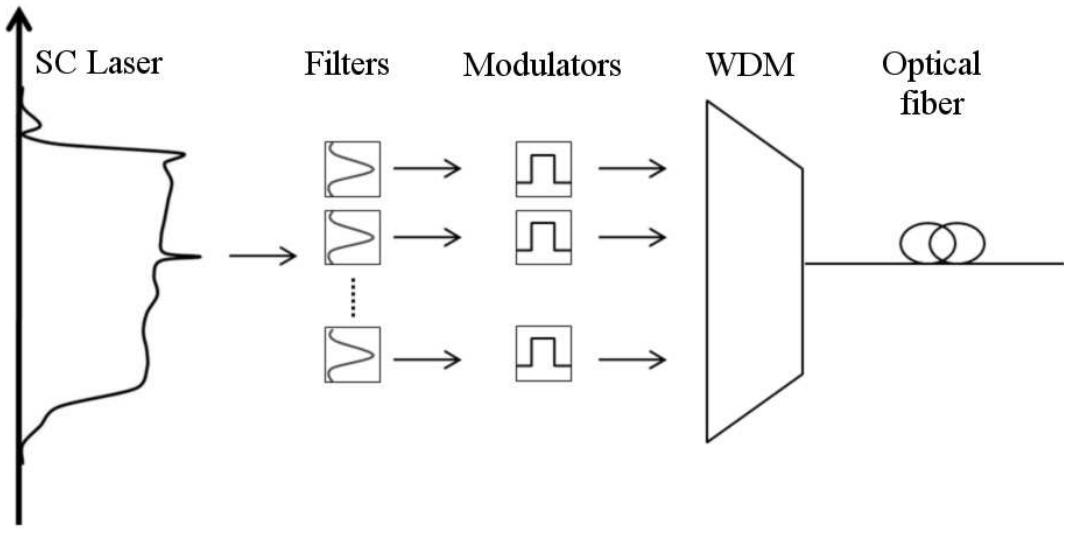

Fig. 3 Schéma de la façon dont une source supercontinuum pourrait être employée dans les applications de télécommunications type WDM.

les utilisateurs.

Malgré leur capacité inégalée à produire une grande largeur de bande à haute puissance, des sources SC ont aussi leurs limites. Leur plus gros problème est leur coût prohibitif. Comparant les composants d'un SC, on s'aperçoit que le laser source de puissance élevée est de loin l'élément le plus coûteux de l'installation. Même si avec l'avènement des SC sur fibre optique les exigences relatives à la source de pompage ont été diminuées en termes de vitesse et de puissance, il va exister toujours une demande pour des sources SC moins chères. Cela est particulièrement vrai lorsque le coût de la source est divisé entre un petit nombre de ménages, comme dans le cas des petits réseaux locaux, comme par exemple les réseaux WDM d'accès.

Un autre inconvénient des sources SC est leur grande taille et la complexité de l'installation. En ce qui concerne cet aspect, c'est également la source de pompage qui est l'élément le plus gênant. Historiquement, la source de pompage la plus utilisée pour la génération de SC étais un laser Ti: saphir. Plus tard, les SC fibrés étaient excités à l'aide des pompes laser à fibre dopée avec Er^{3+} et Yb^{3+}, qui étaient moins chers et moins encombrant que le laser type Ti: saphir.

Un dernier inconvénient de la source SC est sa complexité théorique, puisque une partie des phénomènes qui sont à la base de la génération SC sont toujours étudiés aujourd'hui. Cela rend les simulations thermodynamiques du SC un véritable défi, et par conséquent les simulations numériques utilisées dans la conception d'une telle source laser aussi difficiles.

En raison de son prix élevé lorsqu'il est utilisé dans des applications à petite échelle, comme dans le cas des réseaux locaux déjà mentionnés, certaines alternatives moins chères aux SC ont été recherchées. Pour montrer la difficulté de trouver une telle alternative au supercontinuum, une comparaison est faite dans la Fig. 4 entre les spectres des différentes sources de lumière.

Pour chaque source, seule la puissance utile (la fraction du rayonnement émis qui pourrait être dirigée dans une fibre optique) a été examinée. Tout d'abord, il y a la lampe à arc à xénon, qui imite très bien le spectre naturel du soleil et qui est utilisée dans différents types de dispositifs de projection. Mais la divergence de son faisceau rend la puissance utile de cette lampe loin de la distribution d'énergie d'une source

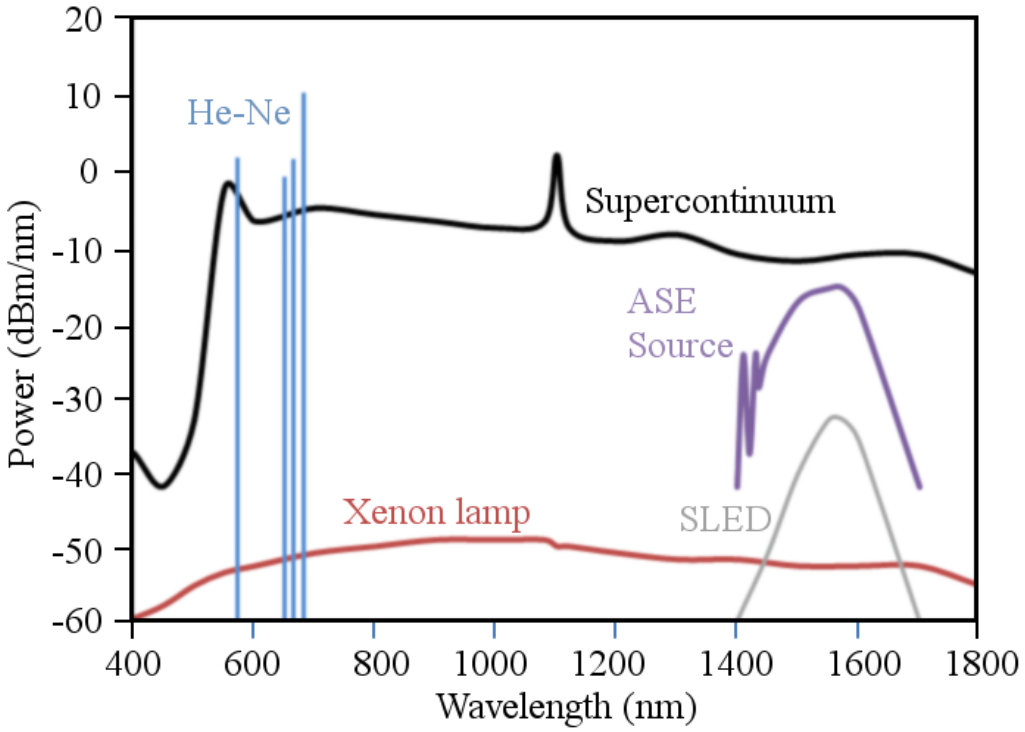

Fig. 4 Comparaison entre les spectres des différents types de sources lumineuses: He-Ne (laser hélium-néon); lampe au xénon; Source ASE (source à l'émission spontanée amplifiée); SLED (diode super-luminescente); Supercontinuum. Pour chaque source, seule la puissance utile a été considéré (le niveau de puissance généré, qui peut être couplé sur une fibre optique)

SC. Au contraire, la lumière dirigée émise par un laser He-Ne possède une puissance utile très élevée, mais une bande passante très étroite.

Les deux seules sources qui peuvent remplacer efficacement une source SC dans les applications à petite échelle sont la diode super-luminescente (SLED) et la source à l'émission spontanée amplifiée (ASE). Toutes les deux fonctionnent sur le même principe lié à la génération et à l'amplification de la lumière spontanée sous le seuil laser. La différence entre eux est que les SLED sont des diodes à semi-conducteurs ayant une structure similaire à celle d'un laser Fabry-Perot, fonctionnant sous le seuil en raison de leur manque de feed-back, tandis que l'émission spontanée dans les sources ASE est réalisée sur une fibre dopée.

Au cours des dernières années, les sources lumineuses incohérentes comme les SLED et les ASE ont eu un certain succès en remplacement du SC dans les réseaux WDM petits en raison de leur faible prix. Premièrement, leur bande passante est suffisamment grande pour couvrir toute la bande C (1530-1565nm). Deuxièmement, leur pouvoir pourrait être amplifié dans la fibre à des valeurs satisfaisantes en utilisant différents types d'éléments dopants. Mais ces sources ont aussi leur

inconvénient qui découle de leur niveau d'incohérence. Leur bruit optique se traduit par un taux d'erreur binaire plus élevé (BER) par rapport à celle d'une source SC.

Dans la recherche d'alternatives moins coûteuses pour le SC, il peut être envisagé qu'une source idéale conçue uniquement pour les petits réseaux WDM d'accès devrait générer un rayonnement cohérent puissant avec une bande passante continue juste assez large pour couvrir entièrement une bande de télécommunications. Le manuscrit de cette thèse va se concentrer sur la recherche d'une telle alternative, en n'utilisant que des phénomènes linéaires.

3. Réseaux à pas linéairement variable

Un réseau à pas linéairement variable (LCG) peut être considéré comme une série de très petits réflecteurs de Bragg uniformes ayant des périodes qui varient linéairement le long de l'axe du réseau. Mathématiquement, cela peut être écrit comme:

$$\Lambda_k = \Lambda_0 + C_\Lambda \cdot z_k \tag{3.1}$$

Dans l'équation (3.1) Λ_k est la période du k-ième réflecteur de Bragg dans le réseau, *C* c'est le chirp du réseau et z_k est la position de début du k-ième réflecteur de Bragg le long de l'axe du réseau. Pour un LCG le chirp *C* est une quantité constante, et il détermine la rapidité de variation de la période de Bragg au long de l'axe. Considérant que chaque réflecteur uniforme de Bragg a une seul période, alors le LCG (qui est la série de tous ces réflecteurs) va avoir une variation d'indice de réfraction comme dans la Fig. 5. Ce type de réseau sera utilisé en suite dans nos simulations. Le but des simulations est de trouver un réseau comme celui affiché

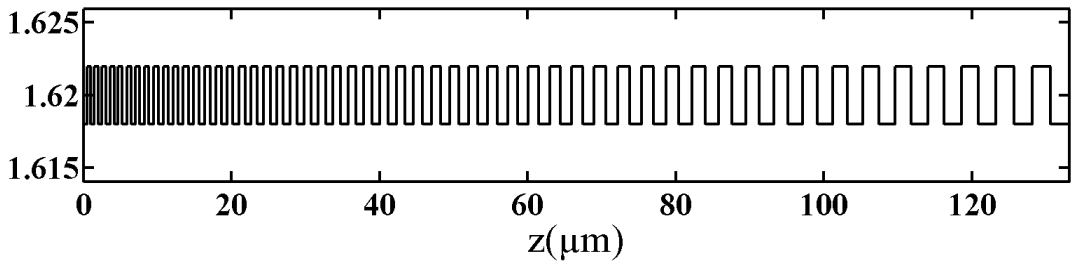

Fig. 5 Variation de l'indice de réfraction (axe des y) d'un réseau à pas linéairement variable réalisé sur fibre. Ce réseau a le *chirp* C=0,04 et le coefficient de couplage k=80cm^{-1}.

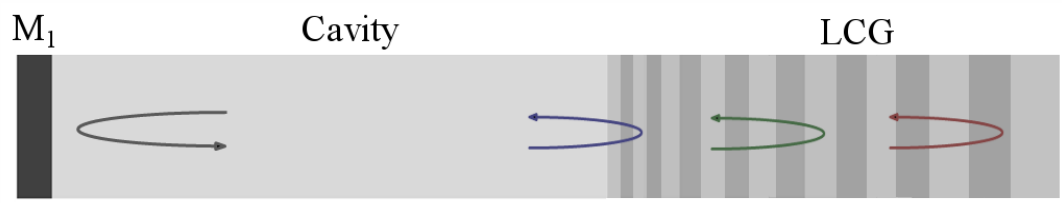

Fig. 6 Représentation des chemins optiques à l'intérieur d'une cavité Continuum: différentes longueurs d'onde parcourent différents chemins optiques, en fonction de la position dans le LCG où leur réflexion a lieu.

dans la Fig. 5 qui peut être employé pour l'élargissement des modes résonant d'une cavité FP. L'élargissement des modes par de tels réseaux semble théoriquement possible si on regarde la Fig. 6. On voit sur cette figure qu'une cavité résonante passive est formée entre un miroir métallique à gauche et un LCG à droite.

A gauche de la cavité dans la Fig. 6, toutes les longueurs d'onde de rayonnement se réfléchissent au même endroit, sur le miroir métallique. Au contraire, dans la partie droite de la cavité, chaque longueur d'onde est réfléchie à un emplacement diffèrent sur le réseau. Les longueurs d'onde plus petites sont réfléchies au début du réseau, correspondant à l'endroit où sont situées les petites périodes de réseau, tandis que les longueurs d'onde plus grand se réfléchissent plus loin à l'intérieur du réseau de Bragg. Ceci est dû au fait que chaque paire de couches formant une période (une couche ayant un indice de réfraction faible, l'autre ayant un indice de réfraction élevé) a une longueur d'onde correspondante qu'elle réfléchit plus que les autre longueurs d'onde, en vertu de sa similitude avec un réseau de Bragg uniforme.

Pour établir la condition mathématique nécessaire à réaliser l'élargissement modale d'une cavité avec un LCG, il faut maintenant regarder la Fig. 7. Dans cette figure, M_1 est un miroir diélectrique simple, introduisant une différence de phase de $\pm \pi$ après réflexion qui, étant indépendante de la longueur d'onde, peut être négligée dans les calculs ultérieurs. Dans la même figure, le décalage de phase aller-retour a été séparé en deux termes, un correspondant au chemin optique à travers la cavité (φ_{FP}) et l'autre à la longueur du trajet moyen du rayonnement dans le réseau de Bragg (φ_{BG}). Dans une cavité résonante la somme des deux est un multiple de 2π pour chaque longueur d'onde λ correspondant à un maximum d'émission (condition de résonance). Dans le cas d'élargissement de modes, φ_{BG} devrait avoir une telle valeur pour que le changement total de la phase aller-retour ($\varphi_{FP} + \varphi_{BG}$) reste un multiple de 2π sur une

large bande spectrale. En autres mots, la variation de φ_{BG} devrait annuler la variation naturelle de φ_{FP} avec λ:

$$d\varphi_{BG}/d\lambda = -d\varphi_{FP}/d\lambda. \tag{3.2}$$

Si (3.2) est vraie pour une bande spectrale assez grande, notre structure va montrer un comportement de continuum. Au lieu d'utiliser des dérivées de phase, l'équation (3.2) peut s'écrire en utilisant une autre grandeur physique appelée le délai de groupe (*GTD*) qui dans certains cas a une interprétation plus intuitive. Le *GTD* est une grandeur caractérisant les systèmes optiques et a une forme mathématique définie par (3.3), où φ est le déphasage introduit par la propagation à travers la structure.

Selon l'endroit où la différence de phase est mesurée par rapport à l'onde incidente, il peut y avoir un *GTD* correspondant à la transmission à travers la structure, et un autre *GTD* correspondant à la réflexion. Parce que tous les réseaux abordés dans le manuscrit fonctionnent comme des miroirs, ce qui sera important pour nous est le *GTD* correspondant à la réflexion sur les réseaux, noté GTD_{BG}.

$$GTD = \lambda^2/(2\pi c)\cdot d\varphi/d\lambda \tag{3.3}$$

Le temps de retard de groupe (*GTD*) d'un rayonnement λ réfléchis sur un réseau est proportionnel à $d\varphi/d\lambda$ comme indiqué en (3.3). On déduit de (3.2) que le *GTD* du réseau doit avoir la même valeur absolue et un signe opposé par rapport au *GTD* de la cavité. Cette condition doit être vraie quel que soit le formalisme de phase adopté. Dans les simulations numériques par la méthode des matrices de transfert (TMM), le décalage de phase d'un rayonnement λ après sa propagation sur une distance z à travers un milieu d'indice de réfraction n est considéré égal à:

$$\varphi(z) = -2\pi nz/\lambda. \tag{3.4}$$

Dans ce formalisme de phase, le GTD_{FP} de la cavité est toujours positif. Il découle de

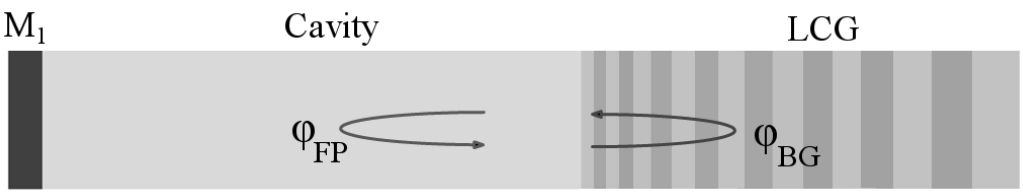

Fig. 7 Représentation d'une cavité résonnante réalisée avec un LCG, dans laquelle le décalage de phase aller-retour totale a été divisé entre le réseau de Bragg (φ_{BG}) et le reste de la cavité (φ_{FP}).

(3.2) que le GTD_{BG} du réseau de Bragg (simulée par TMM) devrait avoir en conséquence un signe négatif dans la bande spectrale souhaitée, si on garde le même formalisme de phase (3.4) partout dans les calculs:

$$GTD_{BG} < 0. \tag{3.5}$$

Le but des simulations présentées par la suite est de trouver un LCG ayant un temps de retard de groupe négatif. Pour trouver cela on a fait varier trois paramètres différents du LCG, dans le but de couvrir l'espace entier des LCG technologiquement réalisables.

Tout d'abords, considérons dans la Fig. 8 l'influence du chirp sur le *GTD* d'un LCFBG de longueur *L=1cm*. Dans la même figure, les valeurs des réflectivités correspondantes sont tracées en bleu. Les deux graphiques séparées correspondent à deux valeurs limites du coefficient de couplage. En haut, il y a le cas d'un réseau avec un coefficient de couplage *k* élevé. Un tel réseau se caractérise par une réflectivité de 100% pour des *chirps* allant jusqu'à 20nm/cm. La réflectivité (ligne bleue) descende au-dessus de cette valeur du chirp. En raison de moins de périodes de Bragg capables de réfléchir une longueur d'onde λ, la somme des réflexions distinctes pour cette longueur d'onde diminue. En ce qui concerne le *GTD*, les réseaux à faible *chirp* ont de nombreuses périodes de Bragg une après l'autre reflétant le même intervalle de bande spectrale. Cela signifie que la longueur d'onde située au centre de cet intervalle spectral ne se déplace pas beaucoup dans le réseau, étant réfléchie au tout début du réseau. Cette réflexion est similaire à celle provenant d'un miroir solide placé près du début du réseau, entraînant une valeur proche de zéro pour le *GTD*. Avec l'augmentation du *chirp* et donc de la largeur de bande, les premières périodes du réseau vont commencer à réfléchir de moins en moins la longueur d'onde correspondante au centre de cet intervalle spectrale. Cela permettra au rayonnement ayant cette longueur d'onde de pénétrer dans le réseau de plus en plus, ce qui augmente la valeur du *GTD*. Cette augmentation va cesser quand le chirp permettra à la radiation centrale d'atteindre le centre du réseau et d'être réfléchie à une position effective $z_{eff} = L / 2$. Augmenter le chirp encore plus au-delà de cette valeur ne modifiera pas le *GTD* correspondant à cette longueur d'onde centrale. En regardant la Fig. 8(b) une forte diminution de la réflectivité comparée au cas précédent peut être constatée, ce qui est dû au faible coefficient de couplage utilisé.

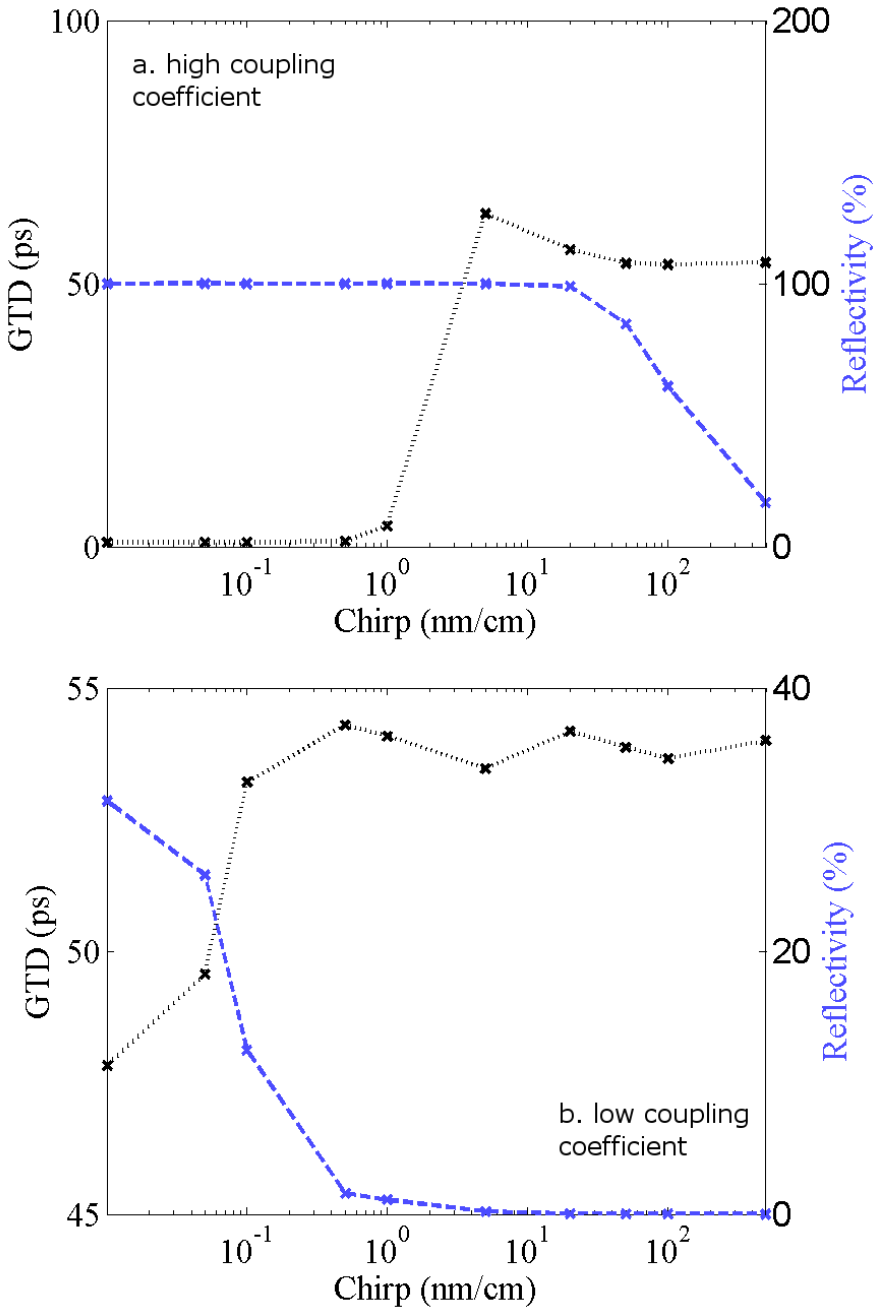

Fig. 8 Influence du *chirp* sur le temps de retard de groupe (*GTD*) d'un LCFBG de longueur L = 1 cm et coefficient de couplage de: a. k = 100cm^{-1} et b. k = 1 cm^{-1}. Le GTD est représenté en noire et la réflectivité en bleue. Toutes les valeurs sont calculées pour λ = 1550 nm au centre de la bande de réflexion du réseau.

En raison de cette faible réflectivité, la longueur d'onde centrale parvient à atteindre tout l'ensemble des périodes de Bragg du réseau, même quand le chirp du réseau est faible. La coordonnée efficace (moyenne pondérée) de la réflexion est très proche de $z_{eff} \approx L / 2$. Lorsqu'on augmente le *chirp*, la bande de réflexion augmente autour de la longueur d'onde centrale, mais le nombre de périodes capables de réfléchir cette longueur d'onde centrale diminue de manière correspondante. A forts *chirps*, seule la période de Bragg centrale situé à $z_{eff}=L/2$ reflétera sa longueur d'onde

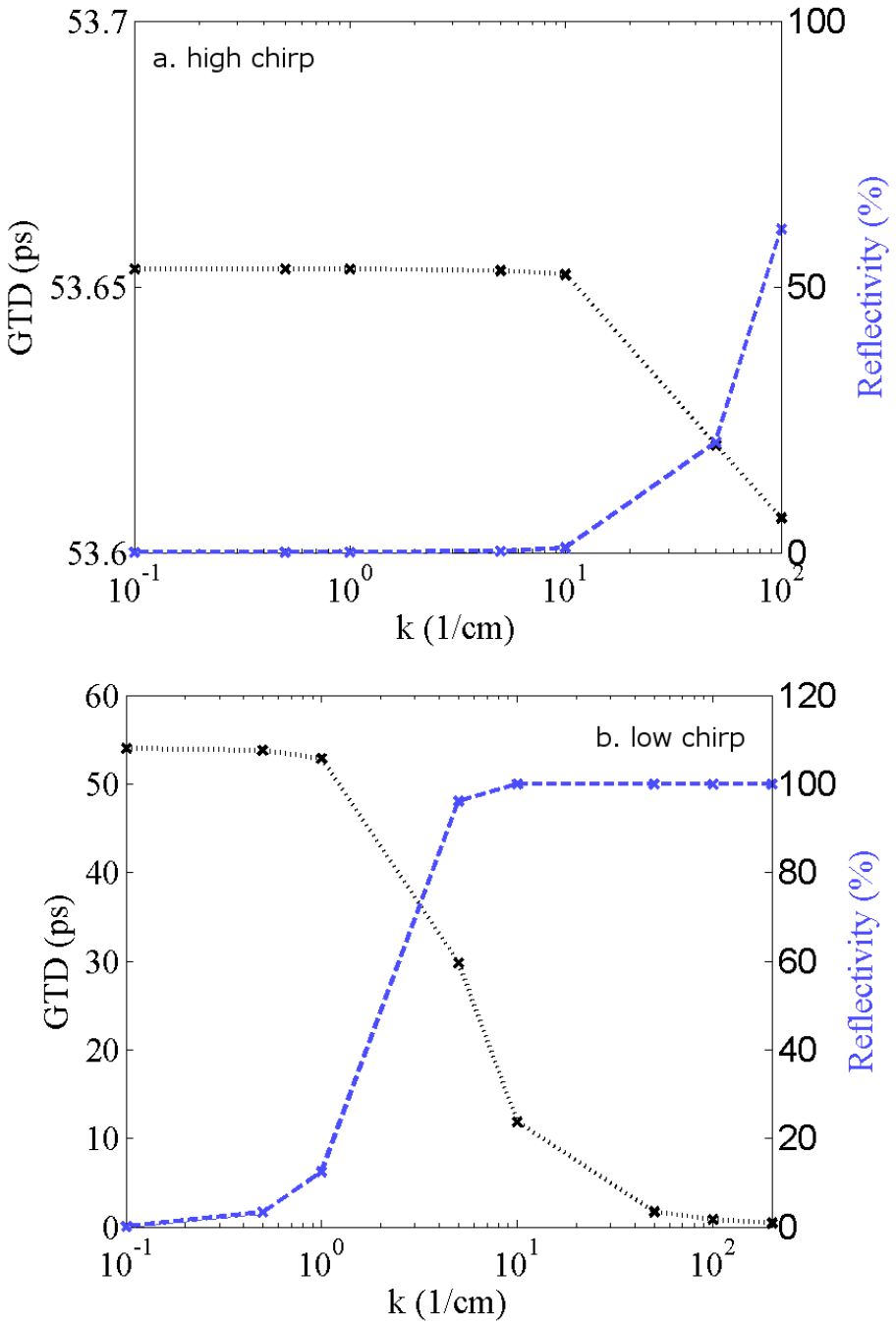

Fig. 9 Influence du coefficient de couplage *k* sur le temps de retard de groupe (*GTD*) d'un LCFBG de longueur *L=1cm* et chirp: a. *C = 100nm/cm* et b. *C = 0,1nm/cm*. Le *GTD* est représenté en noire et la réflectivité en bleue.

correspondante, de manière similaire à ce qui a été décrit précédemment pour un réseau à coefficient de couplage élevé. Cela signifie que pour le cas des réseaux à chirp élevé, le coefficient de couplage a peu d'influence sur le *GTD*.

Le dernier point peut également être remarqué dans la Fig. 9(a), où l'influence du coefficient de couplage sur le *GTD* est analysée dans le cas d'un LCG fibré à *chirp* élevé. Tandis que le coefficient de couplage a été multiplié par 1000, la variation du *GTD* n'a pas dépassé 0,1%. Au contraire, pour le cas d'un réseau à pas faiblement

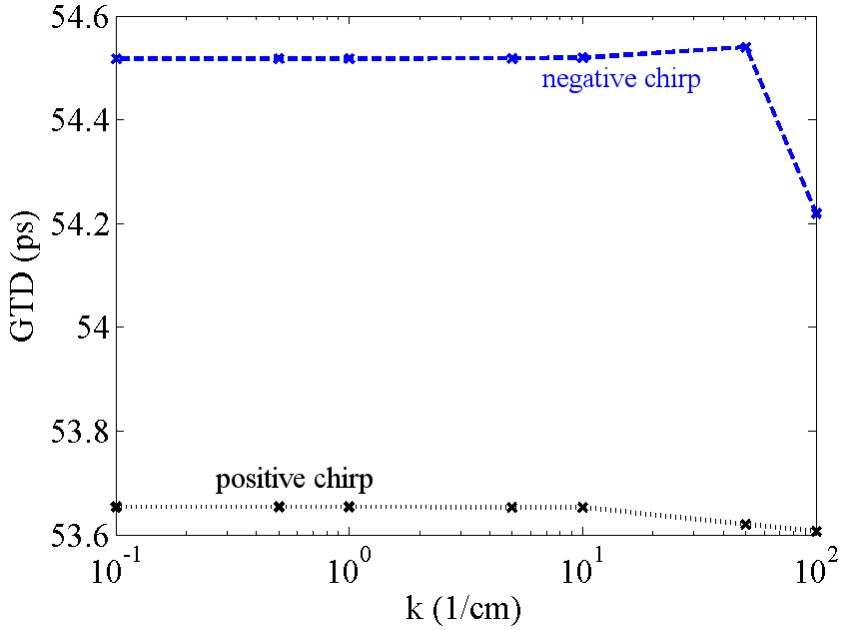

Fig. 10 Influence du signe du *chirp* sur le retard de groupe (*GTD*) d'un LCFBG de longueur *L = 1cm*. La variation du *GTD* avec *k* est étudiée pour le même réseau ayant un chirp *C = 100nm/cm* (noir) et *C= -100nm/cm* (bleu) respectivement.

variable, la variation du *GTD* avec le coefficient de couplage est très importante, comme le montre la Fig. 9(b). Malgré sa grande variation avec *k*, le *GTD* se rapproche seulement asymptotiquement de zéro et il n'arrive pas à atteindre des valeurs négatives. Comme expliqué précédemment, chaque période de Bragg d'un réseau à *chirp* faible sera en mesure de réfléchir la longueur d'onde centrale de sa bande passante. Lorsque le coefficient de couplage est faible, le rayonnement est réfléchi par chaque période de l'ensemble du réseau, présentant une réflexion pour une coordonnée efficace (moyenne) égale à $z_{eff} \approx L / 2$. Lorsque le coefficient de couplage augmente, le rayonnement sera réfléchi de plus en plus par les premières périodes de la grille et donc sa coordonnée efficace de réflexion z_{eff} diminue en conséquence.

Le degré de précision de l'hypothèse physique présentée au début de cette section est testé dans la Fig. 10. Il a été considéré que pour un LCG à chirp positif les longueurs d'onde courtes seront réfléchies avant les plus longues, par les périodes de Bragg situés au début du réseau. Si cela était vrai, en inversant le réseau et créant ainsi un LCG à chirp négatif, les longueurs d'onde plus grandes seront réfléchies avant les plus courtes. La modification de la dérivé de la phase créée après ce renversement du réseau doit se réfléchir sur le *GTD* de la longueur d'onde centrale. Mais comme on le

remarque dans la Fig. 10, une petite différence de 1 picoseconde a été obtenue en faisant tourner un réseau fibré de *chirp C = 100nm/cm* et longueur *L = 1cm*. Cette petite différence démontre le changement de la phase supposé initialement, mais nous montre aussi que la valeur de cette variation n'est pas suffisante pour aboutir à un *GTD* négatif et obtenir l'effet continuum.

La dépendance du *GTD* (calculée pour la longueur d'onde centrale) en fonction de la

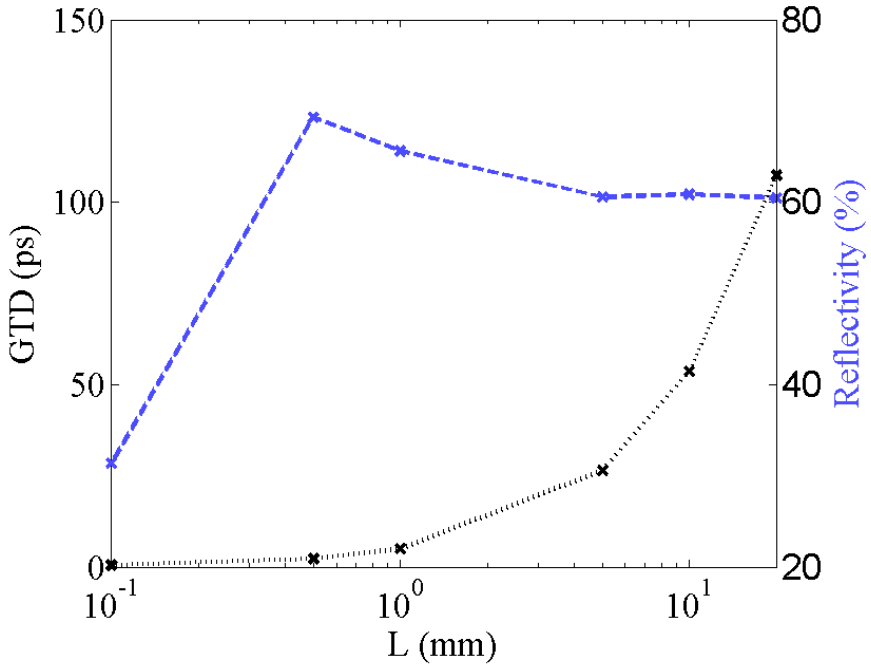

Fig. 11 Influence de la longueur du réseau sur le temps de retard de groupe (noir) et la réflectivité à la longueur centrale (bleu) d'un LCG fibré de chirp *C=100nm/cm* et coefficient de couplage $k=100cm^{-1}$.

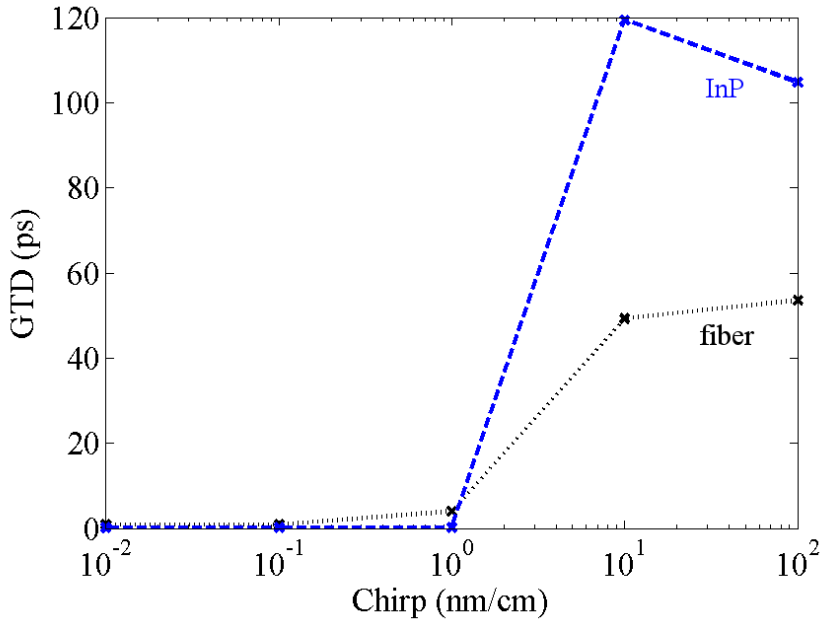

Fig. 12 Influence du milieu du réseau sur le temps de retard de groupe (*GTD*) d'un LCG de longueur *L=1cm*. Le réseau intégré est représenté en bleu, tandis que le LCG fibré est en noir. Un coefficient de couplage de $1000cm^{-1}$ a été utilisé pour le réseau sur InP, tandis que pour le réseau fibré un $k=100cm^{-1}$ a été utilisé.

longueur du réseau est représentée sur la Fig. 11. Au début, l'allure de la réflectivité ne semble pas très intuitive. A partir d'une certaine longueur du réseau, la réflectivité va commencer à diminuer avec la longueur. Cela arrive parce que nous augmentons le nombre de périodes en ajoutant de petites périodes de Bragg à gauche et des grandes périodes à droite. Les périodes de Bragg ainsi ajoutées peuvent réfléchir à nouveau la longueur d'onde centrale, mais cette fois en opposition de phase avec les périodes initiales du réseau. Quant au *GTD*, en augmentant la longueur, on va toujours pousser plus loin la position de la coordonnée efficace de réflexion $z_{eff} \approx L/2$.

Les graphiques présentés dans cette section n'affichent les valeurs du *GTD* que pour certains cas limites de réseaux de fibre optique (chirps élevés vs chirps faibles, *k* élevé par rapport à *k* faible, etc). D'autres cas intermédiaires (comme pour les chirps et les coefficients de couplage moyens) ont été négligés à force de ne rien apporter de nouveau aux observations déjà faites. Les mêmes séries de simulations ont été faites pour le cas de réseaux sur InP sans meilleurs résultats (Fig. 12). La technologie intégrée apporte la possibilité d'utilisation de coefficients de couplage élevés. Grâce à cette propriété, des plus petites *GTD* vont être obtenus pour le cas de petits chirps, lorsque la réflexion est réalisée dans la proximité du début du réseau ($z_{eff} \approx 0$). Comme InP présente un indice de réfraction plus élevé par rapport au cas fibré, son *GTD* sera aussi beaucoup plus élevé lorsqu'on augmente le chirp et on permet une réflexion effective proche de $z_{eff} \approx L/2$. Ceci est causé par une augmentation du chemin optique de la lumière, même si la réflexion est réalisée à la même coordonnée physique dans les deux milieux.

Les discussions de cette section sur le *GTD* sont des analyses originales du comportement de la lumière dans un LCG. Malheureusement, notre objectif de trouver un réseau réfléchissant ayant un *GTD* négatif n'a pas été atteint. C'est peut-être à cause du nombre très réduit de degrés de liberté offert par LCG, ou ça peut être causé par une limite physique fondamentale inhérente au processus de réflexion.

4. Réseaux génétiques

Alors que nous avons cherché une solution au problème d'un réseau à GTD négatif dans la section précédente, nous nous sommes limités seulement à l'espace des LCG

technologiquement disponibles. La dépendance du GTD en fonction de trois paramètres de fabrication a été calculée et expliquée. Il a été observé que, peu importe les paramètres utilisés, il n'a jamais été possible d'obtenir un GTD négatif dans le centre de la bande de réflexion d'un LCG. L'idée de cette section est d'étendre notre recherche indéfiniment à tout type de structure réfléchissante réalisée par la variation de l'indice de réfraction. Ce type de structure pour laquelle il n'existe pas de fonction analytique simple reliant une couche du réseau avec les autres couches sera appelé un réseau aléatoire. Comme le montre la Fig. 13 il peut y avoir trois types de réseaux aléatoires, en fonction du paramètre qui est considéré comme aléatoire. Le type qu'on va utiliser dans nos simulations prochaines est le premier d'entre eux, le réseau à épaisseur aléatoire.

Dans le but de générer un tel réseau aléatoire, on a illustré dans le manuscrit original plusieurs méthodes numériques, appelées méthodes de synthèse. On a choisi l'algorithme génétique comme méthode préférée et on l'a adapté à notre cas spécifique. Cet algorithme génère automatiquement une population initiale de *N*

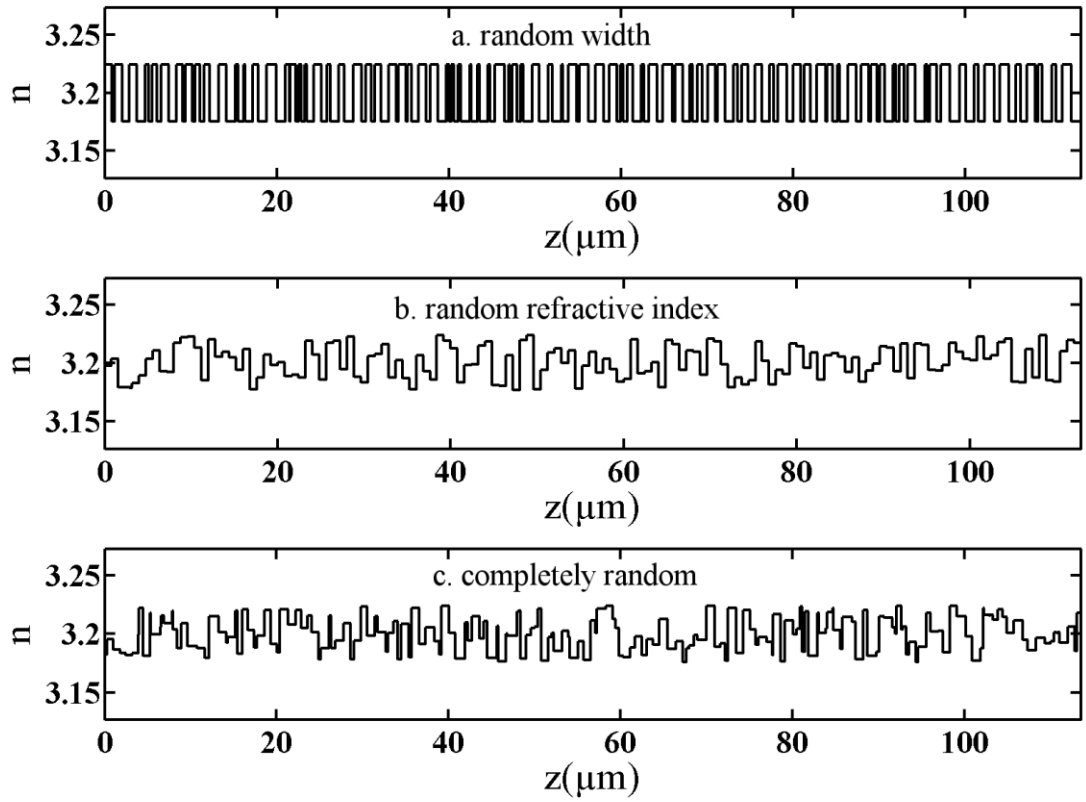

Fig. 13 Trois exemples de différents types de réseaux aléatoires sur InP: a) à épaisseur aléatoire, dans lequel la largeur de chaque couche est aléatoire, b) à indice aléatoire, dans laquelle l'indice de réfraction de chaque couche a une valeur aléatoire, c) complétement aléatoire, dans lequel à la fois la largeur et l'indice de réfraction de chaque couche sont aléatoires

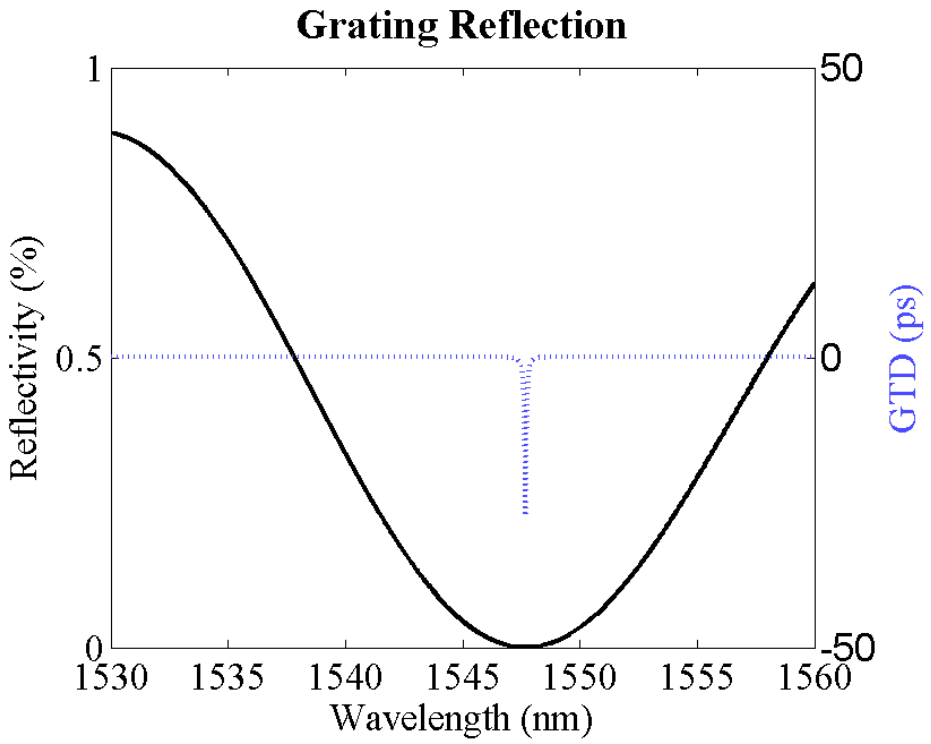

Fig. 14 Spectre d'un réseau génétique obtenu après 10 itérations par un algorithme génétique qui cherchait un réseau de 200 couches d'InP ayant un *GTD* négatif. L'amplitude de la réflectivité est représentée en noir, tandis que le GTD est en bleu.

réseau ayant le même nombre de couches *M* et mélange leurs caractéristiques physiques dans le but d'obtenir un super-réseau, meilleur par rapport à tous les réseaux initiaux. Une description complète de notre méthode de synthèse peut se trouver dans le manuscrit de thèse. Dans ce résumé on va directement passer à décrire les résultats obtenus par cette méthode. Tous les réseaux aléatoires obtenus avec un algorithme génétique on va les appeler réseaux «génétiques».

Le premier exemple est celui d'un réseau obtenu quand l'algorithme génétique avait comme seul contrainte la synthèse d'un réseau à *GTD* négatif n'importe où dans la bande C (1530-1565nm). Aucune condition n'était mise sur la réflectivité. Dans ce cas-là un exemple typique du spectre d'un réseau génétique synthétisé est affiché dans la Fig. 14. Ce spectre appartient à un réseau de M=200 couches trouvé par un algorithme génétique après dix itérations. La population initiale utilisée par l'algorithme est N = 1000. On remarque que la valeur négative élevée de *GTD* = *−28ps* correspond à une région de réflectivité nulle. En fait, chaque fois que l'algorithme tente la synthèse d'un réseau à *GTD* hautement négative, le spectre de ce réseau va avoir une région correspondante de réflectivité nulle. Il devient ainsi

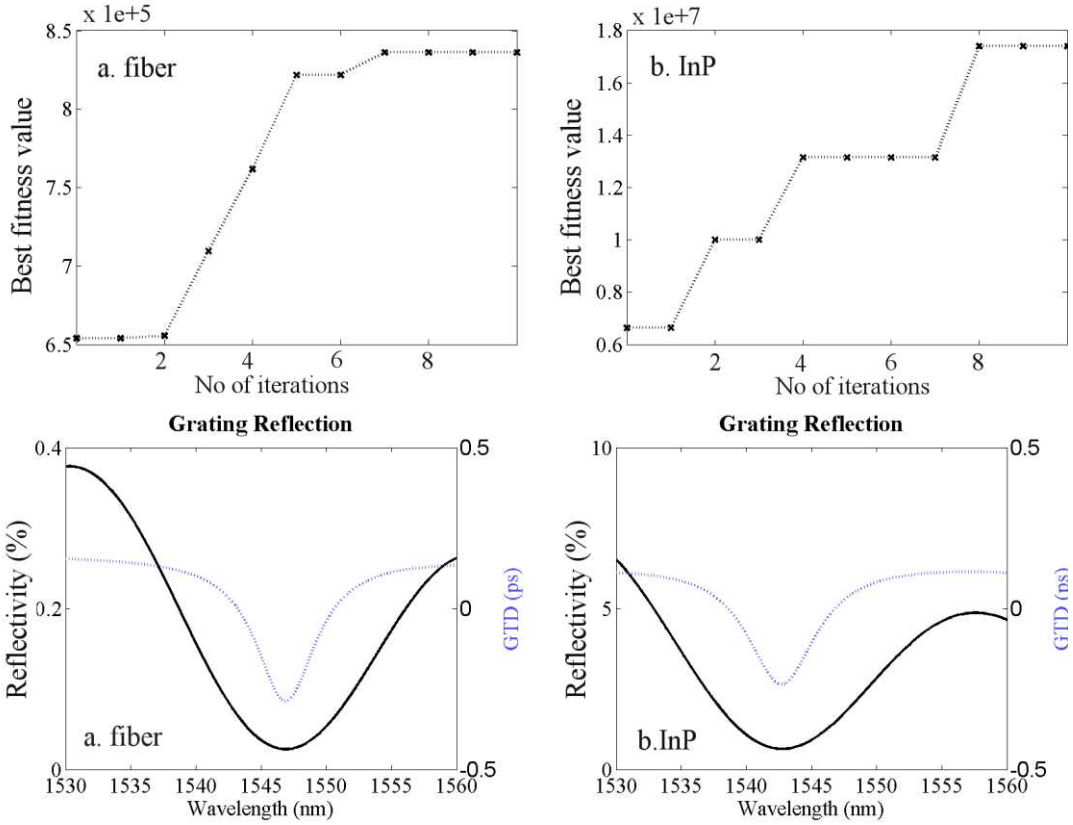

Fig. 15 Comparaison entre l'efficacité de l'algorithme génétique pour le cas de deux populations différentes de réseaux : (a) fibrés et (b) intégrés. Les deux populations sont composées de réseaux de M = 200 couches. En haut, l'évolution de la meilleure valeur de fitness en fonction du nombre de nouvelles générations créées par l'algorithme. En bas, les meilleurs spectres obtenus dans la dixième nouvelle génération.

évident que les deux conditions (*GTD* négatif et réflectivité élevée) sont opposées. On a donc réécrit l'algorithme pour essayer de concilier les deux conditions mutuellement opposées.

Figure 15 montre une comparaison de l'évolution de cet algorithme «conciliant» pour deux populations de réseaux ayant les mêmes caractéristiques générales, à l'exception du matériel et donc de leurs coefficients de couplage *k*. A la gauche de la Fig. 15 on a le cas des réseaux fibrés, et à la droite le cas des réseaux sur InP. La valeur maximale du coefficient de couplage a été utilisée dans les deux cas, ce qui correspond à une valeur de k = 100cm^{-1} pour les réseaux fibrés et à une valeur de k = 1000cm^{-1} pour les structures sur InP. La valeur de fitness (appelée «fitness value» en anglais) exprime numériquement combien chaque réseau se rapproche des performances ciblées par l'algorithme génétique. La valeur fitness maximale qui est affichée dans les graphiques supérieurs de la Fig. 15 montre la performance du

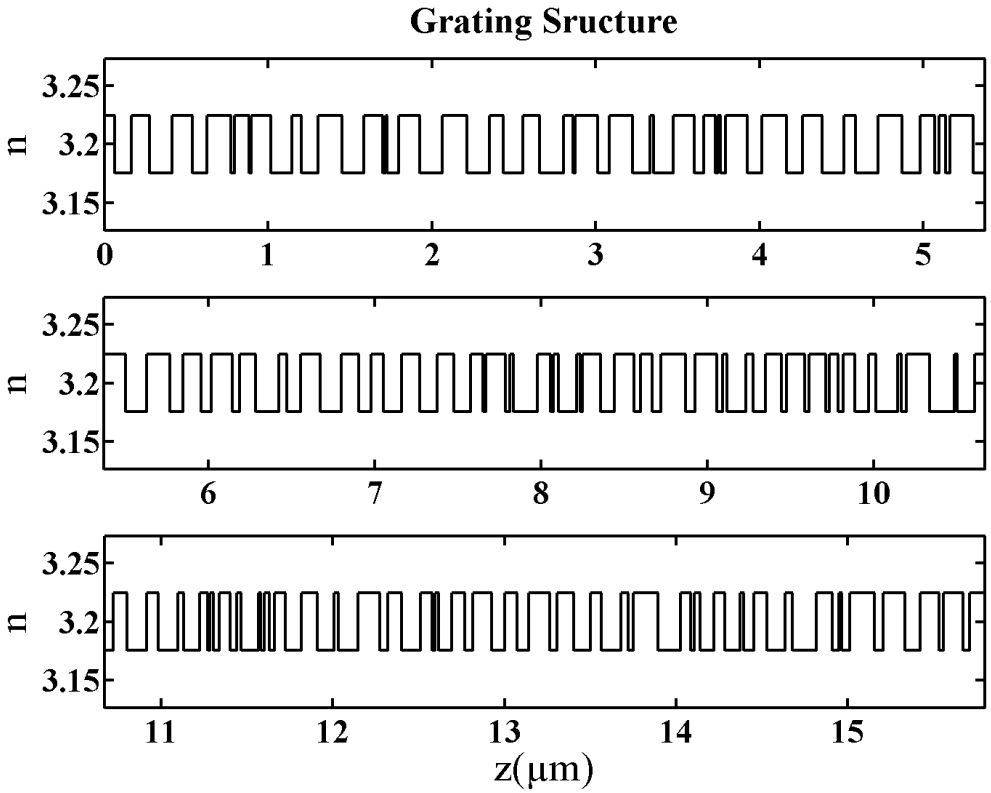

Fig. 16 Variation de l'indice de réfraction du réseau génétique de 200 couches, dont le spectre a été tracé sur la Fig. 15(b)

meilleur réseau à chaque pas de l'algorithme. Il est tout à fait normal que cette valeur va augmenter avec le nombre d'itérations de l'algorithme.

En comparant les deux graphiques en haut, il est aussi évident que la valeur maximale initiale de fitness (lorsque le nombre d'itérations est égal à zéro) dans la population InP est dix fois plus élevée que la valeur maximale de fitness initiale dans la population de réseaux fibrés. En comparant ensuite l'évolution de cette valeur pour dix générations consécutives de réseaux génétiques, il devient également évident que de bien meilleures performances sont obtenues en appliquant l'algorithme dans le cas de réseaux intégrés sur InP. Enfin, en bas de la figure, les meilleurs spectres obtenus à la $10^{ème}$ génération sont affichés côte à côte dans les deux cas. Il est clair que ce qui décide en faveur des structures sur InP est leur plus grande amplitude de la réflexion causée par leur coefficient de couplage beaucoup plus élevé. Par contre, les valeurs du GTD sont très similaires dans les deux cas. Le léger avantage obtenu par le réseau fibré est expliqué par son coefficient de couplage inférieur. On a déjà montré dans la Fig. 9 qu'il existe une corrélation inverse entre le coefficient de couplage et les valeurs absolues du GTD. Mais en ce qui concerne notre préférence pour les réseaux

sur InP, la grande augmentation de la réflectivité rend les pertes dans le *GTD* moins importantes.

La structure du réseau dont le spectre a été montré dans le bas de la Fig. 15 b) est affichée dans la Fig. 16. On voit le caractère aléatoire des dimensions de chaque couche du réseau. Une autre façon de présenter le spectre de réflectivité de ce réseau (autre que celle utilisée en Fig. 15) est en remplaçant le *GTD* directement avec la différence de phase après réflexion, avec laquelle il est lié par l'équation (3.3). Cette représentation est utilisée dans la Fig. 17 (a), où la ligne bleue représente la différence de phase du rayonnement réfléchi de longueur d'onde λ par rapport au rayonnement de longueur d'onde λ_0 = 1530nm, considéré comme référence. A titre de comparaison Fig. 18 (a) nous montre une représentation analogue du spectre de réflexion, mais pour un réseau de Bragg uniforme de 100 périodes (200 couches) ayant le même coefficient de couplage k = 1000cm^{-1}. On s'aperçoit que la phase du

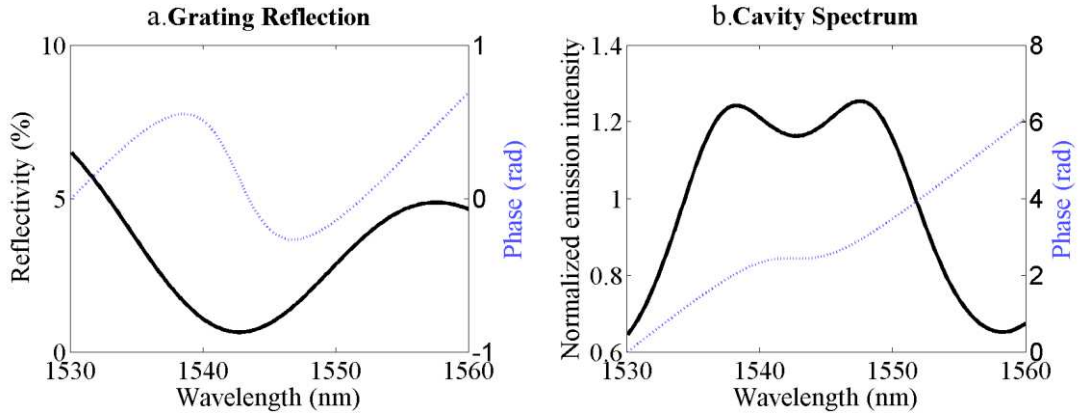

Fig. 17 Spectre de réflexion d'un réseau génétique de 200 couches et l'émission d'une cavité « continuum » utilisant ce réseau comme miroir.

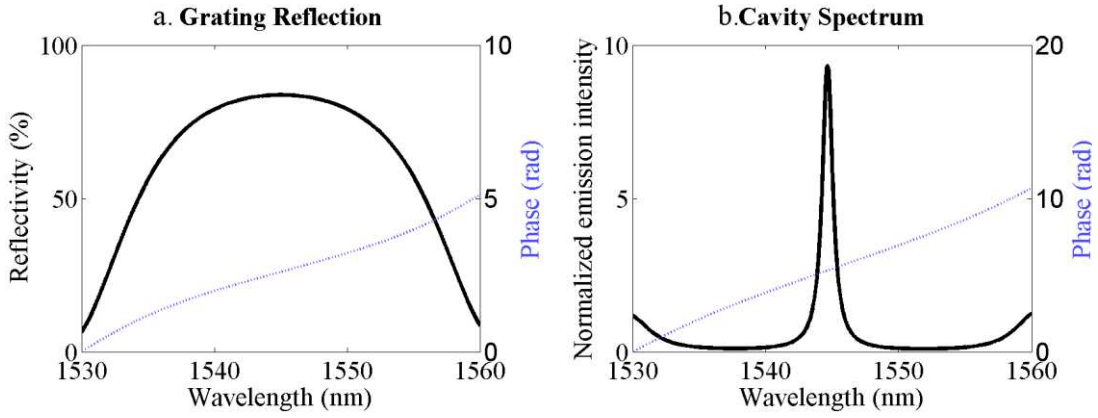

Fig. 18 Spectre de réflexion d'un réseau uniforme de Bragg sur InP à 200 couches (100 périodes) et l'émission d'une cavité résonante utilisant ce réseau comme miroir. Le coefficient de couplage du réseau est *k=1000cm^{-1}*.

réflecteur de Bragg uniforme est uniformément croissante avec la longueur d'onde, pendant que sur le graphique du réseau génétique on voit un intervalle de $\Delta\lambda = 8nm$ centré à 1543nm dont la phase est descendante. Cet intervalle correspond à la région de *GTD* négatif de la Fig. 15 (b). Dans les exemples évoqués ci-dessus, dix itérations de l'algorithme ont été considérées suffisantes, puisqu'après ce nombre de répétitions tous les nouveaux réseaux générés commencent à avoir une structure de couches très similaire. Poursuivre le calcul n'aurait pas donné des valeurs de fitness très différentes.

Le réseau représenté dans la Fig. 16 est ensuite utilisé en tant que miroir dans une cavité résonante. Le feed-back est assuré de l'autre côté de la cavité par un miroir métallique à haute réflectivité ayant un coefficient de réflexion égal à R = 0,9. Pour une longueur spécifique de la cavité résonnante (lorsque la variation de phase de la cavité avec λ est annulée par la variation de phase du réseau) la structure entière a un spectre d'émission normalisé comme celui de la Fig. 17(b). Cette longueur spécifique dépend de la valeur négative du *GTD*. Dans ce cas on a un *GTD* égal à −0235ps, ce qui correspond à une longueur calculée de la cavité résonante égale à $L_0 \approx 11\mu m$. C'est ainsi cette longueur de la cavité qu'on a utilisé pour la simulation de la Fig. 17(b). En gardant la même longueur de la cavité mais remplacent le réseau de Bragg synthétisé par le réseau uniforme (UB) dont le spectre est affiché en Fig. 18 (a), le spectre de la cavité devient comme dans la Fig. 18(b).

Ce qui peut également être remarqué dans la Fig. 17(b) est la cessation presque complète de la variation de phase entre 1539nm et 1547nm, l'intervalle dans lequel le *GTD* négatif du réseau annule la *GTD* positif du reste de la cavité. En d'autres termes, la phase aller-retour de la cavité se maintient constante sur cette bande passante de 8nm parce que la croissance naturelle de la phase aller-retour avec λ est compensée par une baisse similaire de la phase après la réflexion sur le réseau. Il peut être également observé que la région du *GTD* négatif s'approche des deux maxima de réflectivité ayant un *GTD* positif, ce qui produit l'élargissement de la bande spectrale d'émission jusqu'à une valeur de 15 nm dans la Fig. 17(b).

Les spectres d'émission normalisés qui ont été présentés dans les Fig. 17(b) et 18(b) ont été simulés en dessous du seuil, considérant un milieu actif placé à l'intérieur de la cavité. Le milieu actif est supposé avoir une émission spontanée uniforme sur

toutes les longueurs d'onde. L'interférence provoquée par les allers retours consécutifs de cette émission à travers la cavité génère les spectres des deux figures. Le coefficient de gain α du milieu est considéré égal à zéro. Des différentes formes du coefficient de gain peuvent être imaginées pour que la petite vallée dans la Fig. 17(b) formée dans la région du *GTD* négatif soit égalisée au niveau des deux sommets environnants.

5. Mesures expérimentales

L'idée initiale du projet était basée sur les cavités résonnantes formées avec des LCG. Les simulations de la section 3 ont déjà montré qu'il n'y a aucun moyen de produire un spectre d'émission continu en utilisant un LCG en conjonction avec une cavité résonante, contrairement à l'hypothèse initiale du projet. On a retrouvé plus tard dans

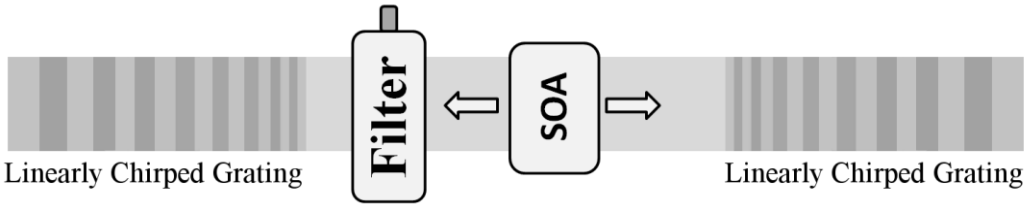

Fig. 19 Schéma d'un laser accordable formé entre deux LCG. A l'intérieur de la cavité un filtre est utilisé pour configurer manuellement la longueur d'onde désirée.

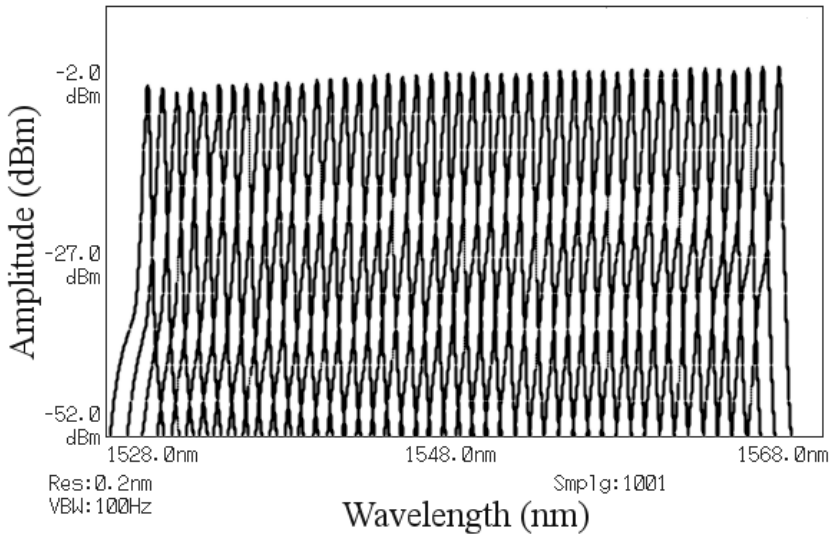

Fig. 20 Spectres d'émission superposées obtenues en ajustant manuellement le filtre de la Fig. 19 pour les différentes longueurs d'onde de la grille ITU.

la section 4 que seul un certain type de structure de couches aléatoires, généré par un algorithme génétique, a pu élargir le spectre d'émission d'une cavité Fabry-Perot. Malgré cette constatation ultérieure, il n'a pas été possible d'obtenir un prototype réel de ces réseaux synthétisés en temps voulu, et donc dans la partie expérimentale du projet on a essayé plutôt de trouver de nouvelles applications pour les LCG déjà livrés.

On va commencer par une première application originale trouvée pour les cavités résonnantes construites avec des LCG. D'abord nous avons essayé d'imaginer une façon originale de déplacer le spectre d'émission d'une cavité résonnante. La structure de la Fig. 19 a ainsi été créée. Le filtre, ayant une bande passante de 1nm à −3dB, a comme rôle de régler manuellement la longueur d'onde émisse à toute valeur désirée contenue à la fois dans la bande de réflexion du réseau et aussi dans le domaine de fréquences du filtre. La bande de réflexion d'un réseau était typiquement l'intervalle 1530-1570nm, alors que le domaine de variation du filtre était composé de l'intervalle 1525-1565nm. L'intersection des deux sera alors le domaine spectral de 1530-1565nm. En faisant tourner manuellement le bouton de réglage du filtre, le spectre sera donc centré sur une longueur d'onde de ce dernier intervalle. Une superposition des spectres obtenus après les ajustements successifs du bouton du filtre est représentée dans la Fig. 20.

L'écartement de fréquence entre deux pics consécutifs dans la Fig. 20 est 50GHz. Chaque pic a été spécialement choisi pour correspondre aux fréquences du peigne ITU utilisé dans les communications WDM en bande C. Chaque spectre séparé dans la Fig. 20 a été enregistré par un analyseur de spectre optique avec un échantillonnage de 1000 points dans une fenêtre d'observation de 40nm.

Une deuxième application originale est représentée par un amplificateur résonant. Cet amplificateur sera constitué d'un SOA placé entre deux LCG de 50% réflectivité comme dans la Fig. 21. Un laser externe de différentes amplitudes et longueurs d'onde est injecté dans cette cavité. De l'autre côté de la cavité, le signal de sorti est mesuré avec un analyseur de spectre. Les résultats enregistrés sont affichés dans la Fig. 22. Pour le cas de la Fig. 22(a) un laser externe de 0,5 mW est utilisé à l'entrée. La ligne pointillée rouge indique le niveau mesuré par l'analyseur en absence de la cavité résonante. La cavité résonnante de la Fig. 21 est alors interposée entre le laser

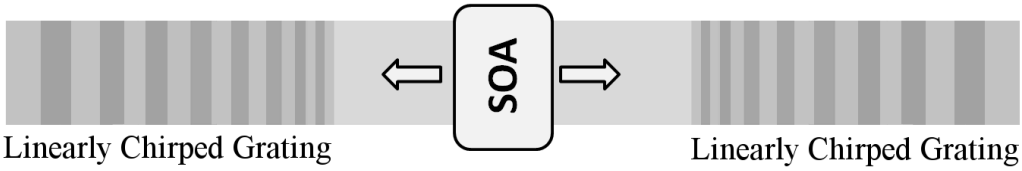

Fig. 21 Le modèle d'un amplificateur résonant utilisé dans les mesures expérimentales. Le miroir métallique qui bordé auparavant d'un côté la cavité a été remplacé par un second LCG.

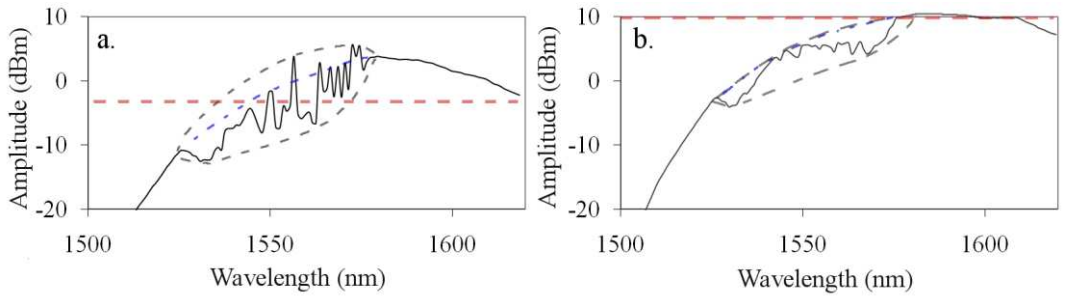

Fig. 22 Des graphiques représentant l'amplitude du laser externe en fonction de la longueur d'onde, après son passage à travers l'amplificateur résonant de la Fig. 21. Deux niveaux différents (marqués en rouge pointillé) du laser externe ont été utilisés à l'entrée d'amplificateur: a. 0,5 mW; b.10mW.

externe accordable et l'analyseur. Le niveau du signal détecté dans ce nouveau cas par l'analyseur est marqué avec une ligne noire continue.

Lorsque le laser accordable émet hors de la bande passante des réseaux de Bragg, le rayonnement externe va passer à travers le SOA une seule fois. Mais la région intéressante est représentée par la bande de réflexion des réseaux de Bragg, comprise entre 1530nm et 1570nm, dans laquelle le laser externe passe à travers le SOA plusieurs fois avant de sortir de la cavité. Dans cet intervalle, l'amplitude mesurée par l'analyseur semble varier considérablement dans le temps. Cette variation dans le temps est enregistrée par l'analyseur comme une variation avec la longueur d'onde λ, puisque l'amplitude correspondante à chaque longueur d'onde est enregistrée pendant quelques secondes, avant que le laser externe émette sur une prochaine longueur d'onde. En effet, lorsque le laser externe est laissé à émettre sur une longueur d'onde choisie un temps suffisamment long, l'amplitude du signal enregistrée par l'analyseur va osciller de façon aléatoire entre les deux enveloppes tracées en traits noirs pointillés dans la Fig. 22. Entre les deux enveloppes, la ligne pointillée bleue de milieu montre l'amplitude du signal quand les réseaux de Bragg ne sont pas présents et donc le signal ne passe qu'une seule fois à travers le SOA.

La cause de l'instabilité temporelle observée dans la bande de réflexion n'est pas bien comprise, mais elle peut être liée à la compétition des modes de la cavité laser. Comme le signal n'est pas assez fort pour attraper toute l'énergie des paires électron-trou de la cavité, il va y avoir des moments quand une partie de cette énergie servira à amplifier l'émission spontanée du SOA qui sera reflétée dans la cavité par les réseaux de Bragg.

À l'opposé, lorsqu'on augmente la puissance du laser externe à 10 mW comme dans la Fig. 22(b) le niveau mesuré à la sortie de la cavité n'augmente pas avec la même quantité par rapport au cas de la Fig. 22(a). C'est parce qu'on atteint la saturation du gain offert par le SOA. Dans cette situation, il n'y aura aucun avantage à utiliser une telle cavité résonante pour l'amplification d'un signal externe, comme l'amplitude à la sortie sera inférieure à l'amplitude de l'entrée (la ligne noire est sous la ligne rouge pour presque toutes les longueurs d'onde).

Pour conclure cette section, une cavité résonnante construite avec des LCG peut considérablement amplifier un signal externe et agir comme un amplificateur uniquement pour de faibles niveaux de puissance injectée, sous le niveau nécessaire à la saturation du SOA. Dans la région du spectre correspondante à la bande de réflexion des réseaux de Bragg, le niveau d'amplification peut devenir 5dB supérieur au niveau enregistré par le SOA seul. D'autre part, l'émission spontanée réfléchie dans la cavité par les réseaux de Bragg sera une source d'instabilité pour cet amplificateur résonant. La seule façon de contrer cet effet indésirable est d'augmenter le niveau de la radiation à l'entrée jusqu'à ce que tous les porteurs électriques à l'intérieur de la cavité soient saturés. Malheureusement, cela forcera aussi une réduction des performances de cet amplificateur résonant jusqu'au point que ça rendrait son utilisation inutile.

6. Conclusions

La partie théorique de cette thèse a été axée sur la recherche de nouvelles alternatives simples aux sources de type supercontinuum dans les applications WDM. Le manuscrit détaille les idées novatrices du projet «Continuum» qui visait à créer une cavité résonante capable de produire un spectre continu dans toute la bande C. Dans

cette cavité allait l'un des réflecteurs métalliques est remplacé par un réseau à pas linéairement variable (LCG) ayant le rôle d'annuler ou d'élargir les modes résonant de la cavité.

Le chapitre 3 du manuscrit cherche d'abord la condition nécessaire et suffisante pour qu'un LCG soit capable d'agrandir les modes d'une cavité résonante. Ensuite, il présente une série de simulations sur tous les LCG technologiquement réalisables, cherchant un réseau avec les caractéristiques requises. Trois paramètres ont été testés dans ce but, sans un succès réel. On a trouvé que le temps de retard de groupe (*GTD*) d'un LCG est proportionnel avec le chirp et la longueur du réseau et inversement proportionnel à son coefficient de couplage. On a constaté que le *GTD* est toujours positif dans la bande de réflexion du LCG. Dans la littérature, ce manuscrit est la première étude de la variation du *GTD* avec les paramètres d'un LCG.

Dans le chapitre 4 l'idée d'élargissement des modes est testée sur les réseaux ayant des couches aléatoires. Comme une recherche exhaustive de tous les réseaux aléatoires aurait été impossible, une idée originale était d'adapter une méthode de synthèse génétique (spécialement conçue pour des réseaux à variation continue d'indice) en but de synthétiser des réseaux aux couches discrètes. Nous avons décidé d'appliquer un algorithme génétique sur quelques petites populations initiales aléatoires de réseaux pour synthétiser de nouvelles structures en fonction de nos besoins. En termes de performances, les réseaux ainsi synthétisés étaient beaucoup mieux que n'importe quel autre réseau provenant de populations (même beaucoup plus nombreux) sur lesquelles l'algorithme génétique n'a pas été appliqué. Les structures sur InP se sont avérées plus performantes que les réseaux fibrés. Enfin, à la fin de la section dédiée à l'algorithme génétique, on a analysé l'influence d'un réseau génétique sur le spectre d'une cavité résonante. Un élargissement modal de l'ordre de 15 nm a été constaté avec une structure pareille. Dans le manuscrit original, les résultats après avoir utilisé une deuxième méthode de synthèse ont été aussi présentés. Par la suite, on a tiré la conclusion que le principe de causalité peut être à l'origine du fait qu'un réflecteur continuum parfait ne peut jamais être construit.

La partie expérimentale de la thèse porte sur la recherche de nouvelles applications pour les cavités résonantes construites avec les LCG. L'ajout d'un filtre accordable dans une telle cavité créera un laser accordable. Ce type d'application est le plus

adapté pour ces structures résonantes, comme les expériences antérieures de Bergonzo *et al* peuvent aussi le confirmer. Une cavité formée entre deux LCG a également été testée comme amplificateur résonant pour différents niveaux d'un laser externe. Pour les niveaux de puissance faibles d’un tel laser externe, l'amplification atteint un bon niveau mais est instable, tandis que pour les niveaux de puissance élevés, l'amplification est stable, mais insuffisante.

PART 2

Manuscript

Synthesis of chirped Bragg mirrors for spectral widening of optical cavities

Chapter 1

Introduction

1.1 Optical cavities

An optical cavity is defined as a region bounded by two or more mirrors that are aligned to provide multiple reflections of lightwaves [1]. Because of these reflections, electromagnetic radiation is made to interact with itself multiple times before exiting the cavity. For start, let us consider a uniform source of electromagnetic radiation inside the cavity. At certain frequencies - called resonance frequencies - the electromagnetic radiation will sustain itself after the reflections on the cavity mirrors, while at other frequencies it will attenuate itself correspondingly. Considering all frequencies of the electromagnetic spectrum, the law of conservation of energy is always satisfied, as each region of positive interference (for which the radiation amplitude increases) is surrounded by regions of negative interference (for which the radiation amplitude decreases). If the uniform radiation enters the cavity from the outside, there will be two resulting beams, one which is reflected, and the other one transmitted by the cavity. The same figure of resonant peaks and valleys is found also in the two resulting beams' spectra, but now the law of the conservation of energy ensures that the peaks in the transmission spectrum correspond to the valleys in the reflection one and vice-versa.

A simple schematic of an optical cavity is shown in Fig. 1, where M_1, M_2 are the metallic mirrors between which the cavity is formed. This cavity can function in a passive mode (as represented in Fig. 1.1) in which case it is called a Fabry-Perot filter. The radiation which enters the cavity from the left will be divided by the cavity

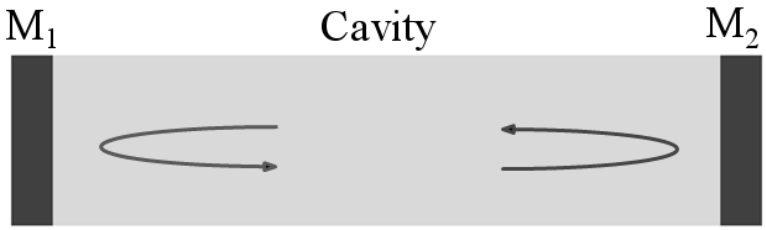

Fig. 1.1 Simple schematic of a passive optical cavity formed between two metallic mirrors (M_1, M_2). The light propagates between the mirrors through the core of an optical fiber. This type of structure is also called a Fabry-Perot cavity.

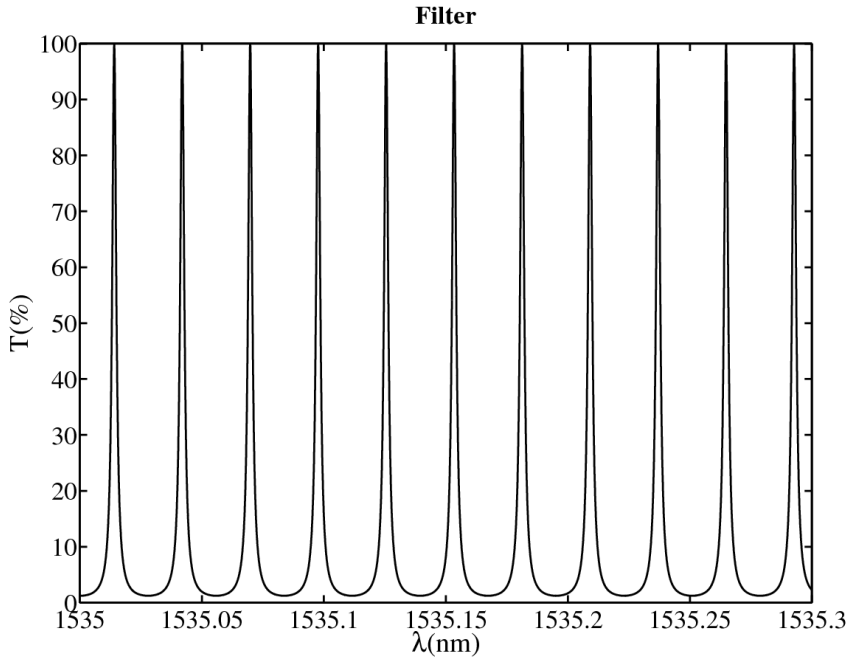

Fig. 1.2 Transmission as a function of wavelength when the Fabry-Perot cavity is functioning as a filter with the reflectivities of the mirrors R_1=R_2=0.8. The distance between the mirrors is L=3cm.

in two parts: one part of the light is reflected (propagating back to the left) and one part is transmitted (propagating outside of the cavity to the right). If we consider that the incident radiation has a uniform spectrum for all wavelengths, the transmitted radiation will have a spectrum similar to that of Fig. 1.2. The spacing (called Free Spectral Range – FSR) between the resonant peaks (modes) depends on the length of the cavity and the refractive index of the medium inside. The difference between the maxima and minima of transmission depends of the reflectivities of both mirrors.

The same cavity of Fig. 1 could be used as an amplifier or a laser if an active medium is inserted between the mirrors. Generally speaking, an active medium is a type of material that emits coherent radiation or exhibits gain as a result of electronic or molecular transition from a higher (previously excited) state to a lower state. The excitation to higher energy states is realized by pumping the material with energy

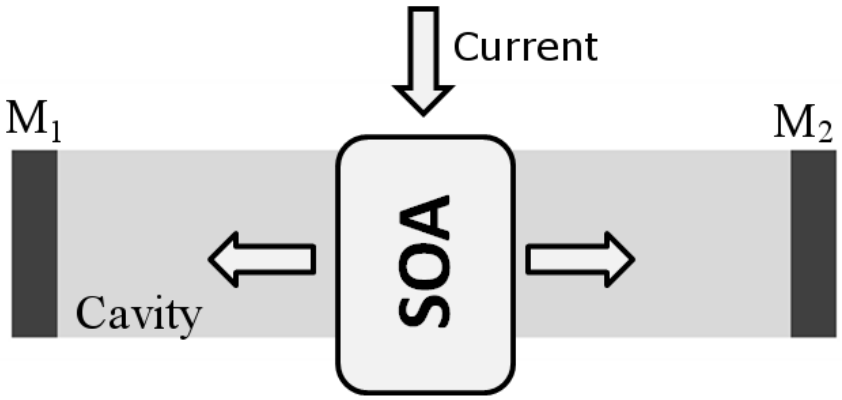

Fig. 1.3 Simple schematic of an active optical cavity formed between two metallic mirrors (M_1, M_2). The active medium is a Semiconductor Optical Amplifier (SOA), which transforms the injected electrical energy into optical gain.

from the exterior. Because throughout this thesis the active medium consists of a Semiconductor Optical Amplifier (SOA) the energy used for pumping was electrical in nature (represented as a current input in Fig. 1.3).

When an external signal is injected into the structure of Fig. 1.3, the cavity is said to function as an amplifier. The most important quantity describing this functioning mode is the gain, defined as the ratio between the output and the input amplitudes of the signal, as a function of wavelength. The gain of such an amplifier will follow the spectrum shape of the passive cavity shown in Fig. 1.2, with maxima separated by the same Free Spectral Range (FSR). However, compared to the passive case, this time the maxima values are greater than 1. The maximum amplitude of the cavity gain depends on the reflectivities of both mirrors and the gain of the SOA alone (gain of the SOA placed outside the cavity). It can usually be greater than 100 (20dB).
The structure of Fig. 1.3 can also generate its own radiation by spontaneous emission in the active medium. Starting with a certain threshold of the SOA current, this functioning regimen becomes that of a Fabry-Perot laser. The laser thus created can emit on multiple wavelengths, in which case it is called a multi-mode laser, or on a single wavelength, in which case it is called a single-mode laser. In both cases, the laser emission wavelengths correspond to one or more of the resonant transmission peaks of the passive cavity (Fig. 1.2).

We can conclude from this section that the transmission function of the passive cavity influences both the gain of the amplifier and the emission spectrum of the laser created by adding an active medium in such a cavity. That is why this thesis

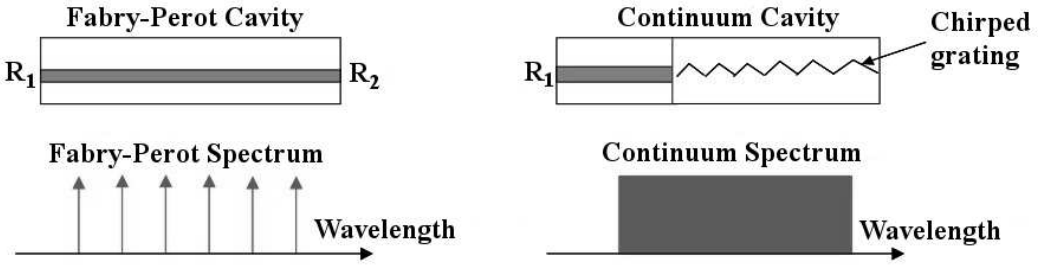

Fig. 1.4 Comparison between a Fabry-Perot cavity (with its resonant modes) and a Continuum cavity (with its resonant enlarged mode)

started with the idea that by acting on the geometry of the passive cavity alone and shaping its resonant modes, we will also succeed in shaping the emission spectrum of the corresponding laser.

1.2 Thesis history

The idea that it would be possible to shape the transmission of a filter, or the gain of an amplifier, or the spectrum of a laser, by acting on the geometry of their corresponding resonant cavities materialized in the so-called Continuum project. This was a 36-months ANR (*Agence Nationale de la Recherche*) project [2] which started in 2009, while I was an internship student at SUPELEC. The biggest aim of the project was the construction of a continuum spectrum laser which was supposed to have a bandwidth larger than 75nm. A comparison between such laser cavity and the cavity of a classical Fabry-Perot laser is shown in Fig. 1.4. At the left of this figure, we can recognize the same cavity presented in Fig. 1.1. Its ideal spectrum is schematically presented below it. To the right there is the Continuum cavity and its ideal resonant spectrum. Studying the figure, it can be seen that the project's core idea is to act on the cavity's geometry by replacing the metallic mirror by a chirped Bragg grating. As it was already said in Section 1.1, it is possible to shape the emission spectrum of a laser by acting on the cavity's geometry, thus changing its resonant modes. By carefully choosing the right grating for a certain cavity, it was thought the resonant modes in the cavity could even be canceled. The spectrum would become single-mode with an enlarged bandwidth equal to the reflection bandwidth of the Bragg grating used. This type of laser would have been a cheaper alternative to the present Supercontinuum lasers for short range data communications. Other requirements of the project are listed in Table 1. The project was a conjoint effort between SUPELEC (SUP), Alcatel Thales III-V Lab (ATL), Institut Carnot de

Bourgogne (ICB) and Institut d'Electronique de Sud (IES). SUPELEC was responsible with the coordination of the project and also with everything linked to the design of the cavity and testing of the final products. Alcatel was in charge with the technology and fabrication of the integrated continuum cavities, whereas ICB and IES were responsible with dynamic modeling of the active cavities, taking into account thermal and non-linear phenomena.

A LCG, used very often in future chapters of the thesis, is similar to a uniform Bragg grating, except for the fact that its grating period varies linearly from one end to the other of the grating. As it will be later shown, none of the final objectives of the Continuum project was met because of some limitations imposed by fundamental physical laws. Nevertheless, trying to approach some of the initial requirements made us develop some interesting structures which we will describe later in this manuscript. After abandoning the initial path developed by my colleague Xunqi WU requiring the use of LCGs, we adopted instead the more complicated path of designing our own chirped Bragg gratings by numerical methods.

TABLE I
SUCCESS CRITERIA FOR THE CONTINUUM PROJECT

Regimen	***Parameter***	***Success Criteria***
Filter	*Power*	*P > 10mW*
	Bandwidth	*BW > 75nm*
Amplifier	*Gain*	*G > 20dB*
	Noise factor	*Nf < 5dB*
	Bandwidth	*BW > 50nm*
Laser	*Power*	*P > 10mW*
	Bandwidth	*BW > 75nm*

1.3 Outline

The understanding of a large part of this manuscript will generally be available to anyone who has a general background in physics and mathematics. There will be only small sections where a more thorough knowledge of the field will be necessary.

After this chapter's small introduction into the subject of optical cavities and the working environment which permitted the finalization of this manuscript, we will pass to a presentation of the state of the art of the devices capable of emitting coherent light on a large bandwidth. These devices, the so-called Supercontinuum sources, or white-light lasers, will be described in the first part of Chapter 2. Their functioning will be explained, how they were discovered, their main applications, alternatives and limitations. A special emphasis will be placed on the telecom applications. The second part of the chapter will go deeper into the idea behind the Continuum project, how it originated and its basic mathematical grounds.

Chapter 3 concentrates on the use of Linearly Chirped Gratings (LCGs) for the Continuum generation. After thoroughly explaining the structure and parameters of a LCG, we will present the results obtained after using all the technologically available LCGs to form resonant cavities. This chapter will also contain a more thorough analysis of the mathematics behind the Continuum generation and a small presentation of the two types of optical cavities studied in this thesis. This is needed to fast check if a chirped grating could be employed as a mirror to enlarge the modes of a Fabry-Perot cavity. Because of the negative results obtained with the LCGs, the necessity to design a special Bragg grating to reach our aim will be obvious at the end of this chapter.

And this is exactly what we will do in Chapter 4, which will contain most of the innovative part of the present manuscript. Two methods for grating synthesis will firstly be explained, followed by some grating designs obtained after implementing those methods. Spectral examples will be given for both of the two types of gratings mentioned in Chapter 2 (fiber and integrated).

Chapter 5 deals with the experimental part of the thesis. It explains the technology behind each type of cavity studied and it tries to find new applications for each. The

cavities studied are formed with LCGs, as this type of grating was considered sufficient in the initial phases of the Continuum project. In spite of their inadequacy for Continuum generation, it will be seen that we can still take advantage of the LCGs' properties in other types of novel applications.

Finally, Chapter 6 will summarize the ideas presented in this manuscript and will trace some perspective-lines regarding the future work in this field.

Chapter 2

Continuum spectra

This chapter describes two radically different ways for obtaining coherent continuum spectra. The first method, very richly studied in the scientific literature for the past thirty years, is depicted in Section 2.1. It is a well demonstrated method which found numerous applications in different domains. The other method, described in Section 2.2, consists of an original idea sketched for the first time in the Continuum project.

2.1 Supercontinuum

Till present, the most documented way to generate large-band intense light radiation is by what is known in the scientific literature as a "supercontinuum". As defined by its discoverer, R.R. Alfano [3,4], "supercontinuum generation is the phenomenon of production of intense ultrafast broadband white light pulses arising after the propagation of intense picosecond or shorter laser pulses through condensed or gaseous media". As seen from the initial definition, a supercontinuum source has three main characteristics: a) high intensity; b) large spectrum; c) fast pulsed. All three characteristics result from the way in which a supercontinuum (SC) is produced. It firstly needs a very powerful laser, which will act as a seed (source, pump) laser. In the beginnings of SC generation, the level of power needed was offered only by ultrafast laser pulses. Those ultrafast laser pulses were collimated and injected into a strong non-linear medium. After a certain propagation distance the SC appeared. Now going back to the three characteristics of a SC, every one of them arises from the premises of the SC's generation. The first one, high intensity, is due to the fact that a supercontinuum still propagates as a laser. The non-linear phenomena responsible with the SC generation do not modify the beam geometrical properties of the initial seed laser, resulting in high energy densities for the SC laser as well. The second characteristic (a large spectrum) is what differentiates a SC from a laser. That is why a SC source is also called a "white-light laser", as its spectrum can be as large as the spectra of incandescent sources, usually hundreds of times larger than that of the initial seed laser used. As for the third characteristic cited by Alfano, it is no more necessary for the SC sources of our day. Even though the initial definition implied that a supercontinuum could function only in the ultrafast pulsed regime, as that was the only way to generate a high intensity seed laser, with the advent of optical fiber SC generation, it was later seen that such a laser can be generated also in the continuous-wave (CW) regime, by using cascaded Raman fiber lasers [5].

2.1.1 Physics

As stated in the introductory part of section 2.1, a SC is generated after the propagation of a source laser through a non-linear medium. The generation of a SC from an optical fiber for the first time in 1976 [6] was the great step forward which

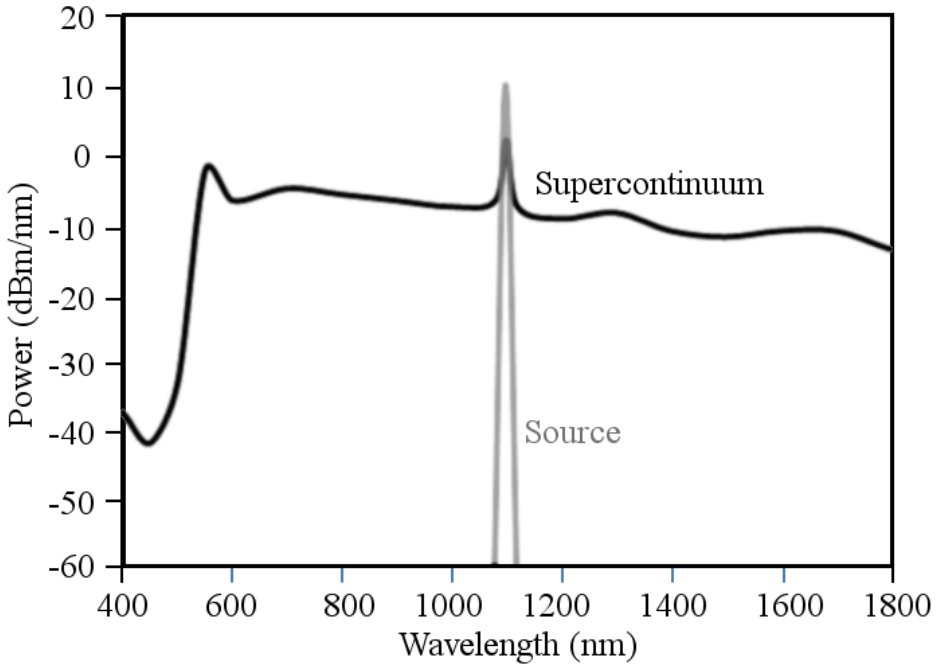

Fig. 2.1 Comparison between a typical Supercontinuum spectrum [22] and the spectrum of the seed (source) laser used for its generation

permitted the introduction of SC into the telecommunication industry. This discovery not only opened the path to a continuous-wave supercontinuum, but it also opened the path to the generation of very large octave-spanning SC radiation. Initially only strong non-linear mediums were used, but it was seen that optical fibers can also exhibit impressive non-linear effects because of their long interaction distances with the light. In Fig. 2.1 a comparison is shown between the typical spectrum of a supercontinuum (SC) and that of its pump source. The SC was generated by passing the 1064nm pulsed pump laser through a photonic crystal. A more than an octave frequency span is noticed.

The physics behind the SC generation is not simple. In fact, under the name of "supercontinuum" we understand today a large body of non-linear phenomena which interact together in complicated ways and which still continue being researched in the present day - a few decades after the SC discovery. The four main non-linear phenomena involved in the first experiments of SC generation are the self-, induced-, and cross-phase modulations and the 4-photon parametric generation.

Later, the generation of SC in photonic crystal fibers (PCF) brought forward other interesting phenomena linked to the creation of soliton-like pulses. Thus, in this type of media, it became possible to distinguish two different regimes of SC generation

[7]: a) an incoherent one, corresponding to the highly non-linear state obtained in the PCF after the injection of long and intense pump pulses; and b) a coherent regime, corresponding to the apparition of coherent soliton-like radiation in a PCF after it was pumped with long pulses in the anomalous dispersion regime. This second regime, which is specific to the optical fiber media, has been extensively researched during the last decade, as it could find useful applications in the telecom industry [8].

As this is only a small snapshot into the world of supercontinuum and the physical phenomena linked to its creation, it is no need to go into mathematical detail regarding the non-linear phenomena that stand at its core. For the interested, the most complete source of information on this subject remains the supercontinuum monograph of Alfano [3].

2.1.2 History

The discovery of the supercontinuum was announced in three papers [4, 9, 10] dating from 1970, signed by R.R. Alfano, who is thus credited with the discovery. One of the experimental setups used from the beginnings for the SC generation [3] is schematized in Fig. 2.2. The most expensive part of this setup is the laser pump, which has to be an ultrafast picosecond or femtosecond pulse laser. This is usually obtainable only through mode-locking. In the first experiments, the pump laser was a mode-locked Nd:glass laser emitting at 1.06μm with a peak power of $5x10^9$ W. What follows next in the schematic is a KDP crystal used for the generation of the second harmonic. The non-linear phenomena responsible with the SC generation in the target crystal were best activated for a frequency corresponding to the second harmonic of the pump laser. This radiation had a wavelength of 530nm and a power of $2x10^8$W. After the second harmonic generation a filter can be used to remove the

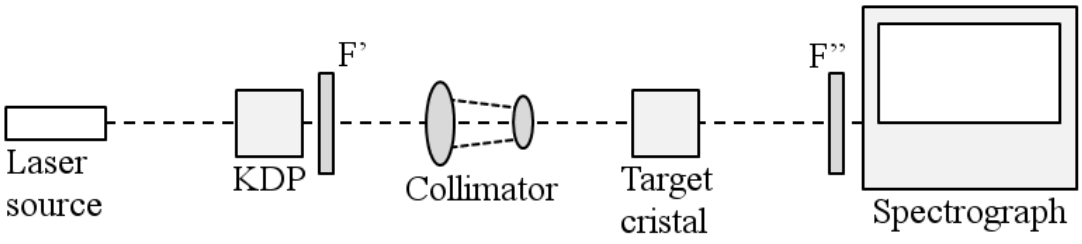

Fig. 2.2 Schematics of the first experimental arrangements used for the supercontinuum generation in the 1970s.

pump wavelength from the propagating beam. Before reaching the crystal, this beam must be reduced in size by a collimating lens and focused onto the sample at the maximum possible energy density. For the SC generation in the sample crystal, one needs at least a few μJ of energy concentrated in a pulse smaller than 100fs on a sample surface smaller than 1mm in diameter.

After passing through the target crystal responsible for the SC generation, the intensity distribution could first be filtered and magnified before being projected on a spectrum analyzer.

Supercontinuum spectra have been obtained using all kind of materials, some of them exhibiting only small non-linear coefficients. As solid-state examples of such materials we can cite the quartz, NaCl, calcite and even the semiconductor GaAs. The SC spectra generated by them have very large spectral widths and random structure [3]. For comparison, the SC spectra generated in liquids have the most intense and uniform distribution. As an example, the SC spectra generated in H_2O and D_2O start from around 350nm and can extend even beyond 800nm. But the material which found the greatest number of applications and is now used the most extensively for SC generation is the optical fiber.

2.1.3 Applications

Thanks to their unique spectra, supercontinuum sources have been used extensively in numerous applications in the past decades, a fact which has made them gather increasing attention from the scientific community. A list of research applications requiring the use of SC sources is found in the book of Alphano [3] and it includes inverse Raman scattering, time-resolved induced absorption, primary vision processes, energy transfer mechanisms in photosynthesis and the list goes on.

In this section, four of the main applications of the supercontinuum will be revised, with a greater emphasis being put on the one in the telecom field. One of the most important applications of SC is in the field of *optical coherence tomography* (OCT) [11]. OCT is a method of imagery used for scanning inside the tissues with the help of the backscattered light. The retina for example can be thus scanned for macular degeneration. The resolution of this imagery technique depends on the spectrum

width of the light source, which is why a SC source is considered the best for this type of application.

Another application of SC is in the field of *optical frequency metrology* [12]. A frequency comb is a radiation whose spectrum is represented by a series of discrete equally spaced modes. Frequency combs are used in metrology to precisely measure optical frequencies very much like a vernier measures small distances. They can also be used to enhance the precision of atomic clocks from the microwave to optical domain, making them reach time precisions of 10^{-17}. But a frequency comb, which is usually created with mode-locked lasers, is useful only if it has a frequency span larger than one octave. It is in this stage that a SC is required when pumped by a mode-locked laser, as it can generate a spectral comb larger than two octaves.

Another field of application for the supercontinuum is the *ultrafast pulse compression* [13]. When the ultrafast radiation coming from a mode-locked laser is transformed into a white light source by enlarging its frequency bandwidth, a compression into the time domain simultaneously happens, as frequency and time are conjugate variables – one is the Fourier transform of the other. This allows for the short duration pulses of the mode-locked laser to be shortened even more. It is believed that durations under 1fs will be soon achieved with this technology. This application is very useful for probing physical, chemical and biological phenomena which have a life-time in the femtosecond domain. It can also study picosecond-

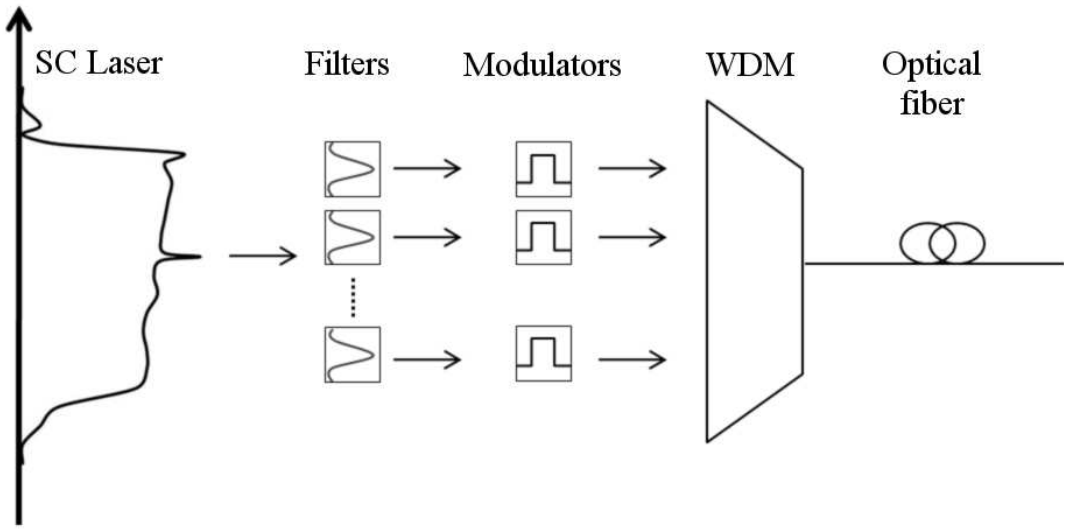

Fig. 2.3 Schematics of the way in which a supercontinuum source could be emplyed in WDM telecommunications

phenomena with better resolution than it was ever-before possible.

Finally, the application of the SC which is in direct connection with the subject of this thesis is in the *WDM telecommunications* field [14-16]. A schematic representation of the way in which a supercontinuum can be used in WDM is shown in Fig. 2.3. Instead of using a different laser source for each user, an approach of using a single continuum laser source which is later sliced in different parts by optical filters is preferred because of the greater fiability. After slicing, each individual channel is modulated in amplitude with the useful information and then sent to a WDM multiplexer before being transmitted over the optical fiber to the users.

2.1.4 Limitations

Despite their unmatched ability to generate large-bandwidth high-power radiation, SC sources also have their limitations. Their biggest draw-back is their prohibitive *cost*. Comparing the components of a typical SC arrangement (Fig. 2.2) as to their cost, it is the mode-locked ultrafast high power pump source that is by far the most expensive component of the setup. Even if with the advent of optical fiber SC the requirements for the pump source have been relaxed in terms of speed and power, there is still a demand for cheaper SC sources. This is especially true whenever the cost of the source is divided between small numbers of households, as it is in the case of small local networks, like WDM access area networks. The alternatives of SC sources for this small type of networks will be discussed in the next section.

Another draw-back of SC sources is their *size and setup complexity*. Regarding this aspect also, it is the pump source that is the most bothersome component. Historically, the mode-locked pump source most used for SC generation is a Ti:sapphire laser. Later, fiber SC lasers were excited using Er^{3+} and Yb^{3+} doped fiber laser pumps, which were cheaper but not necessarily smaller alternatives to the Ti:sapphire laser.

A last disadvantage of the SC is its *theoretical complexity*, as some of the phenomena which are at the base of SC generation are still under research today. This makes

thermodynamic simulations of the SC a real challenge, and so are the numerical methods for the design of a white-light laser source.

2.1.5 Alternatives

Because of their high price when used in small-scale applications, as it is in the already mentioned case of local area networks, some cheaper alternatives to SC sources have been searched. To show the difficulty of choosing for such an alternative to supercontinuum, a comparison is made in Fig. 2.4 between the spectra of different light sources. For each source, only the useful power (the fraction of the emitted radiation which could be directed into an optical fiber) was considered. Firstly, there is the classical *Xenon arc lamp*, which mimics very well the natural spectrum of the sun and is used in different kind of projection devices. Even if it was considered not long ago a bright source of radiation, its beam divergence makes its useful power to be nowhere near the power distribution of a SC source. On the contrarily, the strictly directed light emitted by a He-Ne laser has a very high useful power, but a very narrow bandwidth.

The only two sources that can effectively replace a SC source for small scale applications are the Superluminescent diode (SLED) and the Amplified Spontaneous Emission (ASE) source. Both of them are functioning on the same principle of under-threshold spontaneous light generation and amplification. Whereas SLEDs are semiconductor-based diodes with a similar structure to that of a Fabry-Perot laser, functioning under threshold because of their insufficient feed-back, the spontaneous emission in ASE sources is realized on doped fiber.

During recent years incoherent light sources like SLEDs and ASE sources did have some success in replacing SC in small WDM area networks because of their low price [17, 18]. Firstly, their bandwidth is large enough for covering the whole band C (1530-1565nm). Secondly, their power could be amplified into the fiber to satisfactory values by using different types of doping elements. But these sources have also their drawback which stems from their level of incoherence. Their optical noise figure translates itself into a higher bit-error rate (BER) than that of a SC.

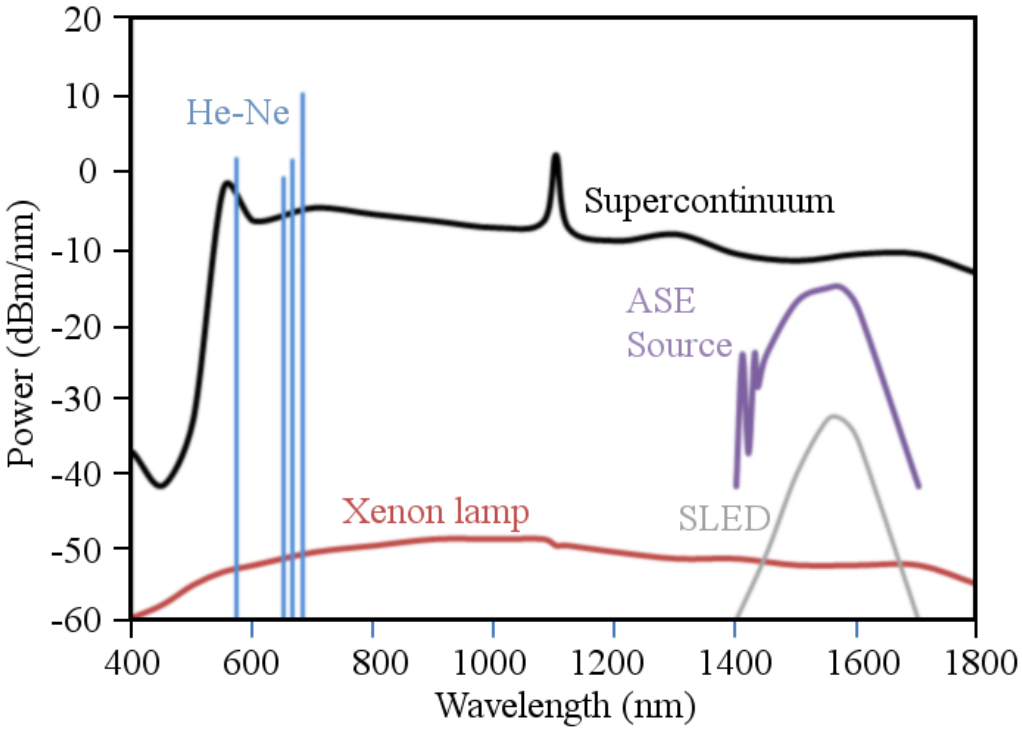

Fig. 2.4 Comparison between the spectra of different types of light sources: He-Ne (Helium-Neon laser); Xenon lamp; ASE (Amplified Spontaneous Emission) Source; SLED (Superluminescent diode); Supercontinuum. For each source, only the effective power was considered (the level of generated power which can be coupled onto an optical fiber)

In the search for cheaper alternatives of the SC, it can be resumed that an ideal continuum source designed only for small area WDM networks should generate powerful coherent radiation with just enough continuous bandwidth to cover at least an entire telecommunication band. Next section of this chapter is a description of the Continuum project innovative ideas which also motivated this thesis and which had as the main goal finding precisely this type of ideal WDM continuum source.

2.2 Continuum cavity

As already described in the *Introduction*, the beginnings of the research which motivated this thesis are to be found in the ideas of the Continuum project, a project which had as its main goal the development of a cheap alternative to SC for small scale WDM telecommunications. Other objectives of the project were summarized in Table 1 of the Introduction. All of the three types of devices targeted by this project had the same core idea: the design of a passive resonant cavity in which the resonant modes are enlarged or even canceled completely. This type of resonant structure will

be further on called a *Continuum cavity*. In analogy with a Fabry-Perot laser which oscillates on one of the resonant frequencies of its cavity, a continuum laser would oscillate on a large continuous bandwidth, as it will not be able to foster any frequency more than another. It is true that beside the design of a Continuum cavity, a judicious choice of an active medium is also needed to make a laser emit on a continuous interval. This is because the shape of the active medium's gain plays an equally important role in the final laser emission as the role of the geometry of the cavity. Nevertheless, the right choice of the active medium is beyond the scope of this thesis. All simulations involving active cavities presented in this manuscript will take into account non-material-specific general phenomena and an active gain which is uniform on the entire desired spectral interval.

As explained in Chapter 1, one must act on the geometry of a passive cavity in order to change its resonant spectrum. An efficient way to do that is if one acts on the geometry of the Bragg mirrors which border the cavity. The next section will thus start by describing the physical principles behind mode-cancelling of a resonant Fabry-Perot cavity using linearly chirped gratings (LCGs). This is followed by the presentation of the origins of the Continuum idea and by a section dedicated to the mathematical representation of that idea. These general notions are needed before passing to the specific structures and numerical simulations of Chapter 3.

2.2.1 Physics

The characteristic transmission spectrum of a Fabry-Perot (FP) resonant cavity was shown in the Fig. 1.2 of the *Introduction*. It was explained that certain wavelengths will positively interfere with their reflections from the cavity mirrors and thus will reinforce their exiting amplitudes and form transmission peaks, whereas others will negatively interfere with their reflections, forming the valleys in the spectrum of Fig. 1.2. A Continuum resonant cavity would have such geometry that all radiation no matter the wavelength, would positively interfere with itself inside the cavity. The transmission characteristic of such a cavity will have a maximum value for all the wavelengths. Correspondingly, because of the conservation of energy, the reflection spectrum will also be uniform for all wavelengths and its amplitude will have a value equal to the difference between the incident and transmitted waves. When the two

reflectors forming the cavity will have the same value of the reflectivity [19, 55, 56] the transmitted wave will have the same amplitude for all the wavelengths as the incident wave, while the reflected wave will be null.

Aiming to generate such a continuum resonance condition, the initial idea of the Continuum project was the design of a cavity formed between a metallic mirror and a linearly chirped grating (Fig. 2.5). A linearly chirped grating (LCG) is a reflector characterized by a refractive index alternation between two values, with a period that varies linearly from one end to the other of the grating. In Fig. 2.5 the low refractive index has a lighter color than the high refractive index. It can be observed that as one is approaching the right side of the LCG, the length of each pair of layers increases linearly. Thus, each LCG could be considered a series of consecutive Bragg gratings characterized by linearly increasing periods. Because of this similarity with Bragg (uniform) gratings, a linearly chirped grating could also be called a *linearly chirped Bragg grating* (LCBG).

At the left side of the cavity in Fig. 2.5 all radiation wavelengths are reflected in the same location, at the site of the metallic mirror. On the contrary, at the right side of the cavity each wavelength is reflected at a different location on the grating. Smaller wavelengths are reflected at the beginning of the grating, corresponding to where the small grating periods are located, whereas longer wavelengths are traveling a greater distance inside the grating before being reflected. This is due to the fact that each pair of layers (one layer having a low, the other having a high refractive index) has a corresponding wavelength which it reflects more than it reflects every other wavelength, in virtue of its similitude with a Bragg grating.

A mode number is the number of times a resonant wavelength is comprised in a round-trip of the radiation inside the cavity. Because longer wavelengths are

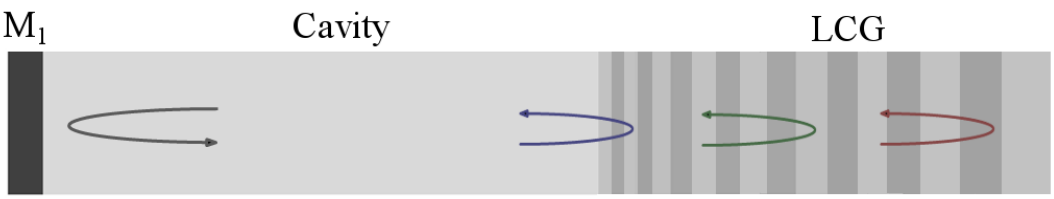

Fig. 2.5 Representation of optical paths inside a Continuum cavity: different wavelengths will travel different optical paths, in function of the position in the LCG where their reflection takes place. Smaller wavelengths are represented in blue, whereas intermediate wavelengths are in green and small wavelengths are drawn in red.

reflected farther away and are thus having longer round-trips, it can be supposed that if one matches the right LCG to a certain cavity length, one will be able to maintain the same mode number for all the reflected wavelengths. This is equal to having a continuum resonance condition satisfied for all the wavelengths reflected by the grating.

The physical base of the Continuum idea will be translated in mathematical form in Section 2.2.3. Until then, the next section presents how this concept was firstly applied in the design of a continuous tunable laser.

2.2.2 Origin of the idea

The idea of the Continuum project has its origins in the work of Bergonzo *et al.* on a type of continuous tunable laser formed inside a resonant cavity [20, 21]. Figure 2.6 shows a sketched representation of this type of laser, realized in a hybrid configuration (a different kind of support than the semiconductor chip used by the initial authors). Nevertheless, the principle remains the same. Firstly, a resonant cavity is formed in a fiber between a metallic mirror (M_1) and a LCG reflecting only the spectral interval comprised between 1530 and 1570nm. An active medium consisting of a SOA introduced into the cavity is modulated by a radio-frequency

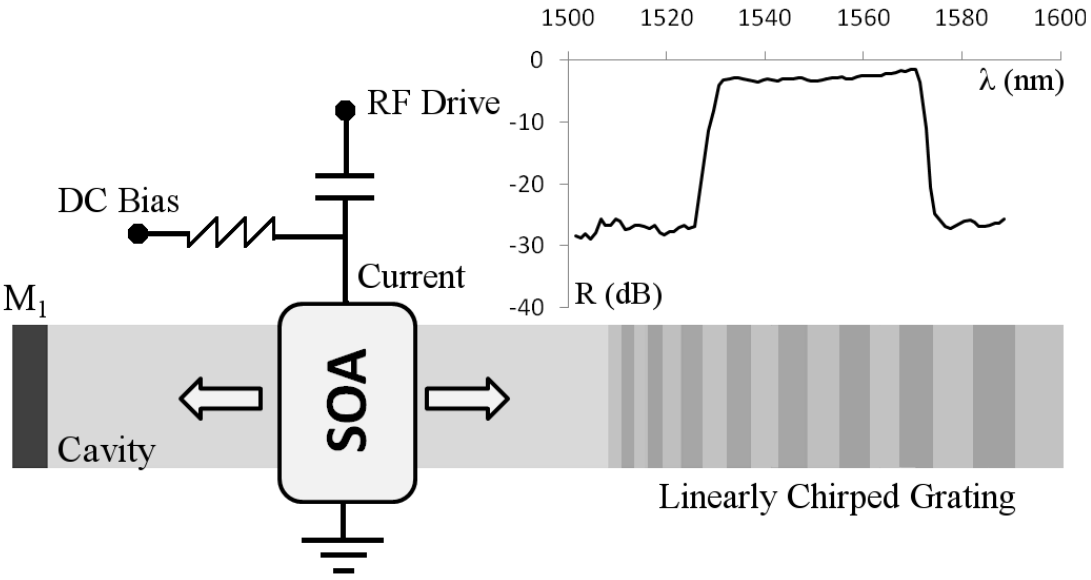

Fig. 2.6 Representation of a type of continuous tunable laser formed with a LCG, inspired by the setup used by Bergonzo *et al.* The reflectivity characteristic of the LCG is presented in the insert above the grating.

(RF) signal. It was observed that by changing the RF applied on the SOA, the cavity also changed its lasing mode. It was also noticed that the lasing emission seemed to be shifting in a continuous manner as a function of the applied RF. It was not just jumping from a resonant mode to the next one, in which case the measurements would have recorded a distance between the lasing modes equal to the free spectral range (FSR) of the cavity. The FSR, or the distance between a cavity's resonant modes, is inversely proportional to the length of that cavity. Because the cavity used by the authors was a small Fabry-Perot laser chip, the FSR would have been large enough to be detected. Thus, due to this continuous transition, the authors supposed that the resonant condition was respected by every wavelength in the reflection bandwidth (1530-1570nm) and that a continuum laser could be similarly created.

2.2.3 Mathematical approximation

The physics behind the Continuum project, explained in Section 2.2.1, could also be translated into the form of mathematical equations. Ideally, the resonant condition should be true for all the wavelengths reflected by the grating. In Fig. 2.7, each Bragg period of the chirped grating, composed of two consecutive layers of different refractive indices, is represented in blue, while the supposed optical paths of different wavelengths are represented with black double arrows.

For the writing of the subsequent equations in this section, it was supposed that each wavelength is reflected only by its corresponding Bragg period. Let us call this supposition the *reflection approximation*. That is not entirely true, as each wavelength is reflected a little bit everywhere in the grating, but it can be considered that its maximum reflection is realized at the location of its corresponding Bragg period. Considering this first order approximation, then the wavelength λ_0 corresponding to the first Bragg period Λ_0 is reflected at the immediate beginning of the grating. Its resonance condition is then written in equation (2.1) in which L_0 and n_0 are the length and the refractive index of the cavity, and m is the mode number:

$$n_0 L_0 = m\frac{\lambda_0}{2} \tag{2.1}$$

As explained in the Section 2.2.1, the continuous resonance condition over a spectral interval is equivalent with all the wavelengths in that interval having the same mode

number. For this to happen, it was shown that the longer wavelengths must be reflected further away in the grating than the shorter ones. The resonance condition for a wavelength λ_k which is reflected in the grating at the position $z(\lambda_k)$ - corresponding to the position of the Bragg period Λ_k - is written in equation (2.2). Following next in (2.3) is the resonance condition for the wavelength $\lambda_{k+1} = \lambda_k + \Delta\lambda$.

$$n_0 L_0 + n_{eff}\, z(\lambda_k) = m \frac{\lambda_k}{2} \tag{2.2}$$

$$n_0 L_0 + n_{eff}\, z(\lambda_k + \Delta\lambda) = m \frac{\lambda_k + \Delta\lambda}{2} \tag{2.3}$$

The n_{eff} parameter represents the effective refractive index of the grating, and it is usually calculated as an average between the two alternating refractive indices. The position $z(\lambda_{k+1})$ where the wavelength λ_{k+1} is reflected in the grating could be written as:

$$z(\lambda_k + \Delta\lambda) = z(\lambda_k) + \frac{\partial z}{\partial \lambda} \Delta\lambda \tag{2.4}$$

By subtracting (2.2) from (2.3), then replacing in that difference m from (2.1) and $z(\lambda_{k+1})$ from (2.4), the continuum condition becomes:

$$n_{eff} \frac{\partial z}{\partial \lambda} \Delta\lambda = \frac{2 n_0 L_0}{\lambda_0} \frac{\Delta\lambda}{2} \tag{2.5}$$

Because there is a correspondence between each wavelength and the Bragg period where that wavelength is primarily reflected, the equation (2.5) could be used to mathematically express the physical structure of the grating. This can be done by

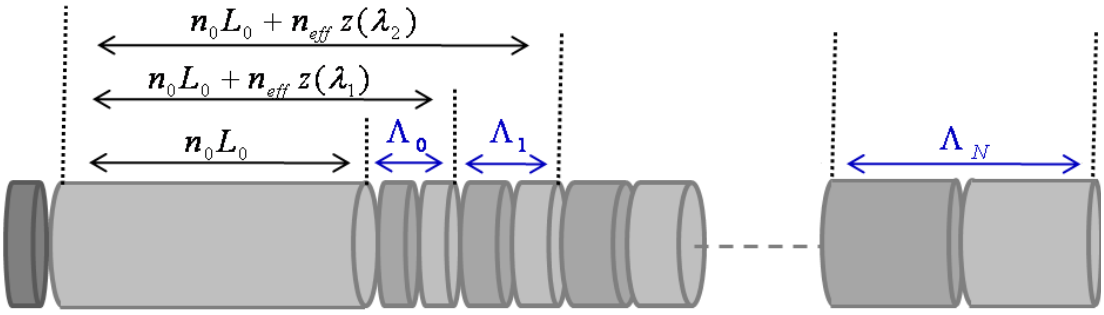

Fig. 2.7 Representation of a Continuum cavity on fiber; the grating at the right side of the cavity is divided in its constituent layers. Each pair of different layers forms a Bragg period of the grating. The length of each period – represented in blue - is linearly increasing from left to right. The supposed optical paths of different wavelengths through the cavity are represented with black double arrows.

replacing λ with Λ accordingly to the Bragg wavelength law:

$$\lambda = 2n_{eff}\Lambda \tag{2.6}$$

The physical structure of the LCG could now be defined using the physical chirp parameter C_Λ, defined in (2.7) and which is equal to how fast the period of the grating changes along its longitudinal axis. For the case of LCGs the chirp is a constant value.

$$C_\Lambda = \frac{\partial\Lambda}{\partial z} = \frac{\partial\Lambda}{\partial\lambda}\frac{\partial\lambda}{\partial z} \tag{2.7}$$

After inserting (2.5) and (2.6) in (2.7) it is found that the chirp of a LCG satisfying the Continuum condition is equal to:

$$C_\Lambda = \frac{\lambda_0}{2n_0 L_0} \tag{2.8}$$

Because L_0 is the length of the cavity, equation (2.8) states that the chirp of a LCG is inversely proportional to the length of the cavity for which it is used to generate a continuum.

Beside the physical chirp, which describes the structure of the grating, another physical quantity could be defined to describe the spectral characteristic of the grating. Taking into account the close correspondence between a wavelength and its corresponding Bragg period (2.6), the continuum condition (2.8) is defined for the case of the spectral chirp as in equation (2.9). This quantity describes how fast the reflection spectrum broadens with the longitudinal size of the grating.

$$C_\lambda = \frac{\lambda_0}{L_0} \tag{2.9}$$

The generalities presented in this Chapter will be useful in the next one, in which the idea of the Continuum project was tested using numerical tools. A complete development of the initial idea of the Continuum project can be found in the thesis of Wu [19]. Following in the next three chapters the original work of this manuscript will be concentrated.

Chapter 3

Linearly Chirped Gratings

This chapter presents the entire development of the initial Continuum idea which was theoretically outlined in the previous chapters. It begins by shortly describing the parameters which can be technologically varied when using a LCG to design a continuum cavity. It introduces also the two types of cavities used in both simulations and experiments. A more precise form of the mathematical continuum condition presented in the previous chapter is needed before passing at its numerical verification for the case of technologically realizable LCGs. The original results of such numerical simulations are presented toward the end of the chapter.

3.1 Description

Linearly chirped gratings were already mentioned in the first two chapters of the thesis in conjunction with their utility to the Continuum project. In the previous chapter, it was said that a LCG can be regarded as a series of very small uniform Bragg reflectors having periods which are linearly varying along the axis of the grating. Mathematically, this can be written as:

$$\Lambda_k = \Lambda_0 + C_\Lambda \cdot z_k \tag{3.1}$$

In equation (3.1) Λ_k is the period of the k-th Bragg reflector in the grating, C is the chirp of the grating and z_k is the start position of the k-th Bragg reflector along the grating axis. For a LCG the chirp C is a constant quantity and it determines how rapid the Bragg period varies along the grating axis. Each small Bragg reflector can have multiple periods, but every linearly chirped grating described in this manuscript will be composed from Bragg reflectors of only one period. This means that each pair of layers of different refractive indices forms a Bragg period, while the next pair of layers forms the next Bragg period of the grating and so on. Thus a LCG, which is formed of the entire succession of all the Bragg periods, can be represented as a refractive index variation as the one depicted in Fig. 3.1 for the case of a fiber grating. The difference between the high refractive index and the low refractive index can be quantitatively defined by a physical quantity called *coupling coefficient*. This is a complex physical quantity [26], but its module, which will be noted with the symbol *k* throughout this manuscript, is equal to:

$$k = \frac{\eta \cdot \pi \cdot \Delta n}{\lambda}. \tag{3.2}$$

Moreover, because η in equation (3.2) represents the fraction of the modal power that

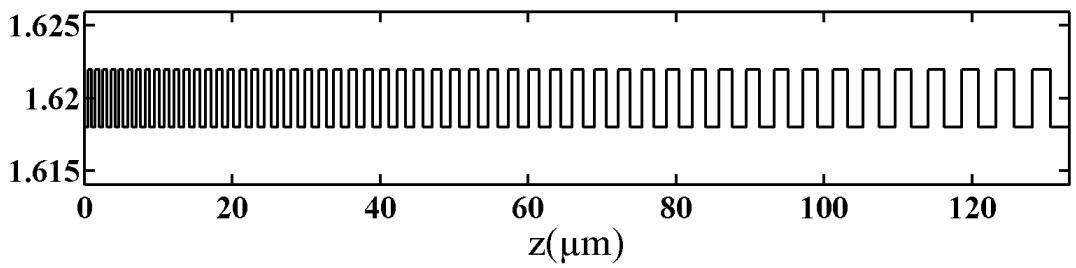

Fig. 3.1 Variation of the refractive index (y-axis) of a linearly chirped grating realized on fiber. This grating has a chirp C=0.04 and a coupling coefficient k=80cm^{-1}.

is contained in the fiber core and because it will be further supposed for the sake of simplification that the entire power is contained in the core, the expression 3.2 simply becomes:

$$k = \frac{\pi \cdot \Delta n}{\lambda}, \tag{3.3}$$

where Δn is the refractive index variation (the difference between the high and the low refractive indices) and λ is the reference wavelength (the wavelength for which the grating was designed to function).

It can be thus said that the most important parameters for a LCG are its chirp and its coupling coefficient. The chirp, along with the grating's length, defines the reflection bandwidth of the grating and it plays a central role in the continuum condition, as previously seen in section 2.2.3. The chirp could have positive values as well as negative ones, as the length of the Bragg periods could be increasing, as well as decreasing along the grating's longitudinal axis.

The coupling coefficient, on the other hand, is very important when considering the reflectivity amplitude of a grating. A greater coupling coefficient means larger refractive index variation, which in turn means stronger reflections inside the grating. That is because each interface between two layers of different refractive indices acts like a dielectric mirror having a reflectivity proportional to the refractive index variation between the two layers, a phenomenon quantified by the Fresnel equations [27]. Unlike the chirp which could practically be fixed at any desired value, the coupling coefficient is strongly limited by the technology used. This will be pointed in the next section, which will present the two different technologies employed in the numerical and experimental parts of this manuscript. There are many applications for which the coupling coefficient is not constant along the length of the grating. This can be useful for example to better adapt a fiber grating with the rest of the fiber, by slowly tapering the refractive index variation toward the tips of the grating. This latter type of grating is called an apodized grating. In function of the form of the envelope of its refractive index variation, the most common types of apodized gratings are the Gaussian and the Raised-Cosine.

3.2 Cavity structures

Throughout the simulations of this and next chapter, and throughout the experimental part of Chapter 5, two types of cavity structures will be referenced, in function of the support medium on which the cavity was created. These will be succinctly presented next, along with some of their technological particularities.

3.2.1 Hybrid cavity

The hybrid cavity studied in this manuscript and presented in Fig. 3.2 is very similar to the laser cavity used by Bergonzo *et al.* and introduced in section 2.2.2. The difference is that this time the LCG is matched to the length of the cavity by the so-called continuum condition (2.8) and that the SOA of Fig. 3.2 is alimented only by a DC current source. The SOA can be inserted in the resonant fiber cavity by splicing the SOA onto the fiber, the new structure being called a *hybrid cavity*, because of the different nature of the active medium comparing to the rest of the cavity.

The cavity can also passively function as a filter, in which case the SOA is missing and the whole cavity is entirely formed on fiber, starting with the metallic mirror in the left, which is coated on the end of the fiber, and finishing with the LCG on the right, which is obtained by exposing the photosensitive core of the fiber to an intense optical interference pattern [28]. Linearly chirped fiber Bragg gratings (LCFBGs) – as LCGs on fiber are sometimes called - found numerous applications in optical communication systems [29] and fiber optical sensor applications [30]. The most outspread of their applications is the *dispersion compensation* of long-haul telecommunication systems [31]. The great limitation of this technology arises from the way in which the LCFBG is engraved onto the fiber, using light interference to

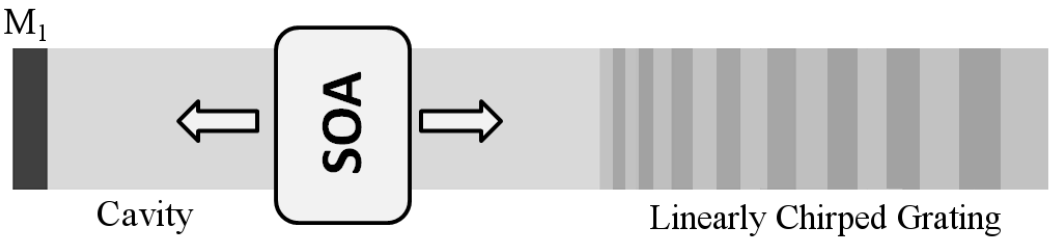

Fig. 3.2 Schematic representation of a hybrid cavity formed between a metallic mirror and a LCG. The active medium consists of a SOA. The name “hybrid” comes from the fact that a SOA is inserted inside the fiber structure.

change the refractive index of the fiber accordingly to the interference pattern created. This technology doesn't permit for great variations of the refractive index, thus it does not permit for high coupling coefficients. The usual technological parameters found in the literature [32] for a LCFBG working in the infrared cite the following usual values for a Bragg period (Λ), refractive index variation (δn) and grating length (L) respectively: $0.5\mu m \leq \Lambda \leq 100\mu m$, $10^{-5} \leq \delta n \leq 10^{-3}$, $1mm \leq L \leq 1m$. This would mean a maximum value for the coupling coefficient of $k \leq 20\text{cm}^{-1}$. This is not entirely accurate, as it is possible to find commercial LCFBGs with coupling coefficients of up to 100cm^{-1}. This is an important fact to note, especially when numerically simulating resonant fiber cavities.

3.2.2 Integrated cavity

The second type of resonant cavity studied in this thesis is the integrated cavity. As its name suggests, this type of cavity is formed on an InP integrated wafer on which several dies have been lithographed, each one having approximately ten different cavities, as represented at the left side of Fig. 3.3. Some of the structures on the die

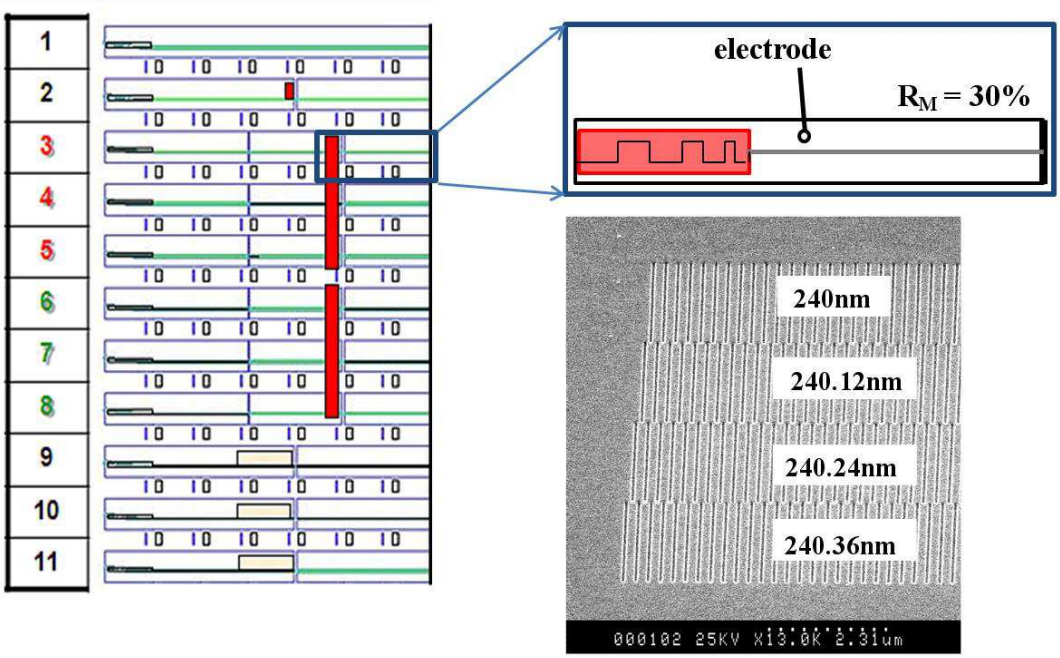

Fig. 3.3 Schematic representation of a die with 11 integrated cavities is drawn to the left. The LCGs are represented with the color red. At the right, a zoom into the structure of an integrated cavity (top) is presented. Also at the right a photo of a series of four Bragg gratings is displayed with the courtesy of Alcatel.

are simple Fabry-Perot cavities formed between metallic mirrors. The ones that are formed between a metallic mirror and a LCG have a red mark on them, corresponding to the place where the LCG is placed. In the example of Fig. 3.3 the semiconductor die at the left is comprised of eleven different cavities, of which one is represented in a magnified form to the right. A metallic electrode is responsible with the current alimentation of the active medium. A photograph showing the precision of the e-beam lithographic process is displayed at the bottom right of Fig. 3.3. In this photo, four uniform Bragg gratings of almost similar periods are shown one next to the other. This type of precision is even more critical when fabricating the LCGs. Considering a reference wavelength of λ=1.5μm and a refractive index for InP of n=3.2 then from (2.6) a reference grating period equal to Λ=230nm is calculated. Another thing to be taken into account is the dimension of the cavity that can be designed onto an InP wafer. Considering the dimension of such a cavity between 200μm and 2mm, it results a value for the spectral chirp C_λ between 0.75 and 7.5nm/μm and for the physical chirp C_Λ between 0.1 and 1nm/μm. This also means that for a typical cavity of length $L_0 = 0.5mm$ each period in the LCG may need to be exactly 0.12nm longer than the one before for the condition (2.8) to be satisfied. It is for this reason that high precision electron-beam lithography is needed, as in the technology displayed in the photo of figure 3.3. It must also be taken into account that InP technology offers the possibility to obtain much higher coupling coefficients (up to 1000cm^{-1}). This is due to the fact that the change in the refractive index is realized by doping. Because the length of an integrated grating is much smaller than that of a LCFBG, higher coupling coefficients are necessary to compensate for the length and to assure the same level of reflectivity in both cases. An experiment involving this type of cavity is presented at the end of Chapter 5. The simulations in this chapter will mostly deal with fiber gratings, but the ones in next chapter will mostly concentrate on the integrated type.

3.3 Numerical methods for grating analysis

Grating analysis can refer to two different types of actions. If given a grating whose parameters are unknown, analyzing it means first finding the parameters of that structure by non-invasive methods. This could be done for example using light

interferometry followed by a layer peeling algorithm [33]. In this manuscript though, grating analysis means already knowing the internal structure of the grating and using the known parameters to numerically simulate the grating's behavior on the computer. For a LCG there are three sufficient parameters which can be used to completely define a grating's spectral response: the chirp C, the coupling coefficient k and the length of the grating L (alternatively, the number of periods M can be used). There are many numerical methods [19] developed in the literature for the purpose of simulating the spectral response of a known grating. The ones that are used the most are the Rouard method [34-36] and a matrix implementation of the coupled mode theory [26, 36, 37]. The coupled mode theory for the case of Bragg gratings with a uniform coupling coefficient will be presented next in section 3.3.1. A generalization of this method for the case of non-uniform coupling coefficient gratings can be numerically solved by a transfer matrix method presented in section 3.3.2. The grating spectra simulated in this manuscript are realized using a more efficient refinement of the matrix method [26, 38] which will also be presented at the end of section 3.3.2.

3.3.1 Coupled mode theory

The coupled mode theory is the most popular approach for analytically solving the spectral response of Bragg gratings, for which it is considered the most intuitive, simple and accurate tool [37]. Although initially conceived for solving the spectra of fiber Bragg gratings having a uniform coupling coefficient, the numerical implementation of this method can be extended to any other type of grating. The derivation of the theory will not be explained in this text, as it is very easily found elsewhere in the literature [26]. It is worth mentioning though the basic assumptions which stand at the core of this method, which are also the general suppositions used in all the simulations presented in this thesis. Firstly, the fiber is considered lossless, thus any type of absorption of light will be neglected in mathematical equations. Then, the electromagnetic field is considered perpendicularly polarized to the propagation axis z, considered also the longitudinal axis of the grating. A forward propagating wave could then be expressed as an exponential of the form $exp[i(\beta z-\omega t)]$ where $\beta>0$ is the propagation constant. The grating is modeled as a periodic

perturbation *n(z)* of the refractive index of the fiber, whose period Λ_B may vary along the grating's length. It is also assumed that the effective refractive index n_{eff} used in the equations of the propagation of light is approximately equal to the weighted average of all the refractive indices along the length of the fiber. The equations will take into account only the *z*-variation of the amplitude for both the forward and the backward propagating waves. Temporal variation is neglected in all of the equations, but is considered implicit. Starting with these assumptions, the final form of the coupled mode theory can now be derived, and the result is displayed in equations (3.4). In this coupled equations *u(z)* and *v(z)* are the amplitudes of the forward, respectively backward propagating waves, and $\beta=\pi/\lambda$ is the propagation constant.

$$\begin{aligned}\frac{du(z,\delta)}{dz} &= +i\beta u + q(z)v \\ \frac{dv(z,\delta)}{dz} &= -i\beta v + q^{*}(z)u\end{aligned} \tag{3.4}$$

Another important quantity is the coupling coefficient *q(z)* which is linked to the refractive index variation. The modulus of *q(z)*, marked with the symbol *k*, was already acknowledged in equation (3.2) as an important parameter of LCGs. The phase of *q(z)* is also linked to the refractive index variation, being a vital parameter in the case of apodized or chirped gratings. For the case of uniform-*q* gratings, which are the gratings with a constant coupling coefficient along their longitudinal axis *z*, the solutions are straightforward and are obtained by directly solving the differential equations resulting from (3.4). The equations thus obtained depend on four constants which can be calculated from the boundary conditions given by knowing the values of the forward and backward propagating waves for the coordinates *z=0* and *z=L*.

3.3.2 Transfer matrix method

The previous solution for a grating having a constant coupling coefficient *q(z)=const* can be numerically extended to any other type of grating. It is sufficient if the varying *q(z)* structure could be replaced by a series of $j=1,2,\ldots,M$ small sections, each section *j* having an approximately constant coupling coefficient q_j and a length Δ equal to $\Delta=L/M$. Then each grating *j* could be represented by a transfer matrix T_j

linking the forward and the backward propagating waves at coordinates $(j-1)\Delta$ and $j\Delta$, as shown in equation (3.5).

$$\begin{bmatrix} u(j\Delta-\Delta) \\ v(j\Delta-\Delta) \end{bmatrix} = T_j \begin{bmatrix} u(j\Delta) \\ v(j\Delta) \end{bmatrix}. \tag{3.5}$$

At the borders between two sections the same pair of propagating waves is referenced by two different matrices (j and $j+1$), allowing us to link all the matrices together in a single matrix product $T = T_1 \cdot T_2 \cdot \ldots \cdot T_{M-1} \cdot T_M$. This total product will connect the propagating waves at position $z=0$ with the waves at $z=L$, as shown in the following equation:

$$\begin{bmatrix} u(0) \\ v(0) \end{bmatrix} = T \begin{bmatrix} u(L) \\ v(L) \end{bmatrix}. \tag{3.6}$$

$$T = \begin{bmatrix} T_{11} & T_{12} \\ T_{21} & T_{22} \end{bmatrix} \tag{3.7}$$

Considering T a matrix of the form displayed in equation (3.7) the reflection and the transmission coefficients could then be calculated as shown in equation (3.8).

$$\begin{aligned} r(\lambda) &= \frac{T_{21}}{T_{11}} \\ t(\lambda) &= \frac{1}{T_{11}} \end{aligned} \tag{3.8}$$

Because each section j is considered having a constant coupling coefficient, the mathematical form of the matrices T_j is found by solving the equation (3.4) for $q=const$. In the general transfer matrix method, the exact function of the refractive index variation, which is accounted by the phase of the coupling coefficient q, is

Fig. 3.4 Schematic representation of the transfer matrix method which was used in this manuscript to numerically solve the spectral response of gratings; a random structure of layers is used for exemplification, as the algorithm could be used for any type of discrete layer grating.

considered to be a sinusoid. However, there is a type of grating for which the form of the transfer matrices becomes very simple. This is the case of the thin film layered grating, for which the transition from a high refractive index to a lower one is realized abruptly. In this model, also called in the literature [26] the *discretized grating model* and represented in Fig. 3.4, the grating is viewed as a succession of layers of different refractive indices. Each layer *j* will have its own transfer matrix (P_j) corresponding to the propagation of light through that layer. In addition, every transition of the refractive index from a layer *j* to the next one will be modeled by an interface matrix (I_j). The mathematical formulas for these matrices are displayed in equations (3.9) and (3.10) respectively.

$$P_j(\lambda) = \begin{bmatrix} \exp(i\frac{2\pi}{\lambda} n_j L_j) & 0 \\ 0 & \exp(-i\frac{2\pi}{\lambda} n_j L_j) \end{bmatrix}. \tag{3.9}$$

$$I_j = \frac{1}{2\sqrt{n_j n_{j+1}}} \begin{bmatrix} n_j + n_{j+1} & n_{j+1} - n_j \\ n_{j+1} - n_j & n_j + n_{j+1} \end{bmatrix} \tag{3.10}$$

It should be noted that the previous model of a grating represented as a sinusoidal (or any other continuous) refractive index variation did not need the presence of the interface matrices (I_j).

The transfer matrix product which links the propagating waves at position *z=0* with the waves at *z=L* as in equation (3.6) can now be defined as:

$$T = I_0 \cdot P_1 \cdot I_1 \cdot P_2 \cdot I_2 \cdot \ldots \cdot P_M \cdot I_M \tag{3.11}$$

The formulas for the reflection and transmission coefficients are the same as previously defined in (3.8) regardless of the grating model used. It can be easily checked that $r(\lambda)\cdot r^*(\lambda) + t(\lambda)\cdot t^*(\lambda) = 1$ for every wavelength λ. Every grating simulation realized in this thesis uses this discretized grating model as its basis.

3.4 Exact mathematical condition

A mathematical approximation of the Continuum condition was presented in section 2.2.3 of this thesis. The continuum resonance condition found in equation (2.8) associated the chirp of the LCG to the length of the cavity. This equation was

obtained after considering that each wavelength is reflected only by its corresponding Bragg period. But this simplification is not entirely true to the reality of things even though at that point it was necessary, as there is no analytical method capable of taking into account all the interactions of light with a multi-layer grating. Now, after introducing the possibility to completely determinate the behavior of light inside the grating by way of numerical methods, such an approximation is no longer necessary. In this section, an exact continuum condition will be sought after. This should be done in relation to the parameters returned by the numerical matrix method used to simulate the LCG. As those parameters are the differences in amplitude and phase of the reflected waves in relation to the incident waves, then an exact continuum condition will be written using those parameters.

In Fig. 3.5 M_1 is a simple dielectric mirror, introducing a phase difference of $\pm\pi$ after reflection which, being independent of the wavelength, could be neglected in future calculations. In the same figure, the round-trip phase shift has been separated in two terms, one term corresponding to the optical path through the cavity (φ_{FP}) and the other to the medium path length of the radiation in the Bragg grating (φ_{BG}). In a resonant cavity the sum of the two is a multiple of 2π for every wavelength λ corresponding to a maximum of emission (resonance condition). In our case, φ_{BG} should have such a value that the total round trip phase shift ($\varphi_{FP} + \varphi_{BG}$) will remain a multiple of 2π on a large bandwidth. In other words, the variation of φ_{BG} should cancel the variation of φ_{FP} with λ:

$$d\varphi_{BG}/d\lambda = -d\varphi_{FP}/d\lambda. \tag{3.12}$$

If (3.12) is true for a large enough bandwidth, our structure will show a continuum behavior. Instead of using phase derivatives, equation (3.12) can be written around another physical quantity called the group time delay (*GTD*) which in certain cases has a more intuitive interpretation. The *GTD* is a quantity characterizing optical

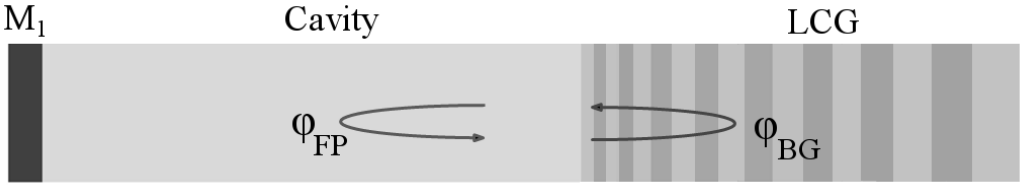

Fig. 3.5 Representation of a resonant cavity realized with a LCG, in which the total round trip phase shift has been divided between the Bragg grating (φ_{BG}) and the rest of the cavity (φ_{FP}).

systems and has a mathematical form defined by (3.13), where φ is the phase shift introduced by the propagation through the structure. Depending on where the phase difference is measured in relation to the incident wave, there can be a *GTD* corresponding to the transmission through the structure, and another *GTD* corresponding to the reflection. Because all gratings discussed in this paper function as cavity mirrors, what will be important to us is the *GTD* corresponding to the reflection on the gratings.

$$GTD = \lambda^2/(2\pi c)\cdot d\varphi/d\lambda \tag{3.13}$$

It can be shown that when all the wavelengths λ in a beam are travelling the same optical path through a structure, in that case the *GTD* is equal to the transit time through that structure and has a value independent of λ. Because the LCGs are structures in which the optical path is wavelength-dependent, in this case the intuitive meaning of equation (3.13) no longer holds true and we have to contend ourselves with solving the mathematical formula.

The group time delay (*GTD*) of a radiation λ reflecting on a grating is proportional to $d\varphi/d\lambda$ as shown in (3.13). It can be stated from (3.12) that the *GTD* of the designed grating must have the same absolute value and an opposite sign compared to the *GTD* of the cavity. This condition must be true no matter the phase formalism adopted as long as we keep consistent with it in all simulations and calculations. In the numerical simulations by the transfer matrix method (TMM), the phase shift of a radiation λ after propagation on a distance L through a medium of refractive index n is considered equal to $\varphi(L) = -2\pi nL/\lambda$. In this phase formalism, the GTD of the cavity is always positive. It follows from (3.12) that the GTD of the Bragg grating (as simulated by TMM) should correspondingly have a negative sign in the desired bandwidth:

$$GTD_{BG} < 0. \tag{3.14}$$

The purpose of the simulations presented in the next section was to find a LCG having a negative group time delay. It is obvious from the previous equations that a grating with a negative *GTD* could realize the continuum condition only with a matching cavity having a positive *GTD* of the same absolute value. This being told, it is easier to firstly find a grating capable of canceling the resonant modes of a cavity and then from its parameters to calculate the length of that cavity than the other way

around. Thus, a formula linking the *GTD* to the cavity length will be sought in the remaining part of this section. Firstly, we will rewrite the resonance condition for a radiation of wavelength λ without linking it to the specific Bragg period corresponding to that wavelength as we did in section 2.2.3:

$$n_0 L_0 + n_{eff}\, z_{eff}(\lambda) = m\frac{\lambda}{2}. \tag{3.15}$$

In equation (3.15) $z_{eff}(\lambda)$ is a position inside the grating from where the radiation of wavelength λ seems to be reflected. In fact the radiation λ is reflected at every interface between two layers of different refractive indices, but its resulting phase, measured at the entry point of the grating, could be interpreted as resulting from the reflection of that radiation at a specific location in the grating. By multiplying (3.15) with (-4π), the result is the equation (3.16) which highlights the phase terms in the resonance condition:

$$-\frac{4\pi}{\lambda} n_0 L_0 - \frac{2\pi}{\lambda} n_{eff} \cdot 2 z_{eff}(\lambda) = -2m\pi. \tag{3.16}$$

The second term in equation (3.16) represents the phase shift $\varphi(\lambda)$ of the radiation of wavelength λ after passing through the grating, and its value is conveniently returned by the TMM method. That is why we chose to multiply (3.15) with (-2π) instead of (2π). The minus sign forces us to keep consistent with the phase formalism chosen for the matrix method and presented in the previous section.

$$\varphi(\lambda) = -\frac{2\pi}{\lambda} n_{eff} \cdot 2 z_{eff}(\lambda), \tag{3.17}$$

By replacing (3.17) in (3.16) the resonant condition becomes:

$$-\frac{4\pi}{\lambda} n_0 L_0 + \varphi(\lambda) = -2m\pi. \tag{3.18}$$

In the first term of equation (3.18) we can recognize the round-trip phase of the radiation through the cavity (without the grating). After its derivation in function of λ, the continuum resonance condition could be written as in (3.19).

$$\frac{d\varphi(\lambda)}{d\lambda} = -4\pi \frac{n_0 L_0}{\lambda^2} \tag{3.19}$$

By introducing (3.19) in the formula (3.13) of the *GTD* and highlighting L_0 from that equation, we arrive at the formula which relates the length of the continuum resonant cavity with the negative *GTD* of its reflecting grating:

$$L_0 = \frac{c}{2n_0}(-GTD_{BG}) \tag{3.20}$$

3.5 Results

Considering the theoretical approach expressed in the previous section, designing a continuum resonant cavity is equivalent with searching for a reflecting structure having a constant negative *GTD* on a certain wavelength interval. After finding this type of structure, we can use it to fabricate a continuum resonant cavity with a length equal to the value of L_0 calculated from equation (3.20). The idea of this chapter was to use a LCG as such a negative *GTD* reflector. The three parameters which can be varied in LCGs (length, chirp and coupling coefficient) offer us a vast number of possible gratings. Our objective was to find under which conditions a LCG may have a negative *GTD* in its reflection bandwidth. Thus, this section will present the influence of the three constructive parameters of a LCG on the group time delay, when the LCG is functioning as a reflector.

In the following figures of this section, the values for the group time delays and the reflectivities are calculated each time for a wavelength $\lambda=1550nm$, situated exactly at the center of the bandwidth for each simulated grating. The grating's bandwidth *B* varies each time with the chirp *C* and the grating length *L*, according to the simple formula $B = n_{eff} \cdot L \cdot C$, where n_{eff} is the effective refractive index of the grating.

For the beginning let us consider in Fig. 3.6 the influence of chirp on the *GTD* of a LCFBG of standard length *L=1cm*. In the same figure, the values of the corresponding reflectivities are plotted in blue. The two separate plots are for two limit values of the coupling coefficient. To the top there is the case of a high-*k* grating characterized by a *100%* reflectivity for chirps as high as *20nm/cm*. The reflectivity (blue line) drops above this value of the chirp: because of fewer Bragg periods found in the vicinity of a wavelength λ, the sum of the separate reflections for that wavelength drops. Regarding the *GTD*, gratings with low chirps have many Bragg periods one after the other reflecting the same narrow spectral bandwidth. This means that a wavelength situated at the center of this bandwidth will not travel much of a distance into the grating, being reflected right at the beginning of the grating.

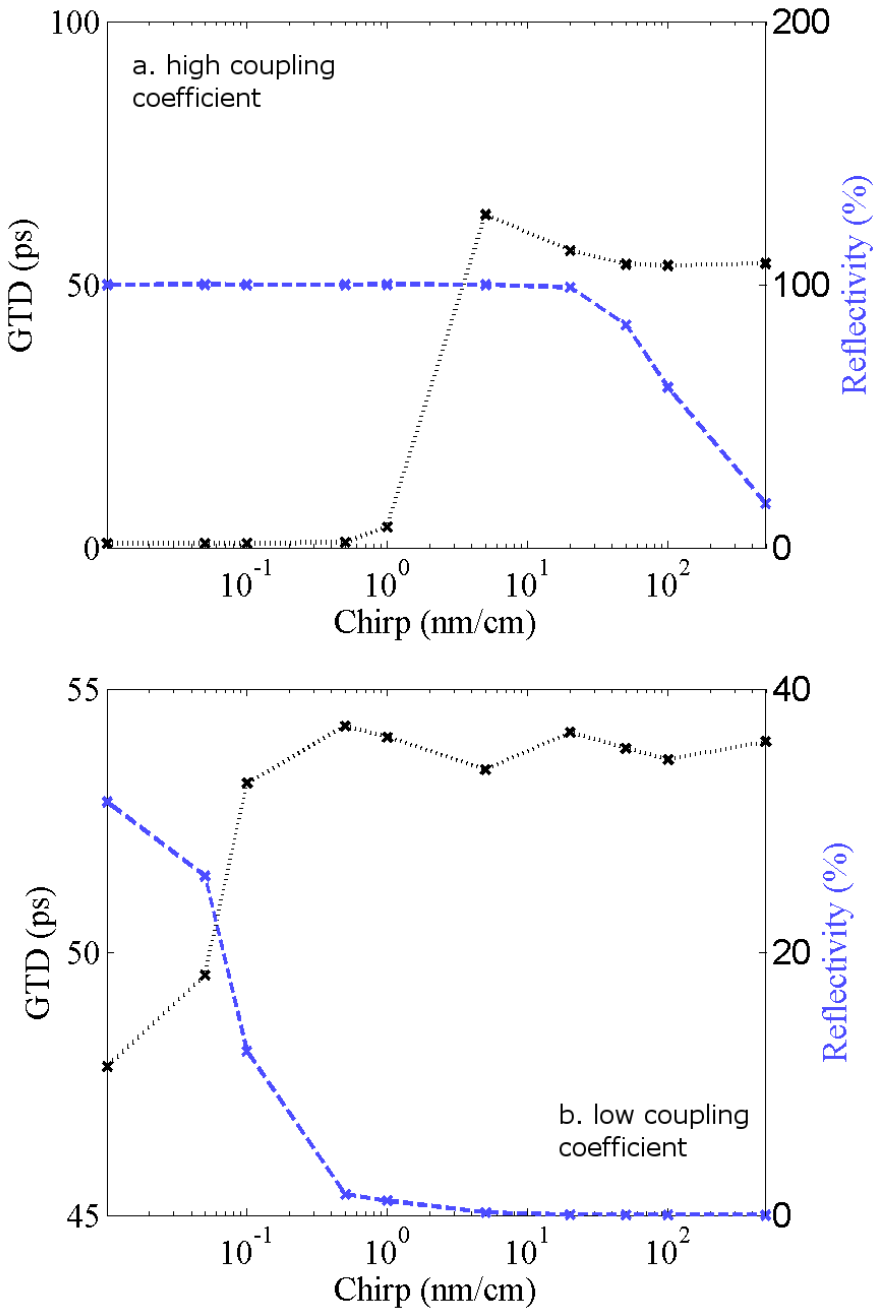

Fig. 3.6 Influence of the chirp on the group time delay (GTD) of a LCFBG of length L=1cm and coupling coefficient of: a. k = 100cm^{-1} and b. k = 1cm^{-1}. The GTD is represented by a black pointed line and the reflectivity in a dashed blue line. Both the reflectivities and the GTDs are calculated for λ=1550nm at the center of the grating's bandwidth.

This reflection is similar to that coming from a strong mirror placed near the beginning of the grating, entailing a value close to zero for the *GTD*. While increasing the chirp and thus the bandwidth, the first periods of the grating will start reflecting less and less the wavelength corresponding to the center of this bandwidth. This will allow the radiation having that wavelength to penetrate into the grating

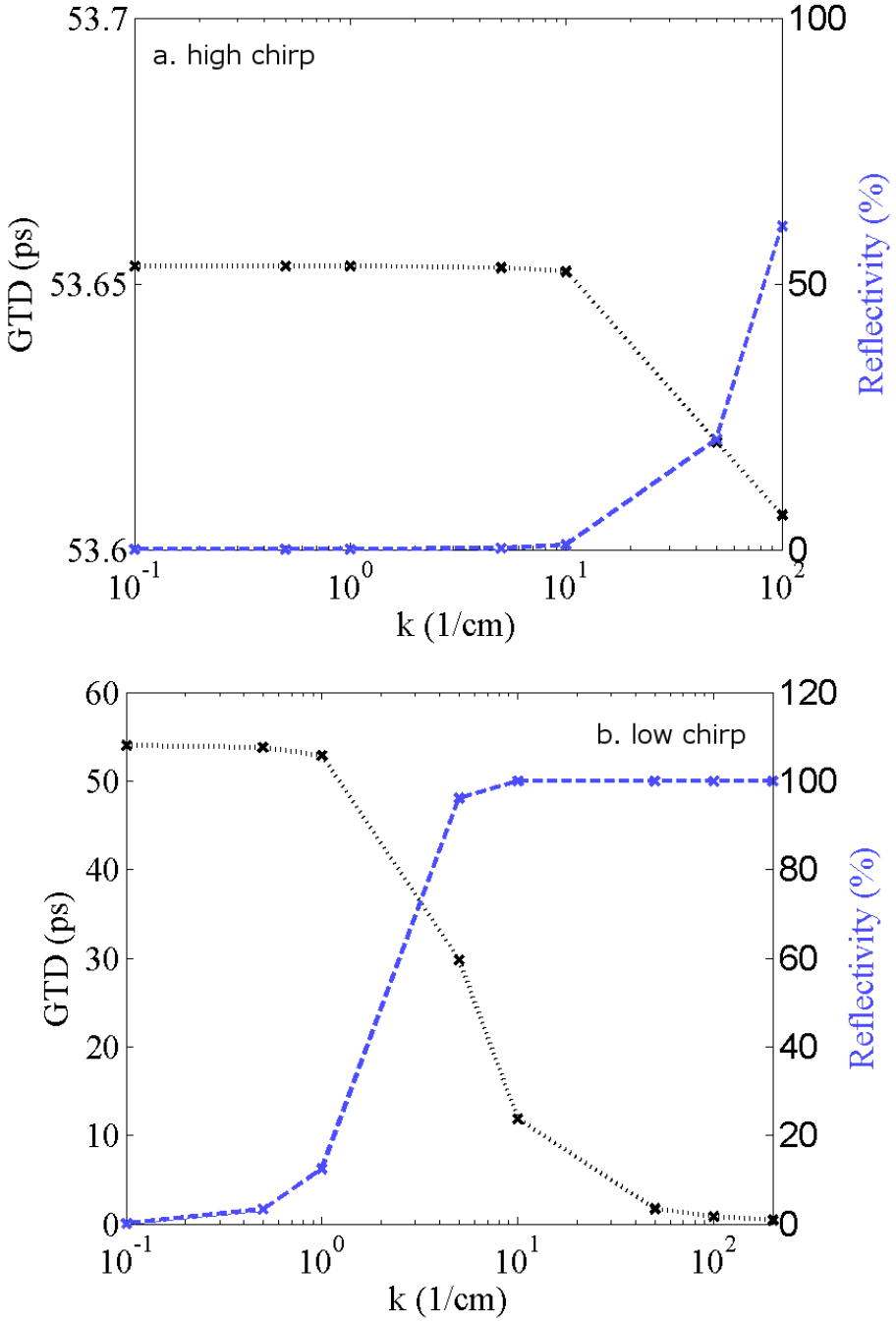

Fig. 3.7 Influence of the coupling coefficient *k* on the group time delay (*GTD*) of a LCFBG of length *L=1cm* and chirp: a. *C=100nm/cm* and b. *C=0.1nm/cm*. The *GTD* plot is colored black, while the reflectivity values are in blue. The values are calculated for the center of the grating's bandwidth.

more, which in turn increases the value of the *GTD*. The increase is limited at a value corresponding to that wavelength being reflected only in the immediate vicinity of the central Bragg period of the grating, at a position $z_{eff} = L/2$. Increasing the chirp even more beyond this value will not modify the *GTD* for this central wavelength. Looking at Fig. 3.6(b) a plummet of the reflectivity comparing to the previous case can be observed, which is due to the low coupling coefficient used. Because of this

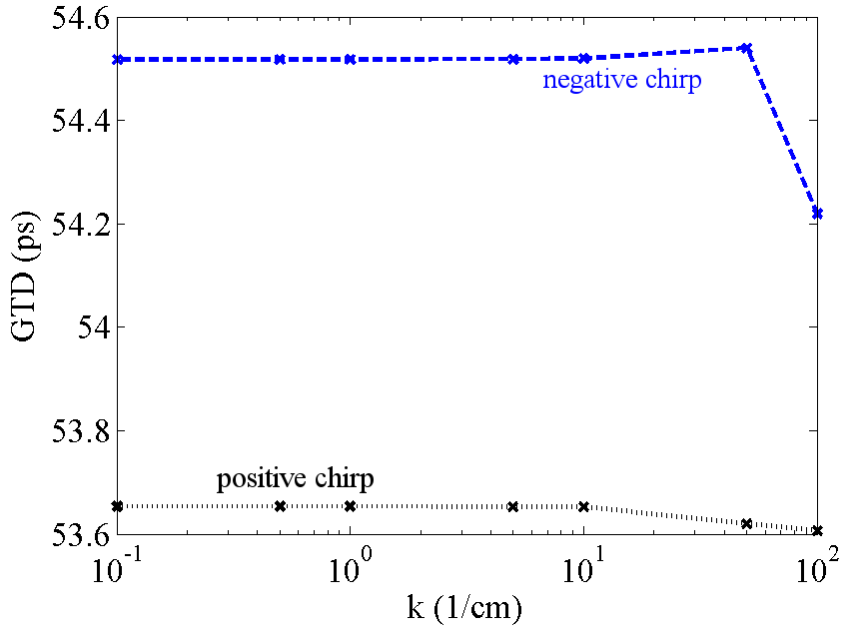

Fig. 3.8 Influence of the chirp's sign on the group time delay (*GTD*) of a LCFBG of length *L=1cm*. The variation of *GTD* with *k* is studied for two different gratings with chirps *C=100nm/cm* (black) and *C=−100nm/cm* (blue).

low reflectivity, the central wavelength manages to reach all of the Bragg periods of the grating in spite of the grating's low chirp. The effective (weighted average) reflection coordinate is very close to $z_{eff} \approx L/2$. When increasing the chirp, the reflection bandwidth of the grating increases around the central wavelength, but the number of periods capable of reflecting it decreases correspondingly. At high chirps, only the central Bragg period situated at $z_{eff} = L/2$ will reflect its corresponding wavelength, similarly to what was described previously for a high-*k* grating. This means that for the case of high chirps, the coupling coefficient has little to no influence on the *GTD*.

This last point can also be noticed in Fig. 3.7(a) where the influence of the coupling coefficient on the *GTD* is analyzed in the case of a fiber LCG of elevated chirp. While the coupling coefficient was increased *1000* times, the variation in the *GTD* was no higher than *0.1%*. On the contrary, for the case of a low chirped grating, the variation of the *GTD* with the coupling coefficient is very important, as shown in Fig. 3.7(b). Despite its large variation with *k*, the *GTD* only asymptotically approaches zero and it does not reach negative values. As explained earlier, every Bragg period of a low chirped grating will be able to reflect the central wavelength of its bandwidth. When the coupling coefficient is low, the radiation is reflected from every period of the entire grating, having an effective (average) reflection coordinate

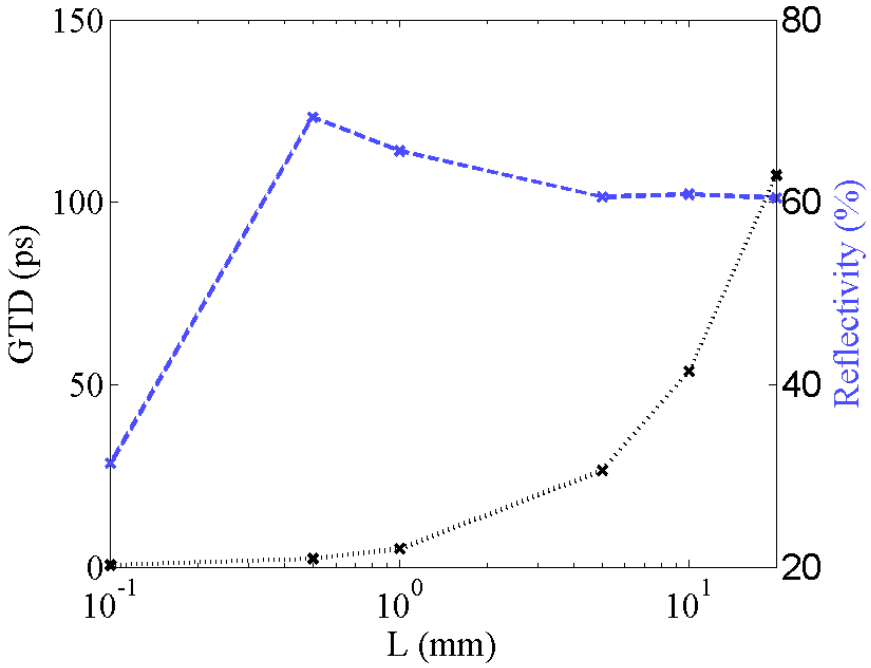

Fig. 3.9 Influence of the grating's length on the group time delay (black) and central reflectivity (blue) of a fiber LCG of chirp *C=100nm/cm* and coupling coefficient $k=100cm^{-1}$.

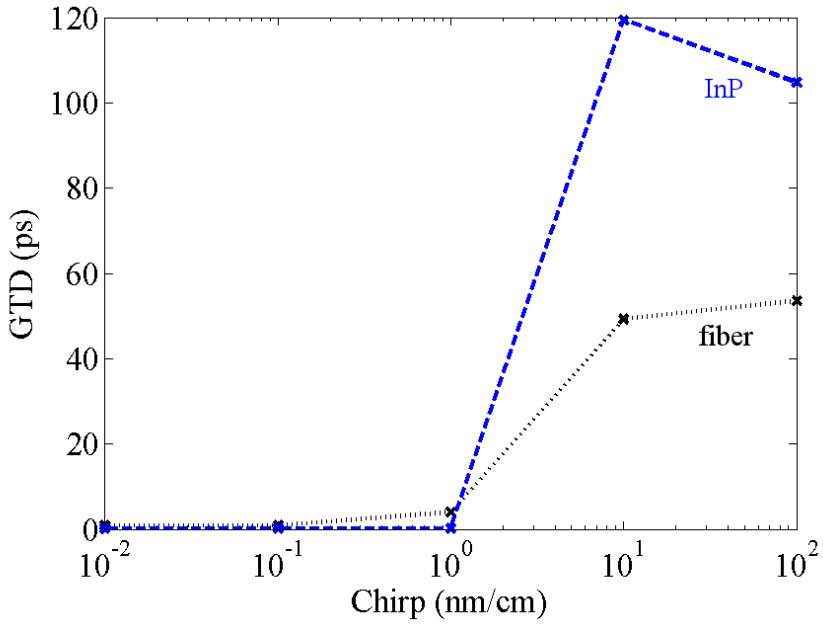

Fig. 3.10 Influence of the grating's medium on the group time delay (*GTD*) of a LCG of length *L=1cm*. The integrated grating is represented in blue, while the fiber LCG is in black. A coupling coefficient of $1000cm^{-1}$ was used for the InP grating, while for the fiber one a $k=100cm^{-1}$ was used.

equal to $z_{eff} \approx L/2$. When the coupling coefficient increases, the radiation will be increasingly reflected by the first periods of the grating and thus its effective reflection coordinate z_{eff} will decrease accordingly.

The degree of accuracy of the physical hypothesis standing at the base of the Continuum project and explained in section 2.2.3 is tested in Fig. 3.8. It was considered that, given a positive chirped LCG, the short wavelengths will be

reflected before the longer ones, by the Bragg periods situated at the beginning of the grating. If this was true, then reversing the grating and thus creating a negative chirped LCG would make the longer wavelengths to be reflected before the shorter ones. This variation of the effective reflection coordinate when turning the grating from the positive to the negative chirp must have a pronounced effect on the *GTD*, but this effect is not seen for the central wavelength. As noticed in Fig. 3.8 only a small difference of *1ps* was obtained by turning a *C=100nm/cm* fiber grating of length *L=1cm* with the other end first.

In all of the simulations the grating acted as a mirror which was placed inside the grating at different positions $z_{eff}(C, k) \in (0, L/2)$ in accord with the supposition of equation (3.17). On the contrary, if noticeable differences in effective reflection coordinates of different wavelengths were possible as supposed in section 2.2.1, then we would have seen a much higher difference between the two *GTDs* of Fig. 3.8 and a negative $z_{eff}(C, k)$ for certain values of *C* and *k* in the case of a positive chirped grating.

The dependence of the *GTD* (calculated for the central wavelength) with the grating's length is shown in Fig. 3.9. At first the behavior of the reflectivity does not seem very intuitive. After a certain length the reflectivity will start to decline with the length of the grating. This happens because as we increase the number of periods by adding small Bragg periods to the left and large Bragg periods to the right, newly added Bragg periods may reflect again the central wavelength, but this time in phase opposition to the initial periods of the grating. As for the GTD, increasing the length will always push further away the position of the effective reflection coordinate $z_{eff} \approx L/2$.

The figures presented in this section only displayed the *GTD* results for some limit cases (high chirps *vs.* low chirps, high *k vs.* low *k*, etc) of fiber gratings. Other intermediate cases (like average chirps and coupling coefficients) were neglected for not bringing anything new to the observations already made. The same series of simulations was done for the case of *InP* gratings with no better results (Fig. 3.10). The advantage of the integrated technology is the use of higher coupling coefficients. This in turn translates in smaller *GTDs* for small chirps, when the reflection is realized close to the beginning of the grating ($z_{eff} \approx 0$). Because InP has a much

higher refractive index then a fiber grating, its *GTD* will also be much higher when increasing the chirp and approaching an effective reflection coordinate of $z_{eff} \approx L/2$. This is caused by an increase in the optical path of the light, even if the reflection happens at the same physical coordinate in both mediums.

The discussions in this chapter are original analyzes of the behavior of light in a LCG from the point of view of the *GTD*. Sadly, our objective of finding a reflecting grating with negative *GTD* has not been achieved. This may be because of the limits in the degrees of liberty offered by a linearly chirped grating, or it may be because of a fundamental physical limit inherent in the process of reflection. Both of the possible causes will be analyzed in the next chapter, where the search for a negative GTD grating will be greatly extended.

Chapter 4

Genetic Gratings

In this chapter the search for an already existing negative *GTD* grating will be replaced by the design of such a grating. The structures presented in this chapter and their associated spectra are all original work. We will start with an introduction into the necessity of using random gratings and then continue with a review of the synthesis methods capable of producing such structures. The results are presented for both cases of fiber and InP gratings. Simulations of grating spectra are followed by those of their corresponding cavities. The chapter will end with a second synthesis method offering a mathematical justification for the impossibility of obtaining a perfect grating.

4.1 Random gratings

While we have searched for a solution to the problem of a negative *GTD* grating in the previous chapter we have limited ourselves only to the technologically available space of LCGs. The dependence of the *GTD* on the three fabrication parameters was calculated and explained. It was observed that no matter the parameters used, it was never possible to obtain a negative *GTD* in the center of the reflection bandwidth of a LCG. The idea of this chapter is to extend our search indefinitely to any type of reflecting structure realized by the variation of the refractive index. This type of structure for which there is no simple analytical function linking one layer of the grating with the other layers will be called a *random grating*. As shown in Fig. 4.1 there can be three types of random gratings, in function of the parameter which is considered random. The first type, in which the width of each layer is independent of the widths of the other layers, is similar to a series of LCGs randomly chirped across the length of the grating. The second one, in which the refractive index varies randomly across the grating, is similar to a series of LCGs with a randomly varying

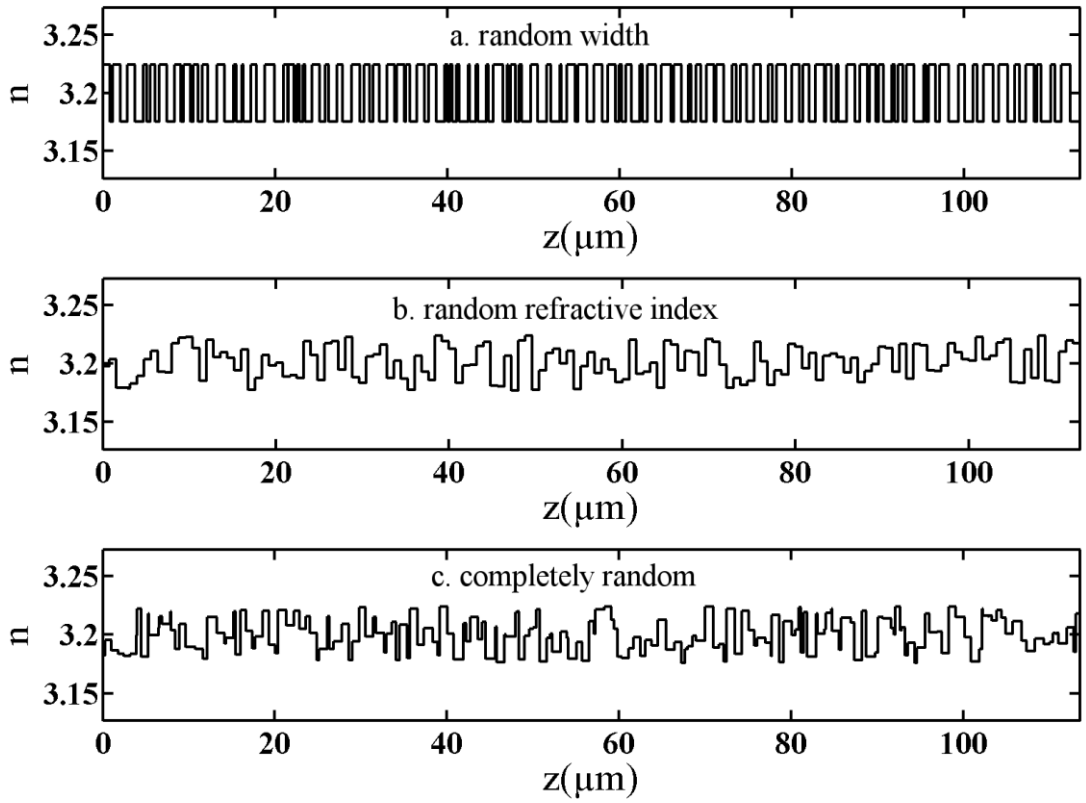

Fig. 4.1 Three examples of different types of InP random gratings: a) a grating in which the width of each layer is random; b) a grating in which the refractive index of each layer has a random value; c) a grating in which both the width and the refractive index of each layer are random

coupling coefficient. The third one will be a combination of the first two. In this chapter the focus will be led on the first type, as it was considered easier to be fabricated than the other two. But no matter the type chosen, each time the number of possible gratings resulted is unlimited. Even when imposing strict limits to each parameter's possible variation, the number of possible gratings still remains enormous. For example, let us consider that the width of each layer will have only p possible values. Because there will be M independent layers, the number of possible gratings becomes equal to p^M which will take very long to be entirely exhausted considering that there will be at least $M>200$ layers needed to construct a grating. Choosing the minimum value for the number of possible values for each layer of only $p=2$ and a required simulation time for each possible grating of at least $t^*=2s$ then a total time of $t^*\cdot p^N > 10^{50} years$ will be needed to cover all the possible combinations of layers. The approach of calculating the *GTD* and the reflectivity only for a centered wavelength used in the previous chapter does no longer work for the case of random gratings which do not have a specific bandwidth. Thus the time t^* was the time needed to calculate the spectrum of one grating over a bandwidth of *30nm* with a precision of *0.1nm* with a *3GHz* processor. Because of this time limitation, an exhaustive search for a grating having a negative *GTD* can not be done for the case of random gratings. The right approach in this case is to try to synthesize such a grating ourselves. The methods described in the next section were created specially for such an endearing feat.

4.2 Numerical methods for grating synthesis

The problem of finding a grating corresponding to a desired transmission or reflectivity is solved by different methods throughout the literature: a numerical solution to the coupled Gel'fand-Levitan-Marchenko integral equations [39], a Genetic Algorithm [40], Discrete Layer Peeling [41] or Fourier transform [42]. Applications of such methods are found wherever the classical type Bragg gratings (uniform or linearly chirped, with or without apodization) do not deliver satisfying results. Lower side lobes, lower pass band ripple and lower dispersion are some of the improvements obtained after using this type of novel structures over their LCG counterparts. All this comes with a cost. The gratings returned by the above synthesis

methods are sometimes difficult to be realized physically comparing to a LCG, as their refraction index variation has sometimes seemingly random shapes. This disadvantage will also be present for the case of the structures presented in this chapter.

First one of the methods listed above, based on the coupled GLM equations, is not exactly useful for the design of a Bragg grating, but for a corrugated filter. A corrugated filter is similar to a Bragg grating, except that the reflections are caused not by a variation in the refractive index in the volume of the structure, but by a variation in the form of its surface.

The genetic algorithm and the Fourier transform methods have been previously used for the design of Bragg gratings of continuous refractive index variation. As explained in section 3.3 the spectra of gratings with a continuous refractive index variation are numerically obtained by a TMM approximation of the coupled mode theory. For the case of these gratings, it is the envelope of the refractive index or the coupling coefficient *q(z)* which will be synthesized by the algorithms.

The Discrete Layer Peeling method is different than the others, as it was specially created for the synthesis of discrete Bragg reflectors, characterized by an abrupt refraction index variation when passing from one layer to the next one, as in the case of the gratings simulated in this manuscript. The spectra of such thin film gratings are obtained by an adaptation of the TMM method which was explained in the final part of section 3.3.2.

One of the original points of this chapter is the adaptation of the genetic algorithm for the case of thin film gratings. It is the best tool to optimize a grating, when an exact solution is not possible. For our specific objective of a continuum reflector, two simultaneous conditions on two spectral parameters (*reflectivity* and *GTD*) will be required. As it will be soon noticed in the simulations, the two conditions are mutually exclusive, which forces us into adopting the optimizing properties of the Genetic Algorithm. On the other hand, the Discrete Layer Peeling method, which was expressly created for the case of discrete gratings and which is based on the discrete Fourier transform of the filter's response, will be recommended when an exact solution is possible.

4.2.1 Genetic Algorithm

The genetic algorithm is a fast way of approaching optimal solutions when the space of variables is so large that an exhaustive search of all the solutions is impossible. One of the algorithm's disadvantages is that it does not find the best solution to a problem, but only local optima depending on the random initial conditions used. Regarding its use in the design of Bragg gratings, it is employed in the literature not for the synthesis of discrete layer gratings, but for that of continuum refraction index gratings [40]. Its former application was thus more fiber-oriented, as in fibers the transition from a lower refraction index to a higher one is smoothly realized. On the contrary, the genetic algorithm developed in this thesis will be applied exclusively to discrete layer gratings and will be thus more oriented towards the design of integrated structures.

The concept of a genetic algorithm was theorized by Holland [43] in 1975. Inspiring himself from the natural mechanisms of selection specific to the animal world, he postulated the existence of similar mechanisms for the selection of artificial created systems. In the natural world, the genetic algorithm has its counterpart in the natural selection mechanisms described for the first time by Darwin [44] in his book from 1859. Basically, what Darwin says is that in every given species, the best of individuals give rise to more offspring than the weakest of the individuals in that species. The best of individuals are the ones more able to survive to the present set of environmental conditions and more able to find mating partners. Translating this in the technical language which will be used further on in this chapter, in every given generation a function can be applied on the characteristics of every individual in a species, calculating that individual's chances of survival and mating. This function will be called a fitness function and in the natural world it must take into consideration both the individual's capacity to survive to sexual maturity and also its capacity to attract opposing-sex partners. The latter consideration will be applied almost exclusively to males, as in most animal species all the females will be able to give birth to offspring once reaching sexual maturity, but only a few best males are able to do the same. The difference is that while the females are very limited in the amount of offspring they can give birth to because of the amount of time involved in

the production of just one sexual cell, the best fitting males are limited only by the number of females in the population. In the extreme case of the elephant seals for example, 4% of males are responsible for 88% of the observed copulations [45]. This 4% of the males, called the alpha-males, are the ones who are the strongest and thus able to chase any other male from the territory of their harem. Even if this is an extreme example in the animal world, it is by no means a singularity. Even in the human species where monogamy is culturally imposed in many parts of the world, there are societies in which a few alpha-men account for the majority of offspring. This is the case for example with the Genghis-Han lineage [46] in which case approximately 8% of the men in Asia have a common ancestor from a thousand years ago. This accounts for 0.5% of the world population originating in the same male individual of a thousand years ago. Other known lineage in Mongolia comes from Giocangga [47]. In another study, one in five males of northwestern Ireland seems to have a common male-ancestor from the medieval dynasty of Uí Néill [48]. It is obvious that the fitness function, which is responsible with calculating the probability for reproduction of every individual, has in the case of human species a very important social component. In the monogamous societies, the laws are in such a way that they even the chances of reproduction of individual males, creating thus an artificial homogenization of the possible values returned by this function. On the contrary, the fitness function has accentuated peaks and great value disparages in such animal species as the elephant seals or the birds of paradise [45].

Continuing with the explanation of the natural selection, the selected individuals pass their characteristics to next generations by the intermediate of genes. In fact the majority of an individual's external characteristics whether physical or behavioral, are encoded in the genes, which are small fragments of code situated at the core of each of their cells. When a male sexual cell combines with a female sexual cell a new individual is born, taking half of its characteristics from the father, and the other half from the mother's sexual cells. The new combination of genes may yield external characteristics which are considered better than the characteristics of its parents, in which case the value returned by the fitness function when applied on the child will be higher than the corresponding values of his parents. When the maximum fitness function remains constant over a great number of cycles, it may mean that the new individuals of a specific species converged to have the same genes, representing the

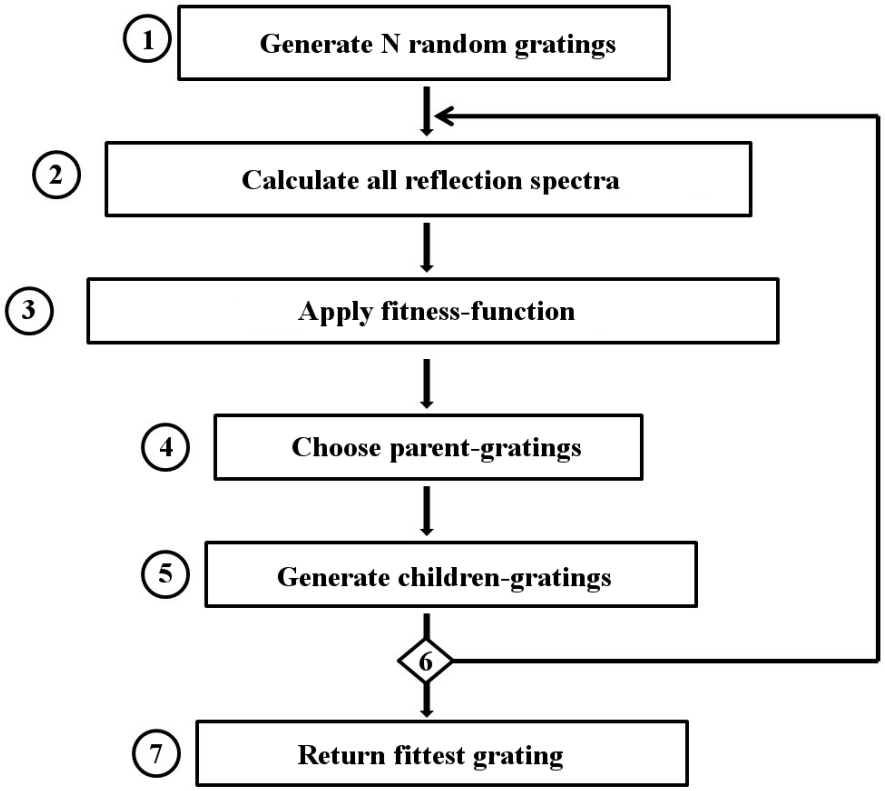

Fig. 4.2 Diagram of the genetic algorithm used throughout this manuscript for the generation of Bragg gratings.

characteristics of the ideally-fitted individual in that species. In the natural world though, the fitness function undergoes a continuous evolution determined by environmental dynamical phenomena like climatic and ecosystem changes. Regarding the temporal evolution of the number of individuals in a certain species, the natural selection theorem was discussed supposing this number a constant from a generation to the next one. This supposition is based on the fact that resources of food and shelter are always limited in real life, which brings about an effect of saturation in the number of individuals a species can have.

It is not complicated to pass all these observations taken from the natural world and to translate them into an algorithm capable of synthesizing artificial structures. The genetic algorithm which will be addressed next will also be used for the generation of all the random gratings displayed at the end of this chapter. Differences between this method and the original algorithm described by Skaar and Risvik [40] will be summarized at the end of this section.

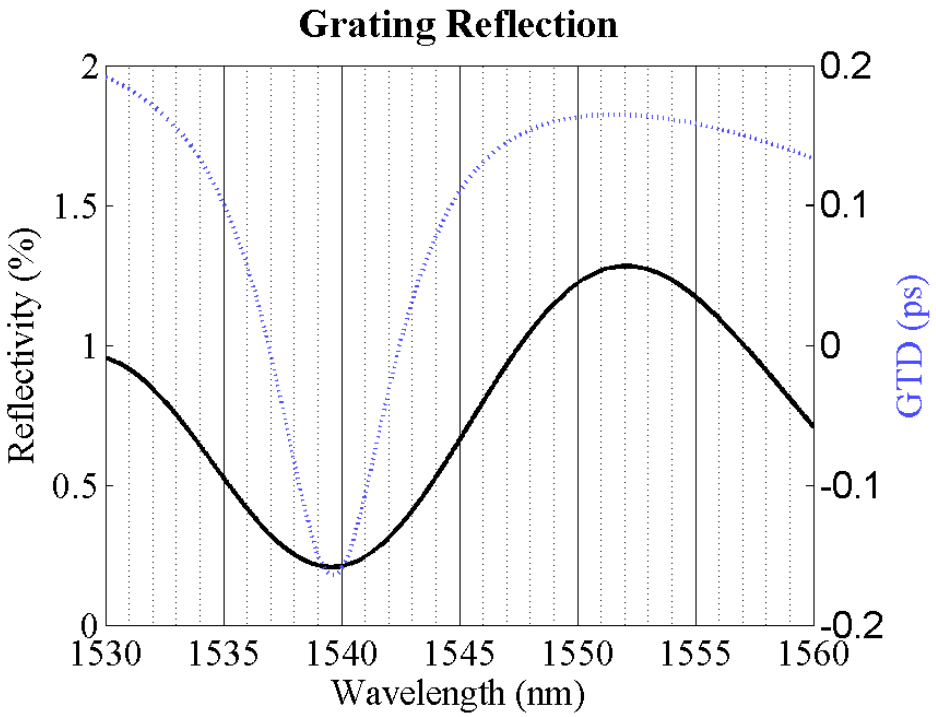

Fig. 4.3 Spectrum of an individual grating, along with the mesh used for the calculation of the fitness function corresponding to that individual grating.

Figure 4.2 displays a block diagram of the algorithm used for the synthesis of all the gratings presented in this manuscript. The first step in this process is the generation of N random gratings, usually random-width gratings. Each grating will have the same number M of layers. Making an analogy to the natural selection, the gratings represent the individuals and the layers represent their genes. Because all individuals of a species have the same number of genes, the gratings will also have the same number of layers. In the general case, each layer will have its own specific refractive index and thickness, which makes the genetic space practically infinite.

For exemplification, the algorithm will be explained only for the case of random-width gratings. In this case, each layer has its own thickness value $w_{i,j}$, where i represents the index of each grating (i=1,2,..,N) and j the index of each layer (j=1,2,…,M) in a specific grating. The refractive index will have only two values: n_1 (for odd layers) and n_2 (for even layers). The totality of layers is analogue to the gene pool of that species.

The second step of the algorithm is represented by the calculation of the reflection spectra of all the gratings by the TMM method. Its application to discrete gratings was explained in section 3.3.2. Analogous to the natural selection, the spectrum of

each grating corresponds to the phenotype of an individual. The phenotype is the totality of observable characteristics or traits of an individual. It is in fact on these observable characteristics that the natural selection works its magic and not directly on the genes, which are only the unseen code producing those characteristics. Of interest to us are the values of reflectivity and *GTD* for a certain number *P* of wavelengths in a bandwidth interval. In Fig. 4.3 for example the spectrum of a grating is calculated for *P=31* different wavelengths in the desired continuum interval. The values of the reflectivity *R* and *GTD* at those specific wavelengths will represent the phenotype of that grating.

At the third step of Fig. 4.2, the fitness function *F* will assign to each phenotype (spectrum of grating *i*) a fitness value f_i, representing, as in the natural selection scenario, the grating's ability to give offspring in the next generation of gratings. Gratings with high values of f_i will yield a great number of offspring, whereas those with low f_i will very likely have none. That is why choosing a good fitness function is a key element in successful grating design. For the case presented in this manuscript, an ideal fitness function should reward simultaneous encounters of a constant negative *GTD* and a high reflectivity over a large bandwidth. A simple fitness function used in our simulations is defined in (4.1).

$$F = \sum_{p=1}^{P} R_p \cdot \left| GTD_p \right|, \qquad for\ every\ GTD_p < 0. \tag{4.1}$$

The summing in (4.1) depends on the number *P* of wavelength sampling points used by the algorithm and it takes place only for the meshing points for which we have a negative $GTD_p < 0$. R_p represents the reflectivity of the grating for those specific wavelengths. The values f_i obtained after applying the function *F* to each grating *i* are then normalized and used as probabilities for each grating to find itself as a parent in the next generation of gratings.

The choice of parents is realized at the forth step of Fig. 4.2 through a roulette wheel type algorithm. On a virtual wheel of fortune, each grating occupies a slice proportional to its fitness function. The wheel is turned and it is then stopped after a random time interval. The grating thus picked will be copied in the vector of parent-gratings. The wheel is turned again until the size of the parent-vector reaches *N*. It is obvious that the gratings with higher values of the fitness function will be extracted

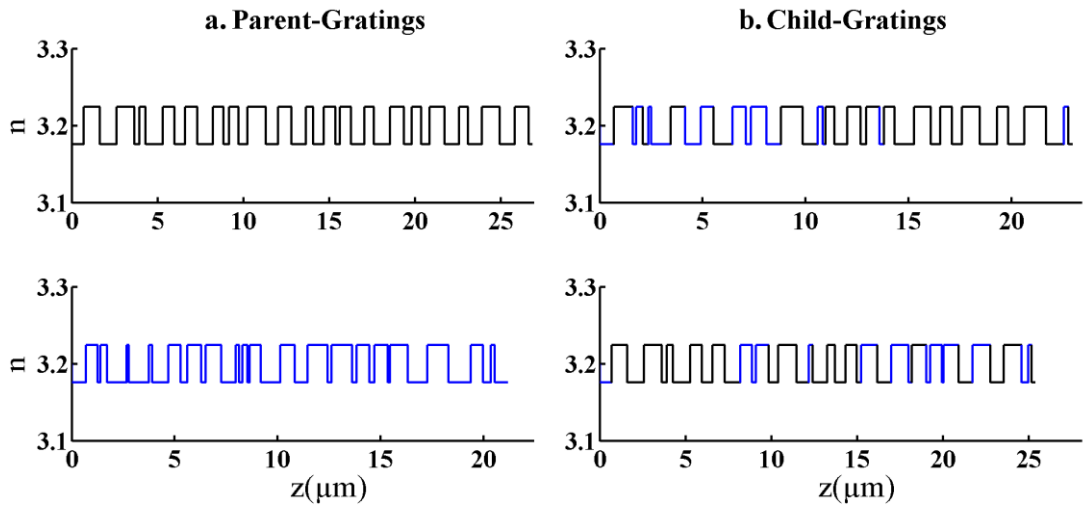

Fig. 4.4 Generation of two child-gratings after applying the uniform crossover method on two parent-gratings

more than once by the algorithm. The gratings will then be coupled two by two inside the parent-vector, in the process creating *N/2* pairs of parent-gratings. It can now be proceed to the next stage of the algorithm, which is the generation of child-gratings.

At the fifth step of Fig. 4.2 each pair of parent-gratings will give rise to a new pair of child-gratings. There are many methods of combining the layers of the parent-gratings to obtain the children, but one in particular was extensively used in this paper, namely the *uniform crossover*, which most resembles the way genes combine in natural sexual reproduction. This method consists in choosing for each layer *j* of a child-grating the corresponding layer *j* of one of its parents, where the binary choice of the parent is realized randomly. As an example, let us consider the case represented in Fig. 4.4. At the left side of the picture the two parent-gratings are drawn in different colors. When analyzing the child-gratings at the right, it can be noticed that each of their layers has the color of the parent-grating which it copies. Very rarely, a mutation could be introduced at a random position in the layers of the child-gratings. In natural selection, a mutation introduces new genes in that population's genetic pool. For the case of Bragg gratings, this will introduce a layer with a random width at a random position in a child-grating. This should be seldom operated as it has rarely a positive result on the fitness function. Having obtained a new population of *N* child-gratings, the algorithm can now start all over again.

The decision to re-iterate the algorithm on the new generation of gratings is represented as the sixth step in Fig. 4.2. Passing from one generation to a new one will produce gratings with better fitness values, as the best gratings (those with highest fitness values) are favored at each step. After a certain number of iterations, the maximum value of the fitness function $max(f_i)$ corresponding to the best grating in that generation will converge to a constant value and it will not modify from a generation to the next. This is an indicator that the fittest grating was found and the program is stopped. Alternatively, the decision to stop the program and return the fittest grating obtained may be taken after a fixed number of iterations. Another fittest grating can be generated by starting again the algorithm with different initial conditions.

In the initial genetic algorithm of Skaar and Risvik [40] the genes were represented not by the layers of a grating, but by the segments of the grating in which the complex coupling coefficient q could be considered constant. This segmentation of a grating is linked with the approximation employed at the beginning of section 3.3.2 for the numerical analysis of non-uniform gratings. Other than the rare mutations applied on the layers of child-gratings, the authors also used a random generation of completely new gratings at every iteration of the algorithm.

4.2.2 Discrete Layer Peeling

The Discrete Layer Peeling (DLP) algorithm [41] is a method of grating synthesis first adapted by Feced *et al.* [49] from Digital Signal Processing (DSP) techniques of filter design [50]. Contrary to the Genetic Algorithm which can be programmed to generate any type of grating, the DLP may be employed only for the design of discrete gratings. If the layer widths in a grating are chosen so that the optical paths of radiation through each layer is constant along the length of the grating, then the Bragg grating becomes completely similar to a digital filter. This concept could be better understood by looking at Fig. 4.5. At the top of the figure, eight transitions in the refractive index mark the interfaces between different layers. Every layer has the same value a for the optical path length, which is the product between the width of a layer and its refractive index. This also means that the time required by a beam of light to travel across each layer has the same value for all the layers of the grating. If

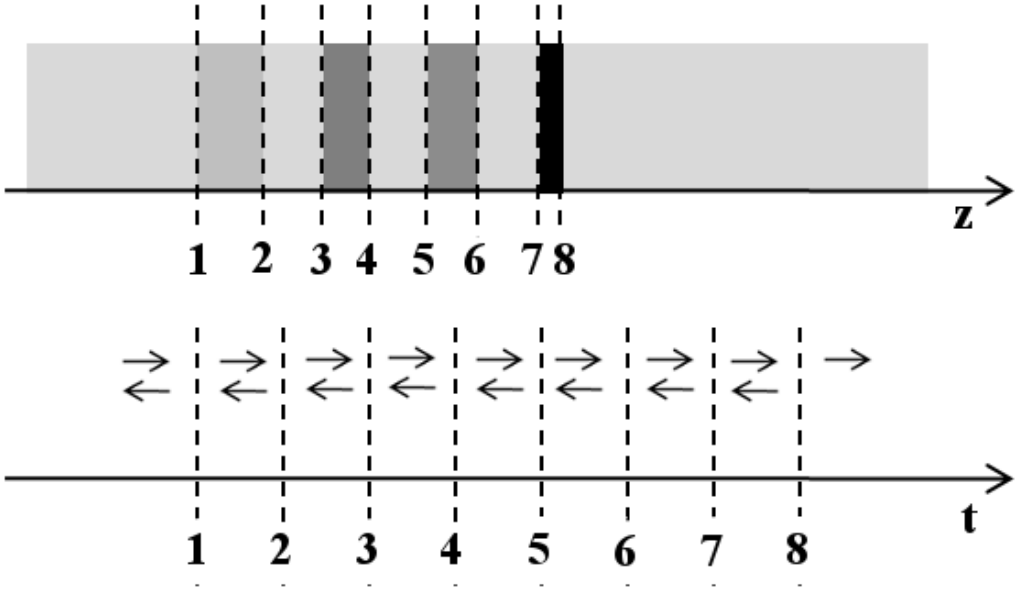

Fig. 4.5 Representation of the analogy between a digital filter and a Bragg grating for which all the layers have the same optical path length

a Dirac pulse of light is sent at the entry of the grating, then a detector placed on the same side will detect reflection pulses spaced by a temporal interval equal to $2a/c$. This discretization (or sampling) of any signal injected at the entry point of such a grating makes that grating similar to a digital filter whose coefficients are the reflectivities between the layers. This observation makes justifiable the utilization of a digital filter design method for the synthesis of a discrete grating.

The input information which is fed to the algorithm is a vector of the desired frequency response that our grating must have in order to widen the resonant modes of a cavity. It was established in the last chapter that this coincides with a reflection response having a high reflectivity and a negative *GTD*. An example of such a response is displayed in Fig. 4.6, in which the complex reflection response is unequivocally determined by the reflection amplitude and *GTD* - which is linked to the reflectivity phase by equation (3.13).

The algorithm will then apply an Inverse Fourier Transform to translate this ideal frequency response into the time domain. The time response determines [41] the physical structure of the grating, so that is why in this stage the feasibility of a grating is decided. This correlation between the time domain and the physical structure is easily explained: as the signal propagates through the grating the time response (in this case the reflected signal) changes accordingly. Inversely, knowing

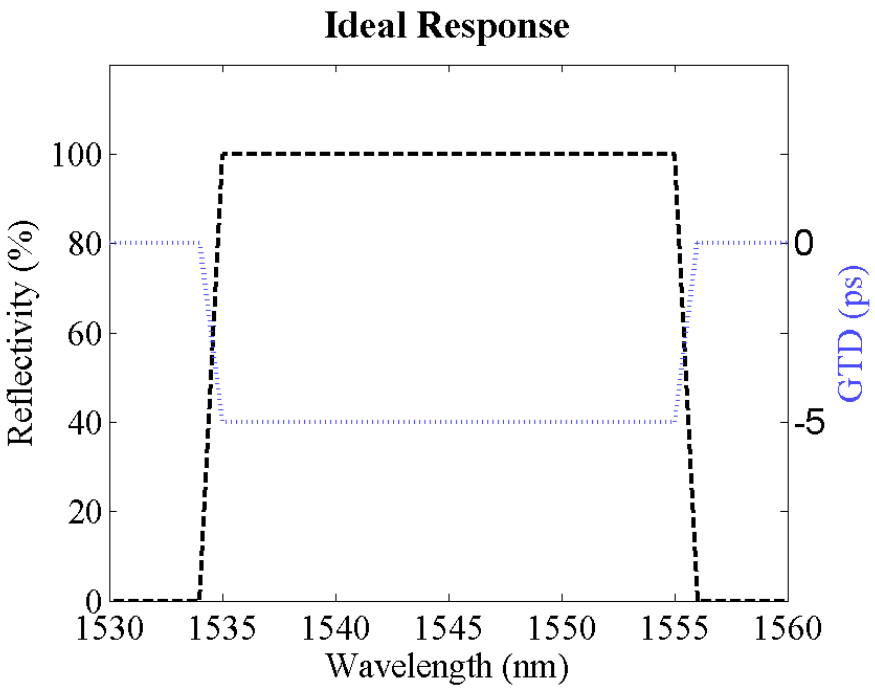

Fig. 4.6 Example of a type of ideal response used as input for the DLP algorithm. The black pointed line represents the desired reflectivity, while the blue pointed one is the desired GTD.

the time response of a grating would permit us to find its inner structure [33]. Not every imagined time response corresponds to a physical structure. That is why the Fourier transform of our desired frequency response will be called the ideal or the desired time response. At this stage it is not known how far from a physical real time response the ideal time response is. In order to become physically realizable, this response is passed through different mathematical functions (truncating, windowing and shifting). The number of physical layers of the grating is also decided at this stage. The realizable time response is then translated back into frequency domain by a Fourier Transform. Thus by starting with a desired frequency response it can be arrived, after a series of mathematical manipulations, to a realizable frequency response.

Not every desired response is possible, and the mathematical reason for this is that certain time responses are anti-causal and thus could not be obtained by the use of real physical structures. As already stated in the preceding paragraph, there is a mathematical method for making a frequency response realizable, which equates with transforming its time response from an anti-causal to a causal one. Sadly, the method can not be used directly to serve our purpose, as one of its steps will determine a change in the sign of the *GTD*. This is because after shifting the time

response, the phase derivative (thus the *GTD*) changes also. Feced's method is suitable when the phase of the frequency response is not important and the amplitude is the only one that counts. That is why the approach of this manuscript was different. It is based on a mathematical treatment known as zero-padding method [50] which is used by engineers in DSP. Its purpose is to detect if the *GTD* of the real structure created by the DLP algorithm (without the mathematical transformations which would modify the *GTD*) remains the same as the desired one. A short explanation of how precisely it does that follows next. To specify a desired frequency response in numerical form, a process of sampling and quantization must firstly be employed. Let Q be the number of points used for the sampling of the desired frequency response. When using an Inverse Discrete Fourier Transform (IDFT) the Q complex numbers in frequency domain will correspond to approximately $2Q$ real numbers in the time domain. By zero-padding this signal at the right with an equal number ($2Q$) of zeros and then translating the entire $4Q$ signal back to frequency domain, what it will be obtained is a quantity of $2Q$ complex numbers representing the same frequency response as the initial one, only now having twice the initial resolution. If the initial frequency response corresponds to a realizable (causal) filter, the process of zero-padding at the right will not change the form of the response, no matter how much the resolution is increased. On the contrary, if the desired frequency response corresponds to an anti-causal imaginary filter, the process of zero-padding at the right will greatly change the aspect of that frequency response, transforming also the *GTD* in the process.

4.3 Results

In this chapter the results of both synthesis methods for thin-film gratings will be presented. In the part reserved to the Genetic Algorithm a greater emphasis will be put on the integrated structures. The reason for this will be explained at the beginning of the next section, where a comparison between the performances of fiber and integrated generated gratings is presented. While the resulting gratings obtained by the genetic algorithm will not have perfect spectra, they could be nevertheless adapted for a continuum generation on a bandwidth of 8-15nm. Whereas the genetic algorithm strives with each new repetition to approach the perfect-spectrum grating

and in this process it generates intermediary optimum gratings, the Discrete Layer Peeling (DLP) method will only generate a grating if its desired spectrum is physically possible, otherwise the result may be totally unsatisfactory.

4.3.1 Genetic Algorithm

The random generation of gratings can be a powerful tool for grating synthesis even without the use of a genetic algorithm, if this method is applied in an efficient way. For example, a random population of $N=1000$ gratings could be created, and from within this population, the grating having the best characteristics can be directly chosen. In the case of the genetic algorithm, the random generation is only the first step of the method. For it to be efficient, the limits of the parameters' variation should be carefully chosen. As our attention was set on the type of random-width gratings presented in Fig. 4.1(a), then the parameter whose limits must be carefully set is the width w of the layers. Considering the working wavelength to be around $\lambda=1550nm$ and the grating's material to be InP, then it follows from equation (2.6) that the corresponding Bragg period is $\Lambda_B=240nm$. Each layer of a uniform Bragg grating set to work at this center wavelength would thus have a width of $w_B=\Lambda/2=120nm$, which we will call the Bragg width of a layer, from now on. One of the requirements for a successful synthesis method is obtaining a high reflectivity module (or amplitude). For this to happen, the interval of generated random widths should be chosen in such a way as to include also the calculated Bragg width w_B. In the other case, the farther away that interval is chosen, the smaller the maximum possible reflectivity will be. If w_{min} represents the minimum possible width of a randomly generated layer and w_{max} the maximum one, it then follows that $w_{min}< w_B <w_{max}$. As for the dimension $\Delta w=w_{max}-w_{min}$ of the random interval, having it too large would generate only small reflectivity gratings, even if the maximum theoretical reflectivity would be that of a uniform Bragg grating of period Λ_B. On the contrary, a small dimension of Δw around the Bragg width w_B would not offer enough variation to the population of random gratings. Keeping these aspects in mind, the random layer width was finally set within an interval of $[w_{min}, w_{max}]=[15,150]\text{nm}$ for InP and $[w_{min}, w_{max}]=[30,300]\text{nm}$ for a fiber grating.

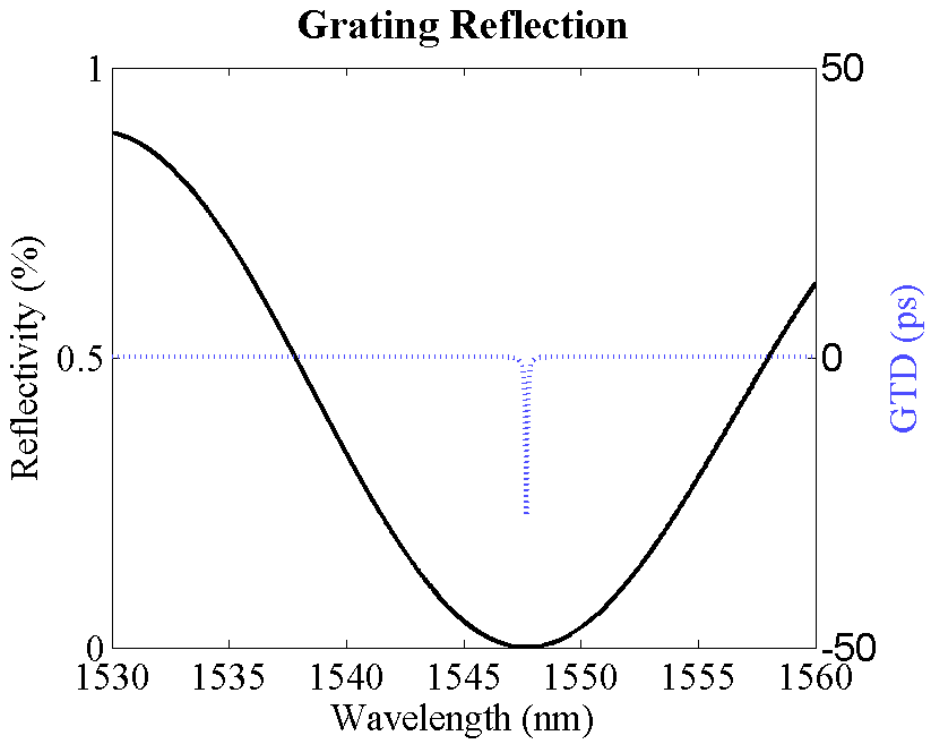

Fig. 4.7 Specter of a genetic grating obtained after 10 iterations by a genetic algorithm which searches for a steep negative GTD grating of 200 layers on InP. The reflectivity amplitude is shown in black, while the GTD in blue.

After establishing the limits for the grating parameters, next important step is deciding which fitness function to use. As our main objective was finding a grating with a negative GTD, we started with a fitness function favoring a high negative GTD. It was soon observed that each time we employed such a function, the regions of very high negative GTD corresponded only with regions of zero reflectivity. A typical example is shown in Fig. 4.7 which displays the specter of a 200-layer grating found by a genetic algorithm after ten iterations. The initial population used by the algorithm was *N=1000*. It is noticed that the high negative value of $GTD = -28ps$ corresponds to a region of zero reflectivity. In fact each time the algorithm searched for a high negative *GTD* grating, the returning spectrum had a corresponding region of null reflectivity. It thus became apparent that the two conditions (negative *GTD* and high reflectivity) are opposed. A fitness function which would try to conciliate both of the conditions was then searched. The final decision was set on the function already explained in equation (4.1) which weights every sampling point of negative *GTD* found in a certain bandwidth (let us say *1540-1550nm)* with its corresponding reflectivity. Every genetic grating presented next will have the fitness function of (4.1) at the core of its generating algorithm. It is obvious that the function (4.1) does

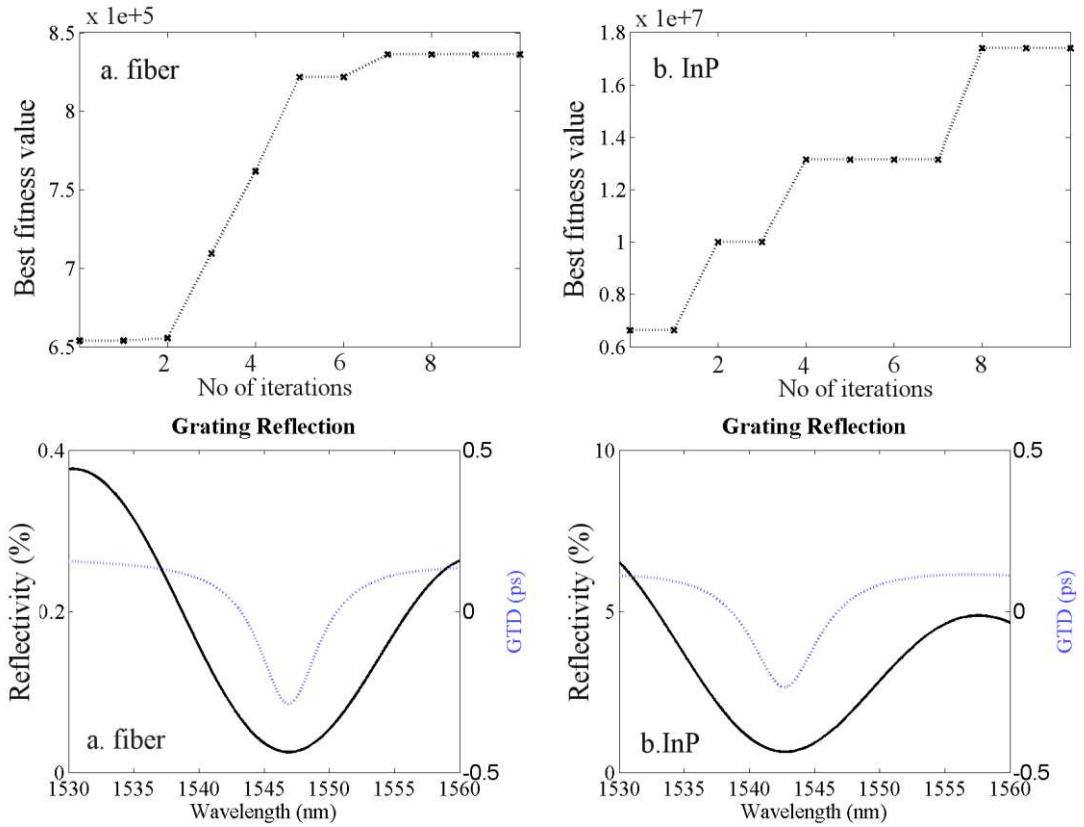

Fig. 4.8 Comparison between the efficiencies of the genetic algorithm for the case of two populations of (a) fiber and (b) InP gratings. Both populations are comprised of gratings of *M=200layers*. To the top, the evolution of the best fitness value in function of the number of new generations created by the algorithm. To the bottom, the best spectra obtained in the 10th new generation.

not take into account the request of having a *constant* negative *GTD* (the necessary condition for the large-band continuum). Increasing the strictness of the conditions on the side of the *GTD* would only diminish the reflectivity. The value returned by the fitness function (4.1) should be expressed in picoseconds, but in the following figures, the fitness-values have been normalized and are thus expressed in arbitrary units. It is not the absolute value of the fitness function that is important, but its evolution through successive generations created by the genetic algorithm, or its variation when changing the initial parameters of the method.

Another point to establish before proceeding further is the reason behind the choice of the InP as the preferred grating material. Figure 4.8 shows a comparison of the evolution of the best fitness value in two populations of gratings having the same general characteristics, except for their material and thus their coupling coefficients. A maximum achievable value for the coupling coefficient has been used in both cases, this corresponding to a value of $k=100cm^{-1}$ for the fiber case and to a value of

$k=1000cm^{-1}$ for the InP structures. The best fitness value is the maximum value returned by the fitness function, when applied to each individual in a specific population. Comparing the two plots at the top, it is obvious that the initial (when the number of iterations equals zero) best fitness value in the InP population is ten times higher than the best fitness value in the initial fiber population. Comparing then the evolution of this value in ten consecutive generations of genetic gratings it becomes also obvious that much better performances are obtained by applying the algorithm in the InP case. Finally, at the bottom of the figure, the resulting best spectra in the 10^{th} generation are displayed side by side for the two cases. It is clear that what is deciding the high performances obtained by the InP structures is their much higher reflection amplitude resulting from their much higher coupling coefficient. Surprisingly, the values for the negative *GTD* are very similar in the two cases. The slight advantage obtained by the fiber grating is explained by its lower coupling coefficient. It was already shown in Fig. 3.7 of the previous chapter that there is an inverse correlation between the coupling coefficient and the positive values of the *GTD*. But regarding our choice of InP gratings, the much greater rise in the reflectivity makes the little loss in the *GTD* unimportant. Not only the performances of InP gratings regarding their fitness values are better comparing to the fiber ones, but there is also the fact that the real InP structures come much closer to the discrete thin layer model used in the simulations of this manuscript.

Now that a decision has been made on the best material and fitness function to be used in the simulations, and also on the width-span for each layer, the question now goes on the number of layers our synthesized InP grating should have. As it will be soon acknowledged, this is a more difficult question. A direct approach to this question is presented in Fig. 4.9. In this figure, the best fitness value in a population of $N=1000$ random gratings is calculated before (black line), and after a genetic algorithm has been applied to that population (grey line). For the two cases, the variation of the best fitness value is plotted in function of the number of layers in the gratings of each population. The amelioration of the maximum fitness value after applying the genetic algorithm may not seem impressive at first, but a more detailed look will show us otherwise. Let us take the example of the 200-layer InP gratings. Before applying the genetic algorithm (G.A.) the maximum fitness value obtained in a population of $N=1000$ gratings was $f_{max}=0.7\cdot10^{7}$. At the 10^{th} new generation

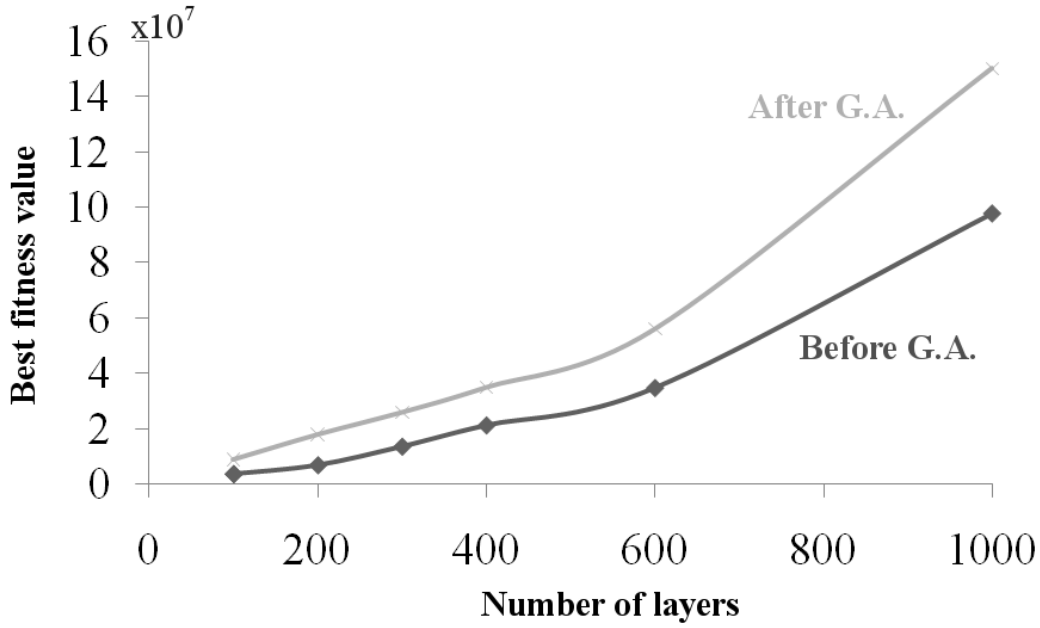

Fig. 4.9 The variation of the fitness-value of the fittest grating in a population of *N = 1000* InP gratings in function of the number of layers of the gratings in that population. The black line is for the initial random population, while the grey line corresponds to the 10th generation created by a genetic algorithm (G.A.).

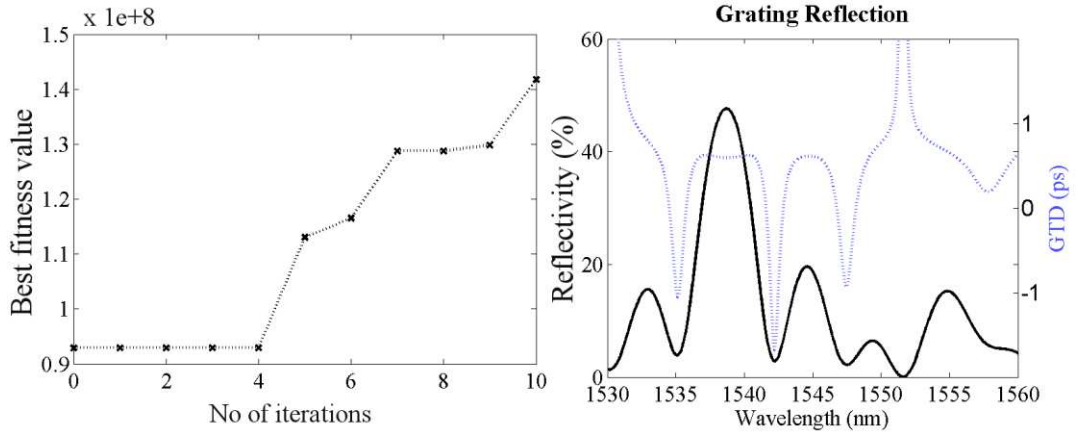

Fig. 4.10 Results after running the genetic algorithm on a population of *N=1000* gratings of *M=1000* layers each: to the left, the evolution of the best fitness value in function of the number of new generations created by the algorithm; to the right, the best spectrum obtained after 10 iterations of the genetic algorithm. In the plot at right, the reflection amplitude is represented in black, while the GTD in function of wavelength is displayed in blue.

created by the genetic algorithm the maximum fitness value becomes $f_{max}=1.8\cdot10^7$. The entire evolution of the fitness value from the first to the last generation is shown in Fig. 4.8(b). The change in the maximum fitness value after applying the genetic algorithm was compared to the maximum fitness value obtained after increasing the initial random population of gratings. The purpose was to see how many random

gratings must be generated (having the same number *M=200* of layers) until we randomly find a grating having the same fitness value as that generated by the genetic algorithm. Well, the maximum value of the fitness value found in a population of *N=30.000* random gratings of *M=200* layers was $f_{max}=1.35\cdot10^{7}$, still way below the value of that grating generated by the genetic algorithm which started from a population of only *N=1000* gratings. At that point of *N=30.000* the random generation was stopped as it was clear it would not easily match the level of the genetic generation.

At the other end of Fig. 4.9 there is the case of the long gratings of *M=1000* layers. The maximum fitness value obtained in a random population of such N=1000 gratings is very high, $f_{max}=9.3\cdot10^{7}$, much higher than the score obtained for the case of *M=200* layers. After applying the genetic algorithm on this initial population, and thus moving from the black to the grey line in Fig. 4.9, the maximum fitness value reaches a whooping $f_{max}=15\cdot10^{7}$. But there is a price to pay for this progress in the fitness value. Figure 4.10 shows the evolution of the best fitness value after 10 iterations of the algorithm and also the best spectrum obtained at the 10^{th} new generation. Comparing this spectrum to the one of Fig. 4.8(b), it can be noticed that when increasing the values of the reflectivity corresponding to a region of negative *GTD*, there is a simultaneous much higher increase in the reflectivity corresponding to a positive *GTD* in the surrounding regions. This makes very difficult the selection of our region of interest when building a resonant cavity with such a reflector. The resonant modes will be placed at the wavelengths corresponding to positive *GTD*s while the regions of interest, having negative GTDs will find themselves canceled. On the contrary, looking at the spectrum of Fig. 4.8(b), the regions of positive *GTD* and higher reflectivity are far enough from our region of negative GTD to be able to cancel them out by using some filters or the right gain medium. That is why choosing the number of layers for the grating is such a delicate problem. From one point of view, high negative *GTD*s are needed to enlarge resonant modes of long Fabry-Perot cavities, cf. equation (3.20). On the other hand, when this is achievable, the regions of negative *GTD*s are surrounded by regions of high reflectivity positive *GTD*, which can not be easily suppressed. Our preference was thus for the gratings which were shorter than *M=400* layers. Even though they are characterized by smaller

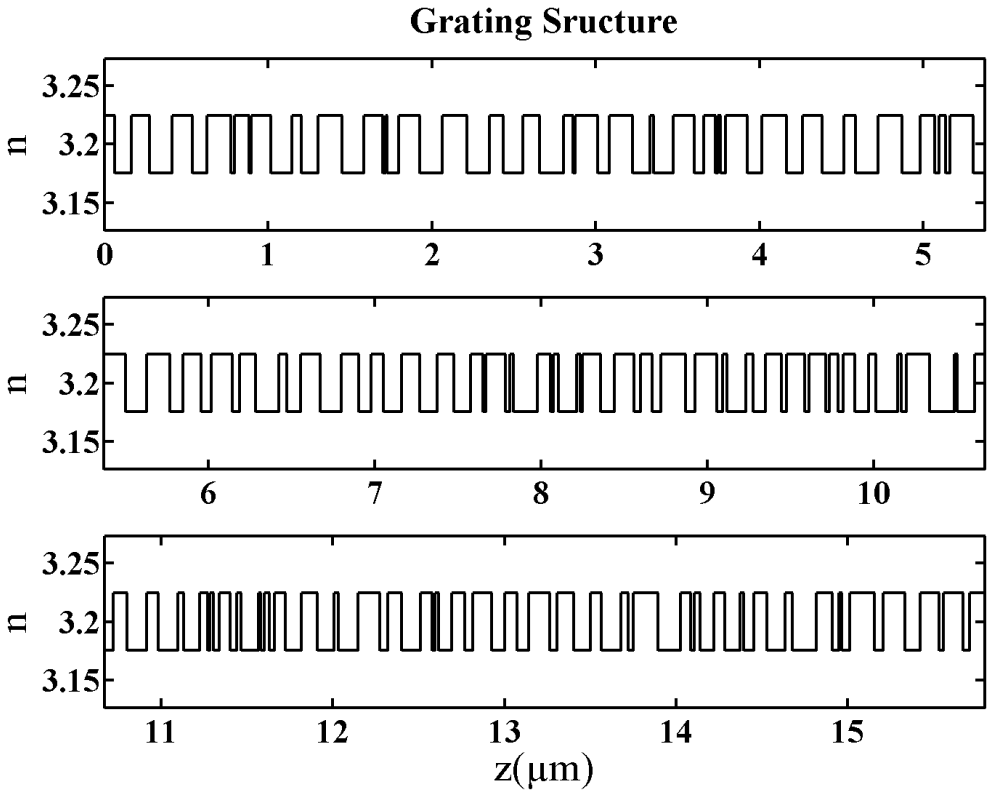

Fig. 4.11 Refractive index variation of the 200-layer grating synthesized by the genetic algorithm and whose spectrum was plotted in Fig. 4.8(b)

reflectivities and by smaller negative GTDs, their spectrum shapes can be more easily adapted for continuum emission.

Figure 4.11 shows the refractive index variation of the best fitted grating of $M=200$ layers, synthesized after ten iterations of a genetic algorithm on a population of $N=1000$ structures. Its spectrum was already presented in Fig. 4.8(b). Another way of presenting the reflectivity spectrum of this grating is by replacing the *GTD* directly with the phase difference after reflection. This representation is used in Fig. 4.12(a), where the blue line is the phase difference of the reflected radiation of wavelength λ compared to the radiation of wavelength $\lambda_0=1530nm$. For comparison Fig. 4.13(a) shows an analog representation of the reflection spectrum, but for a uniform Bragg grating of 100 periods (200 layers) having the same coupling coefficient $k=1000cm^{-1}$. Whereas the phase of the Bragg reflector is uniformly increasing with the wavelength, the phase of the genetic grating has an interval of $\Delta\lambda=8nm$ centered at $1543nm$ for which the phase is descendant. This interval corresponds to the region of negative *GTD* in Fig. 4.8(b).

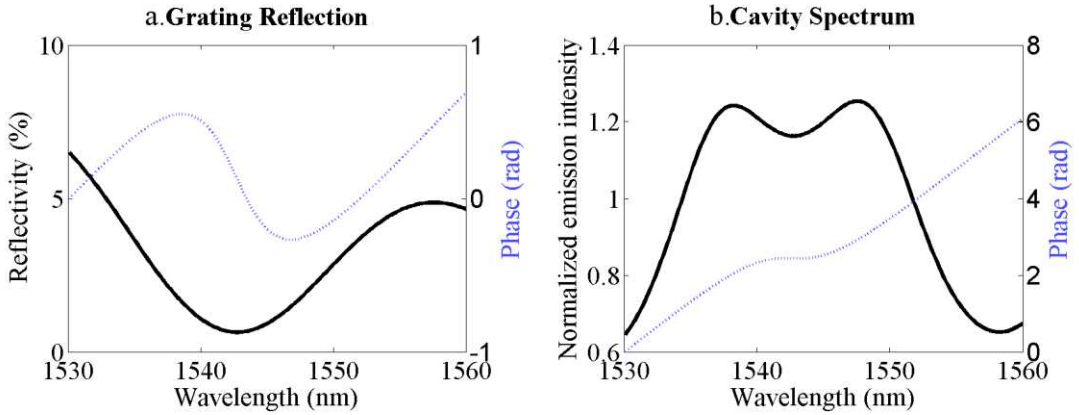

Fig. 4.12 Reflection spectrum of a 200-layer genetic grating and the resonant emission of a continuum cavity formed with that grating as a mirror.

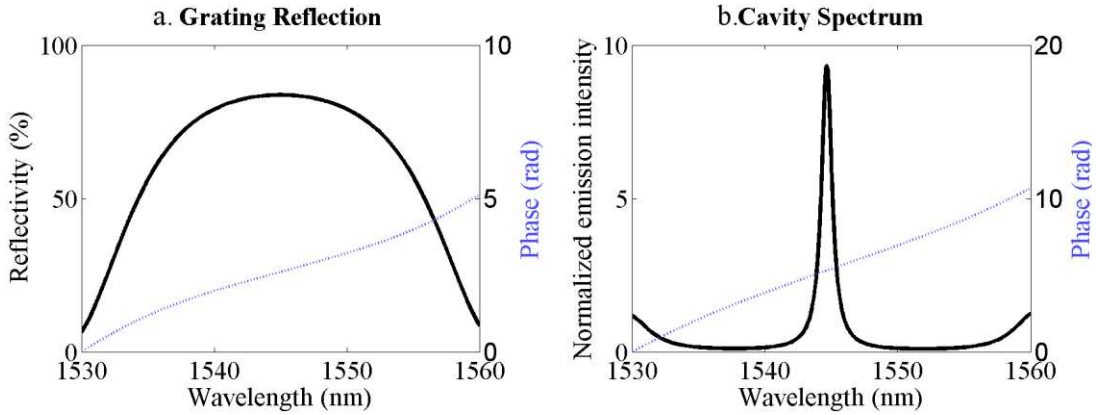

Fig. 4.13 Reflection spectrum of a 200-layer (100-period) uniform InP grating and the resonant emission of a resonant cavity formed with that grating as a mirror. The coupling coefficient of the grating is $k=1000cm^{-1}$.

In the examples discussed above, ten iterations of the algorithm were considered enough, as after this number of repetitions all new generated gratings were usually having very similar layer-characteristics. Continuing their combination would not have yielded very different fitness functions.

The grating shown in Fig. 4.11 is then used as a mirror in a resonant cavity. The feed-back is assured on the other side of the cavity by a high reflectivity metallic mirror of reflection coefficient equal to $R=0.9$. For a specific length of the resonant cavity (when the cavity's phase variation with λ is canceled by the grating's phase variation) the entire structure has a normalized emission spectrum as that shown in Fig. 4.12(b). The specific or continuum length of the cavity is calculated from equation (3.20) and it depends on the highest negative value of the *GTD*. Replacing thus in equation (3.20) a value of $GTD=-0,235ps$ for the group time delay, then the calculated length of the resonant cavity is $L_0 \approx 11\mu m$. This is the length of the

cavity used for the simulation in Fig. 4.12(b). Keeping the same cavity length and replacing the synthesized grating by the uniform Bragg (UB) grating of Fig. 4.13(a), the spectrum of the cavity becomes as in Fig. 4.13b. What it can also be noticed in Fig. 4.12b is the almost complete cessation of the phase variation between 1539nm and 1547nm, the interval in which the negative *GTD* of the grating cancels the positive *GTD* of the rest of the cavity. In other words, the round-trip phase of the cavity keeps constant on this 8nm bandwidth because the natural increase of the round trip phase with λ is balanced by a similar decrease of the grating reflection phase. It can also be observed that the saddle of constant round-trip phase (1539-1547nm) is linked to two nearby reflectivity peaks of increasing phase (1536-1539nm and 1547-1550nm) making the entire emission bandwidth to reach a span of almost *15nm*.

The two normalized emission spectra which were presented in Fig. 4.12(b) and Fig. 4.13(b) were simulated under threshold considering an active medium placed inside the cavity. The active medium has a uniform spontaneous emission over all wavelengths. The interference caused by the consecutive round trips of this emission through the cavity generates the spectra of Fig. 4.12(b) and Fig. 4.13(b). The gain coefficient α of the medium is considered equal to zero. Different forms of the gain coefficient can be imagined so that the small valley in Fig. 4.12(b) formed in the negative *GTD* region would be leveled out with the two surrounding peaks. For more information on the method used to generate the two normalized spectra, the reader can refer to the paper of Soda and Imai [51].

The reason why one could not design a grating characterized by a negative GTD in a spectral region of high reflectivity may be found only after using another method of grating synthesis, called Discrete Layer Peeling.

4.3.2 Discrete Layer Peeling

As explained in section 4.2.2, the first step of this method is to feed the algorithm with a desired frequency response. In this particular case, the desired frequency response consists of having a maximum of amplitude simultaneously with a negative *GTD*, as shown in Fig. 4.6. As explained in the introductory part to the Discrete

Layer Peeling (DLP) method, the frequency domain response is entered as a set of Q complex numbers, having both amplitude and phase, which are sampled from that response for a set Q of wavelengths. After transforming this frequency vector into the time domain, a set of $2Q$ real numbers is obtained, which contains enough information for the construction of a grating structure by DLP. At this point though, there is the possibility that the reflectivity spectrum returned by the synthesized structure may coincide with the initial desired spectrum only in the sampling points, and that between these points its behavior may be completely erratic. To check whether this is the case, the zero padding method is used, increasing the resolution (as explained in section 4.2.2) until a stable figure is obtained.

Basically, the algorithm was fed with different sampled vectors of ideal responses as the one in Fig. 4.6. Different values for the desired GTD_d were used, whereas the reflectivity was always kept to a maximum value close to 100%. The filter structure returned by the algorithm was then analyzed again in the spectral domain. When analyzing the resulting spectrum only for the wavelengths corresponding to the sampling points of the initial response vector, the values for the resulting GTD_r and reflectivity seem always to exactly correspond with the ideal ones. But when increasing the resolution a few hundred of times, there can be seen that the resulting response is not always equal to the one desired by us. And this difference, if it exists, can dramatically change the value of the real GTD_r of the structure. For example if the phase for the sampling wavelength λ_j has a phase value of φ and in the next point λ_{j+1} ($\lambda_{j+1} > \lambda_j$) will reach a value of $\varphi - \delta\varphi$ the GTD_r of the real structure will be calculated as negative. But then again, if after increasing the resolution it is realized that between the two points there existed a phase shift of 2π so that in fact the phase

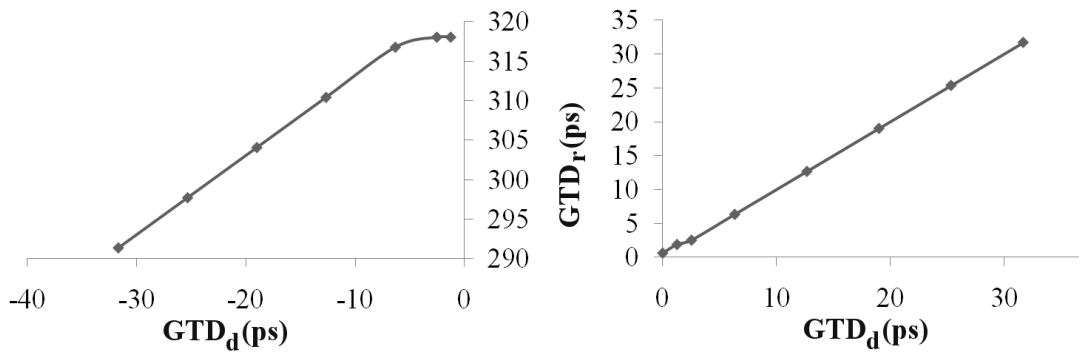

Fig. 4.14 The group time delay of the synthesized structure (GTD_r) created by a DLP algorithm, when it is fed with different ideal responses having different desired GTD (GTD_d).

in the point λ_{j+1} is equal to $\varphi + 2\pi - \delta\varphi$ then the real GTD_r will be in fact positive.

In Fig. 4.14 the resulting gratings' *GTD* (called GTD_r) are plotted in function of the values of the desired *GTD* (called GTD_d) which were used as entry data for the algorithm. The two plots correspond to the negative, respectively positive values of the desired GTD_d. As it can be seen on the plot to the right, every desired positive GTD_d response translates itself into a realizable structure having an identical value of the group time delay $(GTD_r = GTD_d)$. In the same time a maximum value for the reflectivity was obtained. On the other hand, each time the DLP algorithm must design a high reflectivity Bragg grating having a negative GTD in the reflection bandwidth (left plot of Fig. 4.14), the resulting grating will have in fact a very high positive GTD (as revealed after increasing the resolution of the resulting spectrum).

As the success of this algorithm depends on the conformity of the desired spectrum to the causality principle, it follows that filter responses having negative *GTD*s and maximal reflection amplitudes can not be produced by real linear structures. This also confirms our supposition that the structures returned by the genetic algorithm are among the best which can be realized by means of linear reflectors, even if the regions of negative GTD do not appear simultaneously with peaks of the reflectivity.

Chapter 5

Measurements

This chapter will succinctly present the experimental measurements on a series of resonant cavities formed with chirped gratings. The only chirped gratings that could be employed were the linearly chirped gratings presented in Chapter 3. Nevertheless, we have been able to find some interesting applications for this simple type of Bragg gratings. The hybrid cavities were used as tunable lasers and large band amplifiers, whereas the integrated cavities were used in experiments of injection locking.

5.1 Hybrid cavity

The hybrid cavity was already described in Section 3.2.1 before presenting the simulations on resonant cavities formed with LCGs. The simulations of Chapter 3 already shown that there is no way of producing a continuum emission spectrum using a LCG in conjunction with a resonant cavity, contrary to the initial supposition of the Continuum project presented in Section 2.2. It was later found in Chapter 4 that only some type of random-layer structure, generated by a genetic algorithm, was able to enlarge the emission spectrum of a Fabry-Perot cavity. Despite this later finding, it was not possible to obtain a real prototype of those synthesized gratings in due time, and thus the experimental part of the project revolved around finding new applications for the already delivered linearly chirped gratings.

Even though it was clearly shown in the simulations that a continuum can not be obtained by LCGs, some experiments were realized in this purpose by a fellow colleague of SUPELEC, Xunqi Wu, who presented this study in his PhD thesis [19]. It is not our intention to concentrate the discussion on this topic, even though some open points remain as to whether his measured spectra were single-mode or multi-mode. Without an experimental probing into the nature of those spectra obtained by Wu [19] from resonant cavities formed with LCGs, we will trust the TMM simulations and consider them multi-mode.

5.1.1 Description

Section 3.2.1 presented a hybrid type of cavity formed between a metallic mirror and a LCG. That type was the most explored one throughout the simulations of this manuscript, being used in both Chapters 3 and 4. In this experimental section a

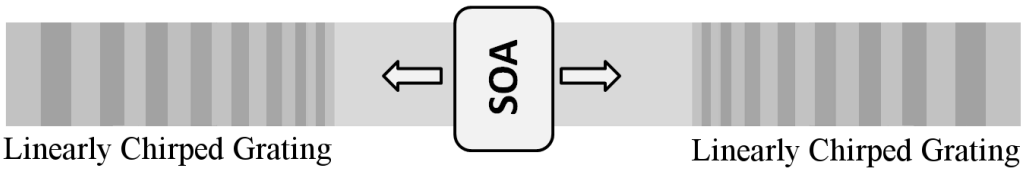

Fig. 5.1 The hybrid cavity model used in the experimental measurements. The metallic mirror which formerly bordered one side of the cavity was replaced by a second identical LCG.

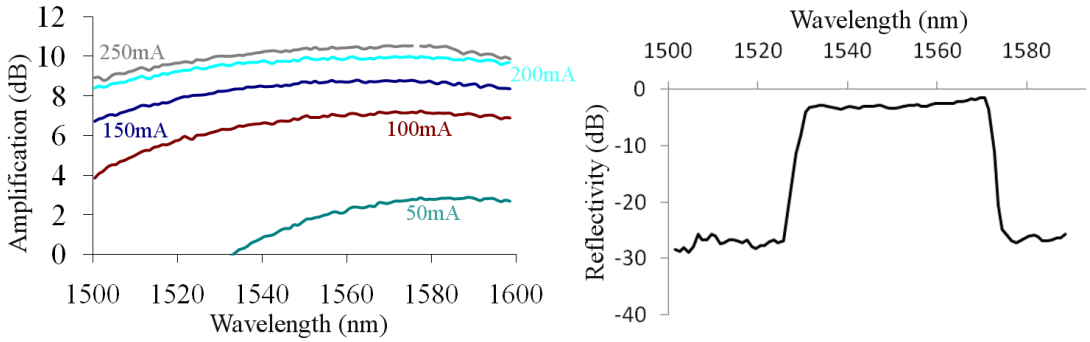

Fig. 5.2 Plots showing typical spectral characteristics of SOA and LCG. To the left, the amplification of the SOA in function of wavelength is plotted for different source currents and for very low levels of signal power. To the right, the reflectivity amplitude of the LCG is measured in function of the wavelength. The LCG is a fiber grating of chirp *C=100nm/cm*, coupling coefficient $k=80cm^{-1}$ and *R=50%*.

somehow different model of cavity will be used. As shown in Fig. 5.1, the metallic mirror which bordered the resonant cavity of Fig. 3.2 is now substituted by a second LCG, identical to the one used at the right side of the cavity. Some typical spectral characteristics for the SOA and LCGs are shown separately in Fig. 5.2. In the plot to the right, the reflection bandwidth of the LCGs is located between 1530-*1570nm*. The Reflectivity peaks at around *-3dB*, or at around *50%*. In the plot to the left, the gain of a SOA is plotted for different source currents. It can be noticed that for high currents the SOA gain keeps almost constant in the reflection bandwidth of the gratings. Also it can be noticed that at around 200mA the SOA reaches gain saturation.

The configuration presented in Fig. 5.1 was among the configurations considered capable of continuum generation at the beginning of the thesis. The theoretical approximations which were used for the case of a cavity formed between a metallic mirror and a LCG were presented in section 2.2.3. In that section, equation (2.8) linked the length of the supposed continuum cavity L_0 to the chirp of the grating C_Λ. The same equation can be adapted for the case of the cavity of Fig. 5.1. Considering L_0 the distance between the two LCGs and noting with C_Λ the chirp of both LCGs, equation (2.8) becomes:

$$L_0 = \frac{\lambda_0}{n_0 C_\Lambda}. \tag{5.1}$$

In the experiments of Wu [19], different cavity lengths have been used, including one equal to the value calculated in (5.1). The measured spectra were quasi-identical for

all cases, showing no trace of a magical cavity length for which the spectrum would become suddenly enlarged. A continuum effect may still have been produced, but in this case, it was hidden by the lack of resolution of the measuring equipment.

Replacing afterwards the two LCGs with different ones having different reflectivities and chirps, the same independence of the spectra to the cavity length was noticed. This behavior confirms that the initial continuum approximation explained in section 2.2.3 is not verifiable experimentally.

5.1.2 Tunable Laser

This section will describe an original application of resonant cavities built with LCGs, which may become the object of a separate patent application. Starting with

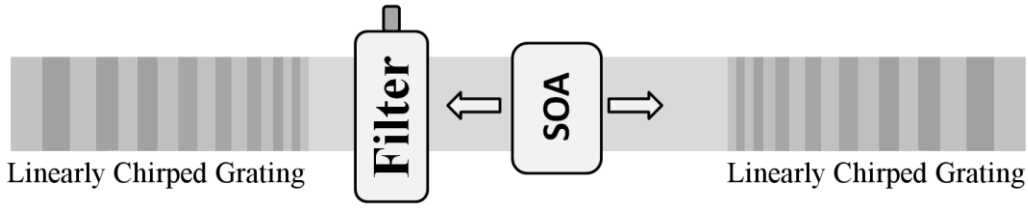

Fig. 5.3 Schematic of a tunable laser formed between two LCG. Inside the cavity a filter is used to manually set up the desired wavelength.

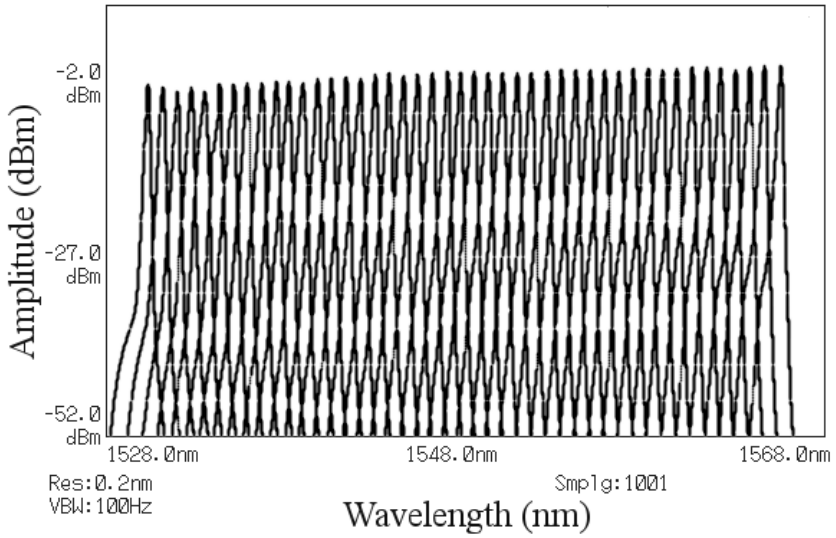

Fig. 5.4 Superposed emission spectra obtained by manually adjusting the filter of Fig. 5.3 for different wavelengths on the ITU grid

the tunable laser described in section 2.2.2 which resides at the origin of the Continuum project, we tried to imagine an alternative way of shifting the emission spectra of a resonant cavity. The structure of Fig. 5.3 was thus created. The filter, having a 3dB-bandwidth of *1nm*, has the role of manually setting the radiation wavelength to any desired value contained in both the reflection bandwidth of the grating and the filter's frequency domain. The reflection bandwidth was shown in Fig. 5.2 as being the interval *1530-1570nm*, whereas the filter's variation domain consisted of the interval *1525-1565nm*. The intersection of the two will then consist of the spectral domain of *1530-1565nm*. By manually turning the adjusting knob of the filter, the spectrum will be centered on any wavelength in this later interval. A superposition of such spectra obtained after successive adjustments of the filter's knob is shown in Fig. 5.4. The frequency span between two consecutive peaks of Fig. 5.4 is *50GHz*. Each peak was specifically chosen to match the ITU-comb frequencies used in C-band WDM communications. When the filter is set outside the reflection bandwidth of the gratings (in the interval 1525-1530nm) there is no laser radiation present. Only the LCGs assure the feedback necessary for a laser emission. Each separate plot of Fig. 5.4 was rendered by an optical analyzer after sampling 1000 points over the entire 40-nm observation window.

A zoom onto the shape of a single peak from Fig. 5.4 is then represented in black in Fig. 5.5. Using only the optical analyzer it would be impossible to decide whether the

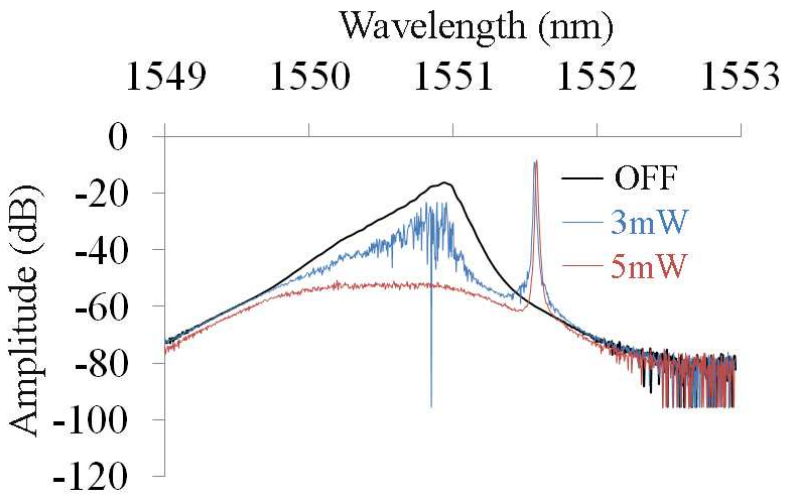

Fig. 5.5 Superposed emission spectra of the cavity in Fig. 5.3 when an external laser is injected inside the cavity: a. no external power (black); b. 3mW external power (blue); c. 5mW external power (red).

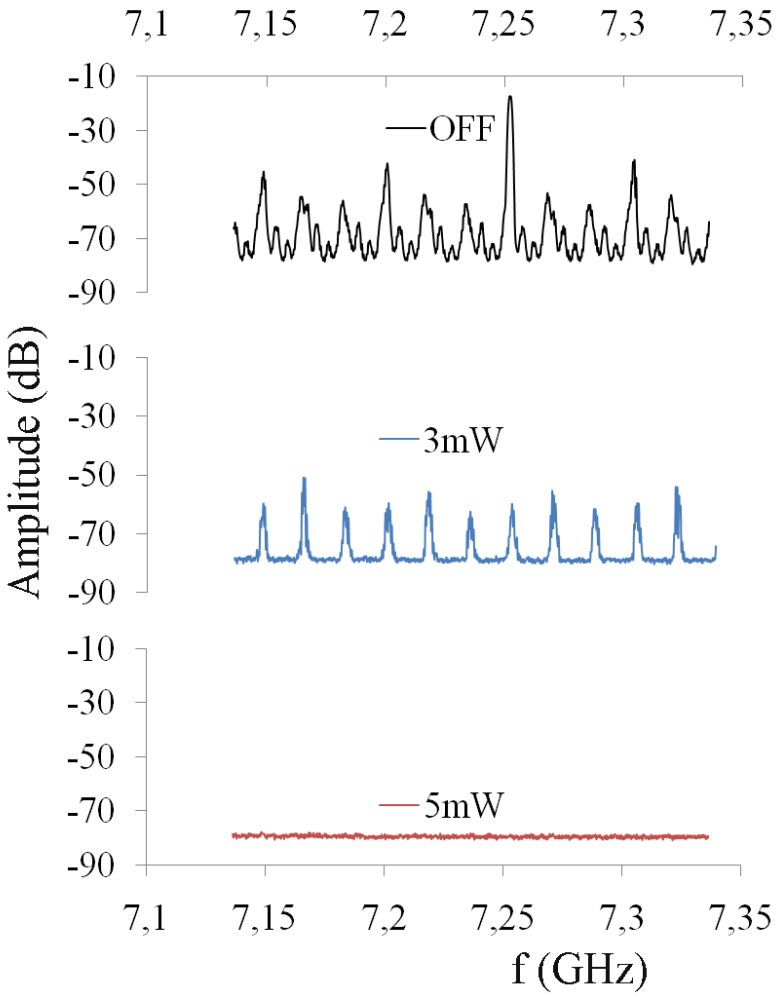

Fig. 5.6 Electrical spectra plotted by a fast photodiode receiving as input the optical radiation exiting the cavity of Fig. 5.3. An external laser is injected into the cavity from the other side, having: a. no external power (black); b. 3mW external power (blue); c. 5mW external power (red).

emission is single-mode or multi-mode. An external (also called master) laser will be injected into the cavity from the left and it will thus be used to dissect the resonant cavity's emission (which can also be called slave emission). In addition to the external laser, a fast photodiode and an electrical analyzer were employed on the other side of the cavity. After receiving the radiation going out of the cavity to the right, the photodiode would transmit the resulting electrical pulse to the electrical analyzer for plotting.

The resulting electrical spectra are displayed in Fig. 5.6. For each of the electrical spectra, the corresponding optical spectrum is also displayed in Fig. 5.5. In the first situation presented in the two figures the external (master) laser is turned off. The

optical spectrum of Fig. 5.5 seems to be continuous, while the electrical spectrum of Fig. 5.6 is periodical. The electrical spectrum should represent the Fourier transform of any signal which modulates the slave laser, but because in the present case there is no external modulation of the cavity laser, there still remains the question of the origins of the periodical spectrum in Fig. 5.6.

The explanation for the electrical pattern could be found only if the optical spectrum is supposed multi-mode. In this case, the free spectral range $\Delta\lambda$ (the distance between two consecutive modes) of the cavity is calculated as:

$$\Delta\lambda = \frac{\lambda_0^2}{2n L_0}. \tag{5.2}$$

Passing the quantity of (5.2) in frequency domain, the free spectral range becomes:

$$\Delta f = \frac{c}{2n L_0}. \tag{5.3}$$

In equation (5.3) Δf is the free spectral range expressed in frequency domain as a function of the length of the cavity L_0. Replacing a value of $L_0 \approx 5m$ in equation (5.3) the calculated value for the free spectral range becomes $\Delta f \approx 20MHz$, coinciding with the period value noticed in Fig. 5.6. This means that the temporal variation in the amplitude of the radiation detected by the photodiode has its source in "the beating" between the different modes of the cavity.

In the second case, represented in color blue in both Fig. 5.5 and 5.6, the external laser having a power of 3mW and a wavelength of $\lambda = 1551.6nm$ is injected into the cavity very close to the cavity's central wavelength of $\lambda = 1550.9nm$. A maximum spectral detuning of *1nm* between the cavity laser and the external laser is necessary in order for the external radiation to pass the cavity-filter. In this situation, the optical spectrum of the cavity separates itself clearly in multiple modes. On the other hand, the amplitude of the electrical pattern reduces proportionally to the injected power.

A complete disappearance of the electrical pattern is noticed for an injected external power of *5mW*, as displayed at the bottom of Fig. 5.6. Correspondingly, looking at the red plot of Fig. 5.5, a complete disappearance of the optical cavity spectrum is also recorded. The only peak observed in this situation is the one corresponding to the external laser. What happens inside the cavity is that the entire electrical energy

represented by electron-hole pairs will be used to amplify the external laser only. It will rest no more energy into the active medium for the generation of its own stimulated radiation. Owing to this effect, the resonant cavity could be used as an amplifier for an external signal injected into the cavity. The amplification will not be due to an injection locking effect, as it will not depend on the polarization of the injected signal and it will span a large bandwidth. This different application will be the subject of the next section.

5.1.3 Amplifier

It was seen in the preceding section that when a high power radiation is injected into the cavity of Fig. 5.4 very close to the bandwidth of that cavity's proper laser emission, all energy will be used for the amplification of the external radiation, while the cavity's own laser emission will be stopped. The presence of a filter as the one in Fig. 5.3 will make the operation of the amplifier more difficult, because the filter's wavelength should always operate on the wavelength of the external laser. In this section therefore the simple schematic of Fig. 5.1 will be preferred. The amplifier will thus consist of a SOA placed between two LCGs of 50% reflectivity. An external laser of different amplitudes and wavelengths will be injected into the cavity of Fig. 5.1. On the other side of the cavity, the peak signal will be measured with a spectral analyzer. In Fig. 5.7 (a) a 0.5mW external laser is first used. The red dashed line indicates the level measured by the analyzer when no resonant cavity is present. The resonant cavity of Fig. 5.1 is then interposed between the external tunable laser

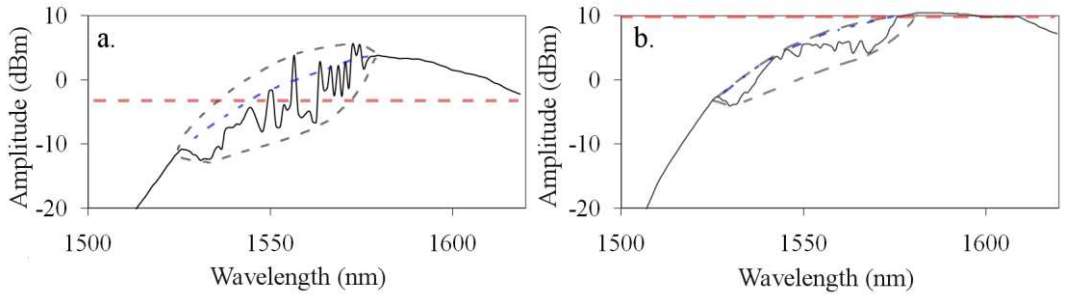

Fig. 5.7 Plots showing amplitude of the external laser in function of wavelength, after passing through the resonant amplifier of Fig. 5.1. Two different levels (marked in a red dashed line) of the external laser have been used as inputs: a. 0.5mW; b.10mW.

and the analyzer. The level of signal now detected by the analyzer is marked with a solid black line. When the tunable laser emits out of the Bragg gratings bandwidth (outside of the 1530-1570nm interval) the external radiation will pass through the SOA only once. It should be noted that the type of SOA employed for the plots of Fig. 5.7 differs from the one in Fig. 5.2. In Fig. 5.7 the dependence of the gain to the wavelength is very pronounced.

The interesting region is represented by the Bragg bandwidth, comprised between *1530nm* and *1570nm*, in which the external laser passes through the SOA multiple times before exiting the cavity. In this interval, the amplitude measured by the analyzer seems to vary greatly in time. This variation in time is recorded by the analyzer as a variation with the wavelength λ, as the amplitude corresponding to each wavelength is recorded during a couple of seconds before the external laser emits on the next wavelength. In fact, when the external laser is left to emit on a chosen wavelength long enough, the amplitude of the signal recorded by the analyzer will randomly oscillate between the two envelopes plotted in dashed black line in Fig. 5.7. Between the two envelopes, the middle dashed blue line shows the amplitude of the signal if the Bragg gratings were not present at all. It is the amplitude of the signal after passing through the SOA alone.

The cause for the temporal instability observed in the Bragg bandwidth is not well understood, but it may be linked to mode-competition of the cavity laser. As the signal is not strong enough to absorb the entire energy of the electron-hole pairs in the cavity, there are moments when some of this energy will serve to amplify the spontaneous emission of the SOA reflected back into the cavity by the Bragg gratings.

Oppositely, when increasing the power of the external laser to 10mW as in Fig. 5.7 (b) the level of radiation measured at the output of the cavity will not increase with the same quantity comparing to the case in Fig. 5.7 (a). This is because of reaching the saturation of gain offered by the SOA. In this situation, there will be of no benefit to use such a resonant cavity for the amplification of an external signal, as the amplitude at the output will be lower than the amplitude at the input side of that cavity (as the black line is under the red one for almost all wavelengths). At the same time with a reduction in the gain for all the wavelengths, there is also a reduction in

the instability seen in the reflection bandwidth of the Bragg gratings. Looking at the interval between *1530nm* and *1570nm*, a lowering of the superior instability envelope is noticed. This is due to the fact that increased levels of the external laser will absorb all the energy of electron-hole pairs. The level of spontaneous emission inside the cavity will simultaneously decrease, which will in turn translate into greater stability.

To conclude this section, a resonant cavity built with LCGs can greatly amplify an external signal and act as an amplifier only for low levels of injected power, under the level required for the SOA saturation. In the spectral region corresponding to the Bragg reflection of the gratings, the level of amplification can become 5dB greater than the amplification recorded by the SOA alone. On the other hand, spontaneous emission reflected back into the cavity by the Bragg gratings will be the source of a great level of amplification instability. The only way to counteract this effect is by increasing the level of the external radiation until all the electrical carriers inside the cavity are saturated. Sadly, this will also decrease the amplification performances of the resonant amplifier to the point that it would render its use futile.

5.2 Integrated cavity

The integrated type of cavity was described in section 2.2.3. As the integrated cavity was not directly used in our experiments, this small section will only try to reinterpret an experiment described in the related work of Xunqi Wu [19] regarding InP cavities. But before going further, it is worth remembering here that this type of cavity was the preferred one in the simulations involving the genetic algorithm, as the greater coupling coefficient allowed greater reflectivities with smaller number of layers.

A great deal of integrated cavities produced at the beginning of the Continuum project was studied by Xunqi Wu in his PhD thesis [19], especially in experiments reviewing the benefits of apodized gratings. But one particular experience described at the end of its PhD manuscript caught our attention and made us re-consider it in the new light of the new experiments (described in Section 5.1.3) on hybrid cavities.

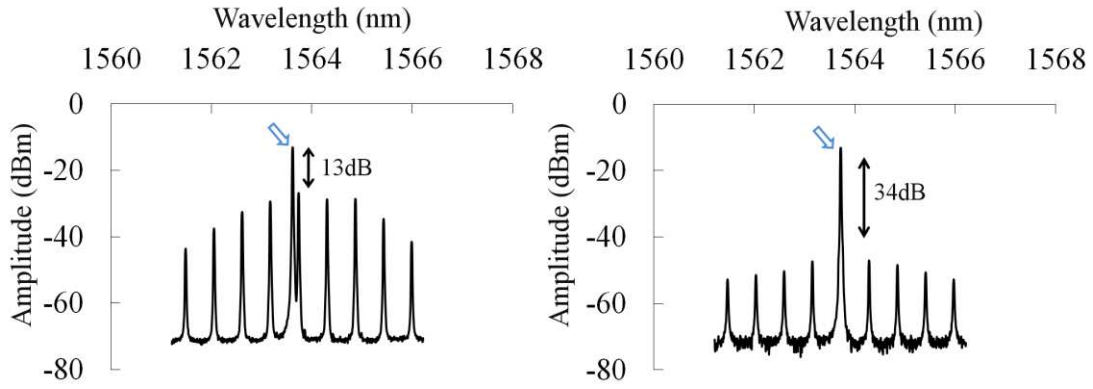

Fig. 5.8 Plots showing the injection locking phenomenon observed in the integrated cavities experiments of Wu. At the left the external laser (blue flash) is not close enough to a cavity peak to lock it, while at the right the cavity emission drops abruptly as a consequence of the locking. The SMSR increases from left (13dB) to right (34dB) as a consequence of the locking.

5.2.1 Amplifier

In that experience, an external laser is injected inside a resonant cavity realized on InP. Firstly, the Fabry-Perot specter of the cavity will be easily distinguished with an optical spectrum analyzer, as the distance between the modes will be wide enough. The external laser is then injected at equal distance between two consecutive modes of the cavity and the difference (called SMSR: Single Mode Suppression Ration) between its amplitude and the amplitude of the nearest cavity modes is measured. The external laser will then be shifted toward one of the cavity modes. The SMSR will keep constant until a certain distance between the external laser and the cavity mode is reached. At that point the cavity emission will shift so that the nearest cavity mode will be assimilated into the external laser emission. The SMSR (measured now as the difference between the external laser and the next closest cavity mode) will suddenly rise. This phenomenon of shifting the cavity emission by using an external laser is called injection locking. The shifting appears simultaneously with a sudden drop in the cavity emission, which translates into a rise of the SMSR. Figure 5.8 shows a set of the measurements on an integrated cavity done by Wu. The rise of SMSR is obvious as the cavity passes from the unlocked (left) to the locked state (right).

In the literature [52-54] the injection locking effect has found applications in improving the modulation efficiency or the operation bandwidth of locked (slave)

lasers. All the applications are related to improving one or other characteristic in slave lasers. Once with the experiment of Wu, it may become possible in fact to act not to improve the slave laser (the one which is locked) but the external master laser (the one which is locking). More precisely, it may become possible to amplify the external laser when the cavity laser is locked into it, similar to the experience described in section 5.1.3 for a hybrid cavity. Sadly, the experiments of Wu [19] offer us information only on the variation of the SMSR with the injected power, when the lasers are already in the locked state. It does not go into details regarding the absolute amplification of a master laser after it locks a Fabry-Perot laser. Figure 5.8 is the only set of measurements that records the evolution from the unlocked to the locked state. Judging from it, one would notice that the master laser (blue flash) will keep almost the same amplitude when passing from the unlocked into the locked state, while the cavity modes will drop altogether. There are however no other experiments to document the effects of this transition on the master laser.

When Wu realized the above experiment there were no indications on the eventual amplification that a maser laser could benefit from, when in the locking state. Meanwhile, the amplification observed while experimenting with external optical injection in a hybrid cavity (section 5.1.3) led us to review the experiments of Wu on integrated cavities in a new light. It is our opinion now that if different powers had been used, the same degree of amplification would have been obtained as for the hybrid cavity, with the advantage of greater stability.

Chapter 6

Conclusions and Perspectives

6.1 Conclusions

The theoretical part of this manuscript was focused on finding new simple alternatives to Supercontinuum sources in WDM applications. Chapter 2 detailed the novel idea of the Continuum projected, aimed at creating a resonant cavity capable of producing a large continuum spectrum over the entire C-band. This cavity was going to have one of the metallic reflectors replaced by a linearly chirped grating (LCG) having the role of canceling or enlarging the resonant modes of the cavity.

Chapter 3 firstly finds the necessary and sufficient condition for a LCG to enlarge the modes of a resonant cavity. Then it presents a series of simulations on all technologically realizable LCGs, in search of a grating possessing the required characteristics. Three parameters have been varied when searching for a suitable LCG, with no real success. It was shown the group time delay (*GTD*) of a LCG is proportional to the chirp and the length of a grating and inversely proportional to its coupling coefficient. It was found that the GTD is always positive in the reflection bandwidth of the LCG. This is the first study of the variation of the GTD with the parameters of a LCG.

In Chapter 4 the idea of resonant modes enlargement is tested on random-width gratings. As an exhaustive search of all random gratings would have been impossible, a novel idea was to adapt a genetic synthesis method (specifically created for continuous gratings) to generate discrete-layer gratings. We decided applying a

genetic algorithm on some initial small random populations to synthesize new structures according to our needs. In terms of performance, the gratings thus synthesized were scoring much higher than any other grating coming from populations (even much larger) on which the genetic algorithm has not been applied. The InP structures were considered more suited than the fiber ones as reflectors for resonant cavities. Finally, at the end of the section on the genetic algorithm, the influence of such a genetic grating on the spectrum of a resonant cavity is being analyzed. A mode enlargement of around *15nm* was noticed using such a structure. At the end of the chapter, the results after using a second synthesis method (DLP) are presented. At this point it becomes apparent that the principle of causality may be the culprit for which a perfect continuum reflector could never be constructed.

The experimental part of the thesis is concerned with finding new applications for resonant cavities formed between LCGs. Adding a tunable filter in such a cavity will create a tunable laser. This type of application is the most suited for such resonant structures, as confirmed by earlier experiences of Bergonzo *et al.* The cavity formed between LCGs was also tested as a resonant amplifier for different levels of an external signal. For low powers of an external carrier, the amplification reached good levels but was instable, while for powerful carriers, the amplification was stable, but negative.

6.2 Perspectives

The typical emission generated by a resonant continuum cavity formed with a genetic grating was shown in Fig. 4.12(b). In the simulations the active gain was considered uniform along all wavelengths. Other gain functions will further more be able to equalize the shape of the emission.

As this was the first time a genetic algorithm was used for the synthesis of a discrete-layer grating, its use may be extended for other applications concerning this type of gratings. This may be the case for the Bragg reflectors of a VCSEL.

Finally, regarding the practical use of a resonant cavity formed between LCGs as an amplifier, the external lasers used in our study did not contain any signal. A study detailing the effects of a resonant amplifier on the modulation bandwidth or

modulation efficiency of a master carrier containing different signal frequencies would also be interesting. In past research of the effects of injection locking on signal modulation, the signal was always contained in the slave laser. Translating the signal onto the master laser would be thus a novel approach.

References

[1] United States Federal Standard 1037C: Glossary of Telecommunications Terms, http://www.its.bldrdoc.gov/fs-1037/fs-1037c.htm

[2] J. Jacquet and G. H. Duan, "Continuum Laser Cavity: Concept and Applications," Continuum Project Submission Document B, 2009

[3] R. R. Alfano, "The Supercontinuum Laser Source: Fundamentals with Updated References" (Springer, 2006), 2nd ed.

[4] R. R. Alfano and S. L. Shapiro, "Emission in the region 4000 to 7000 Å via four-photon coupling in glass," Physical Rev. Lett. 24, P 584-587 (1970)

[5] J.W. Nicholson, A.K. Abeeluck, C. Headley, M.F. Yan, C.G. Jorgensen, "Pulsed and continuous-wave supercontinuum generation in highly nonlinear, dispersion-shifted fibers," Applied Physics B, June 2003

[6] C. Lin and R. H. Stolen, "New nanosecond continuum for excited-state spectroscopy," Appl. Phys. Lett. 28, P 216-218 (1976)

[7] B. Kibler, B. Barviau, C. Michel, G. Millot, and A. Picozzi, "Thermodynamic approach of supercontinuum generation", Optical Fiber Technology 18, P 257-267, 2012

[8] G. Genty, S. Coen, and J. M. Dudley, "Fiber supercontinuum sources", J. Opt. Soc. Am. B, Vol. 24, No. 8, P 1771-1785, August 2007

[9] R. R. Alfano and S. L. Shapiro, "Observation of self-phase modulation and small-scale filaments in crystals and glasses," Phys. Rev. Lett. 24, 592–594 (1970)

[10] R. R. Alfano and S. L. Shapiro, "Direct distortion of electronic clouds of rare-gas atoms in intense electric fields," Phys. Rev. Lett. 24, 1217–1220 (1970)

[11] Hartl, I., X.D. Li, C. Chudoba, R.K. Ghanta, T.H. Ko, J.G. Fujimoto, J.K. Ranka, and R.S. Windeler (2001), "Ultrahigh-resolution optical coherence tomography using continuum generation in an air–silica microstructure optical fiber," Opt. Lett.26, No. 9, 608

[12] Diddams, S.A., A. Bartels, T.M. Ramond, C.W. Oates, S. Bize, E.A. Curtis, J.C. Bergquist, and L. Hollberg (2003), "Design and control of femtosecond lasers for optical clocks and the synthesis of low-noise optical and microwave signals," IEEE J. Sel. Topics Quantum Electron.9, No. 4, 1072

[13] Baltuska, A., T. Fuji, and T. Kobayashi (2002), "Visible pulse compression to 4 fs by optical parametrical amplification and programmable dispersion control," Opt. Lett. 27, 306–308

[14] Takara, H. (2002) "Multiple optical carrier generation from a supercontinuum source," Opt. Photon. News 13, No. 3, 48

[15] M. S. Leeson , B. Luo, and A. J. Robinson "Spectral Slicing for Data Communications", Proceedings Symposium IEEE/LEOS Benelux Chapter, 2006, Eindhoven

[16] C. Ware, S. Cordette, C. Lepers, I. Fsaifes, B. Kibler, C. Finot, G. Millot, "Spectral slicing of a supercontinuum source fpr WDM/DS-OCDMA application", Proceedings of ICTON 2008, Vol. 4, P 158-161

[17] T. Yamatoya, S. Sekiguchi, and K. Iga, "High-Power CW Operation of GaInAsP/InP Superluminescent Light-Emitting Diode with Tapered Active Region", Jpn. J. Appl. Physics, vol. 40, no. 7A, pp. L678-L680, 2001

[18] J. Kani, K. Iwatsuki, and T. Imai, "Optical multiplexing technologies for access-area applications", IEEE J. Sel. Topics in Quantum Electronics, vol. 12, no. 4, P 661-668, 2006

[19] Xunqi Wu, "Etude de cavités optiques formées de miroirs de Bragg à réseaux à pas variable: application aux filtres et lasers", PhD thesis

[20] A. Bergonzo, E. Gohin, J. Landreau, O. Durand, R. Brenot, G-H. Duan, and J. Jacquet, "Tuning Range Extension by Active Mode-Locking of External Cavity Laser Including a Linearly Chirped Fiber Bragg Grating", IEEE Journal of Selected Topic in Quantum Electronics, Vol. 9, n°5, P 1118, September/October (2003)

[21] A. Bergonzo, J. Jacquet, D. de Gaudemaris, J. Lendreau, A. Plais, A. Vuong, H. Sillard, T. Fillion, O. Durand, H. Krol, A. Accard & I. Riant, "Widely Vernier Tunable External Cavity Laser including a Sampled Fibre Bragg Grating with Digital Wavelength Selection*",* IEEE Photonics Technology Letters, Vol 15, n°8, Page 1144-1146, August 2003

[22] Supercontinuum Generation in Photonic Crystal Fibres, NKT Photonics A/S 2013, http://www.nktphotonics.com/supercontinuum

[23] Richard Ramsay, "Photonic-crystal fiber characteristics benefit numerous applications", 17 November 2008, SPIE Newsroom, DOI: 10.1117/2.1200811.1371

[24] Francois Ouellette, "Dispersion cancellation using linearly chirped Bragg grating filters in optical waveguides," Optics Letters, Vol. 12, Issue 10, pp. 847-849 (1987)

[25] K. Ennser, M. N. Zervas, and R. I. Laming, "Optimization of apodized linearly chirpd fiber gratings for optical communications", IEEE J. Quantum Electron, 34, pp 770-778 (1998)

[26] J. Skaar, "Synthesis and characterization of fiber Bragg gratings", PhD thesis, November 2000

[27] C.B. Parker, "McGraw Hill Encyclopaedia of Physics (2nd Edition)," McGraw Hill, 1994

[28] Kenneth O. Hill and Gerald Meltz, "Fiber Bragg Grating Technology Fundamentals and Overview", Journal of Lightwave Technology, Vol. 15, No. 8, August1997, 1263

[29] F. Ouellette, "Fiber Bragg Gratings help WDM push limits of fiber capacity", Laser Focus World, pp. 83-89, March 1998

[30] A. D. Kersay, M. A. Davis, H. K. Patrick, M. LeBlanc, K. P. Koo, C. G. Askins, M. A. Putnam, "Fiber grating sensors", Journal of Lightwave Technology, vol. 15, pp. 1442-1463, 1997

[31] İsa Navruz, Ahmet Altuncu, "Design of chirped fiber Bragg grating for use in wideband dispersion compensation," Proceedings of New Trends in Computer Networks, 2005

[32] Patrice Mégret, Sébastien Bette, Cathy Crunelle, Christophe Caucheteur, "Fiber Bragg Gratings: fundamentals and applications," Doctoral School, May 2007

[33] Xavier Chapeleau, Dominique Leduc, Cyril Lupi, Francisco López-Gejo, Marc Douay, Roger Le Ny, and Christian Boisrobert, "Local characterization of fiber-Bragg gratings through combined use of low-coherence interferometry and a layer-peeling algorithm", Appl. Opt. 45, 728-735 (2006)

[34] C. S. Hong, J. B. Shellan, A. C. Livanos, A. Yariv, and A. Katzir, "Broad-band grating filters for thin-film optical waveguides", Appl. Phys. Lett. 31, 276 (1977)

[35] L. A. Weller-Brophy and D. G. Hall, "Analysis of waveguide gratings: application of Rouard's method", J. Opt. Soc. Am. A, 2, pp. 863-871 (1985)

[36] Raman Kashyap, "Fiber Bragg Gratings" (Academic Press, 2009)

[37] T. Erdogan, "Fiber grating spectra", Journal of Lightwave Technology, vol.15, no.8, pp. 1277-1294 (1997)

[38] G. Bjork and O. Nilsson, "A new exact and efficient numerical matrix theory of complicated laser structures: Properties of Asymmetric Phase-Shifted DFB Lasers", Journal of Lightwave Technology, Vol. LT-5, No. 1, P 140, January 1987

[39] E. Peral, J. Capmany, and J. Marti, “Iterative solution to the Gel’fand-Levitan-Marchenko equations and application to synthesis of fiber gratings,” IEEE J. Quantum Electronics 32, 2078—2084 (1996)

[40] J. Skaar and K. M. Risvik, “A Genetic Algorithm for the Inverse Problem in Synthesis of Fiber Gratings,” Journal of Lightwave Technology, vol. 16, no. 10, October 1998

[41] J. Skaar, L. Wang, and T. Erdogan, “On the Synthesis of Fiber Bragg Gratings by Layer Peeling,” IEEE Journal of Quantum Electronics, February 2001

[42] P. G. Verly, J. A. Dobrowolski, W. J. Wild and R. L. Burton, "Synthesis of high réjection filters with the Fourier transform method", Appl. Opt. 28, 2864-2875 (1989)

[43] J. H. Holland, “Adaption in Natural and Artificial Systems”, Cambridge, MA: The M.I.T. Press, 1975

[44] C. Darwin, “On the origin of species”, John Murray Publisher, 1859

[45] R. Dawkins, “The Selfish Gene”, Oxford University Press, 1976

[46] T. Zerjal *et al.*, “The Genetic Legacy of the Mongols”, The American Journal of Human Genetics, 72 (3), 717-721 DOI: 10.1086/367774

[47] Y. Xue *et al.*, Recent Spread of a Y-Crhomosomal Lineage in Northern China and Mongolia, The American Journal of Human Genetics, Vol. 77, Issue 6, 1112-1116, 1 December 2005

[48] L. T. Moore *et al.*, "A Y-Chromosome Signature of Hegemony in Gaelic Ireland", The American Journal of Human Genetics, Volume 78, Issue 2, 334-338, 1 February 2006

[49] R. Feced, M. N. Zervas and M.A. Muriel, “An efficient inverse scattering algorithm for the design of nonuniform fibre Bragg gratings,” J. Quantum El., vol. 35, 1999, pp. 1105–1115

[50] Smith, S. W., “The Scientist and Engineer Guide to Digital Signal Processing”, California Technical Publishing, 1997-2011

[51] H. Soda and H. Imai, "Analysis of the Spectrum Behavior Below the Threshold in DFB Lasers", IEEE Journal of Quantum Electronics, Vol. QE-22, No. 5, P 637, May 1986

[52] Erwin K. Lau, Hyuk-Kee Sung, and Ming C. Wu, "Frequency Response Enhancement of Optical Injection-Locked Lasers," IEEE Journal of Quantum Electronics, Vol. 44, No. 1, January 2008, P.90

[53] Hyuk-Kee Sung, Erwin K. Lau, and Ming C. Wu, "Optical Properties and Modulation Characteristics of Ultra-Strong Injection-Locked Distributed Feedback Lasers," IEEE Journal of Selected Topics in Quantum Electronics, Vol. 13, No. 5, September/October 2007, P. 1215

[54] Erwin K. Lau, Liang Jie Wong, and Ming C. Wu, "Enhanced Modulation Characteristics of Optical Injection-Locked Lasers: A Tutorial," IEEE Journal of Selected Topics in Quantum Electronics, Vol. 15, No. 3, may/june 2009, P. 618

[55] Wu, X., Jacquet, J., Duan, G., "Steep and flat bandpass filter using linearly chirpd and apodized fiber Bragg grating," Proceedings of SPIE Vol. 7598, 75981Y (2010)

[56] Wu, X., Jacquet, J., Duan, G., "Simulation analysis of a novel bandpass fiber filter," Proceedings of SPIE Vol. 7717, 771715 (2010)

[57] Wu, X., Jacquet, J., Duan, G., "Simulation analysis of a novel bandpass fiber filter," Proceedings of SPIE Vol. 7717, 771715 (2010)

List of Tables and Figures

Table 1.1 Success Criteria for the Continuum Project *35*

Fig. 1.1 Simple schematic of a passive optical cavity formed between two metallic mirrors (M1, M2). The light propagates between the mirrors through an optical fiber. This type of structure is also called a Fabry-Perot cavity *32*

Fig. 1.2 Transmission as a function of wavelength when the cavity of Fig. 1 is functioning as a filter with the reflectivities of the mirrors $R_1=R_2=0.8$. The distance between the mirrors is L=3cm *32*

Fig. 1.3 Simple schematic of an active optical cavity formed between two metallic mirrors (M_1, M_2). The active medium is a Semiconductor Optical Amplifier (SOA), which transforms the injected electrical energy into optical gain. *33*

Fig. 1.4 Comparison between a Fabry-Perot cavity (with its resonant modes) and a Continuum cavity (with its resonant enlarged mode) *34*

Fig. 2.1 Comparison between a typical Supercontinuum spectrum and the spectrum of the seed (source) laser used for its generation *41*

Fig. 2.2 Schematics of the first experimental arrangements used for the supercontinuum generation in the 1970s *42*

Fig. 2.3 Schematics of the way in which a supercontinuum source could be employed in WDM telecommunications *44*

Fig. 2.4 Comparison between the spectra of different types of light sources: He-Ne (Helium-Neon laser); Xenon lamp; ASE (Amplified Spontaneous Emission) Source; SLED (Superluminescent diode); Supercontinuum. For each source, only the effective power was considered (the level of generated power which can be coupled onto an optical fiber) *46*

Fig. 2.5 Representation of optical paths inside a Continuum cavity: different wavelengths will travel different optical paths, in function of the position in the LCG where their reflection takes place. Smaller wavelengths are represented in blue, whereas intermediate wavelengths are in green and small wavelengths are drawn in red *48*

Fig. 2.6 Representation of a type of continuous tunable laser formed with a LCG, inspired by the setup used by Bergonzo et al. The reflectivity characteristic of the LCG is represented in the insert above the grating *50*

Fig. 2.7 Representation of a Continuum cavity on fiber; the grating at the right side of the cavity is divided in its constituent layers. Each pair of different layers forms a Bragg period of the grating. The length of each period – represented in blue - is linearly increasing from left to right. The supposed optical paths of different wavelengths through the cavity are represented with black double arrows. *51*

Fig. 3.1 Variation of the refractive index (y-axis) of a linearly chirped grating realized on fiber. This grating has a chirp C=0.04 and a coupling coefficient $k=80cm^{-1}$ *56*

Fig. 3.2 Schematic representation of a hybrid cavity formed between a metallic mirror and a LCG. The active medium consists of a SOA. The name "hybrid" comes from the fact that a SOA is inserted inside the fiber structure. *58*

Fig. 3.3 Schematic representation of a die with 11 integrated cavities is drawn to the left. The LCGs are represented with the color red. At the right, a zoom into the structure of an integrated cavity (top) is presented. Also at the right a photo of a series of four Bragg gratings is displayed with the courtesy of Alcatel. 59

Fig. 3.4 Schematic representation of the transfer matrix method which was used in this manuscript to numerically solve the spectral response of gratings; a random structure of layers is used for exemplification, as the algorithm could be used for any type of discrete layer grating. 63

Fig. 3.5 Representation of a resonant cavity realized with a LCG, in which the total round trip phase shift has been divided between the Bragg grating (φ_{BG}) and the rest of the cavity (φ_{FP}). 65

Fig. 3.6 Influence of the chirp on the group time delay (GTD) of a LCFBG of length L=1cm and coupling coefficient of: a. k = 100cm^{-1} and b. k = 1cm^{-1}. The GTD is represented by a black pointed line and the reflectivity in a dashed blue line. Both the reflectivities and the GTDs are calculated for λ=1550nm at the center of the grating's bandwidth. 69

Fig. 3.7 Influence of the coupling coefficient k on the group time delay (GTD) of a LCFBG of length L=1cm and chirp: a. C=100nm/cm and b. C=0.1nm/cm. The GTD plot is colored black, while the reflectivity values are in blue. The values are calculated for the center of the grating's bandwidth. 70

Fig. 3.8 Influence of the chirp's sign on the group time delay (GTD) of a LCFBG of length L=1cm. The variation of GTD with k is studied for two different gratings with chirps C=100nm/cm (black) and C=−100nm/cm (blue). 71

Fig. 3.9 Influence of the grating's length on the group time delay (black) and central reflectivity (blue) of a fiber LCG of chirp C=100nm/cm and coupling coefficient k=100cm^{-1}. 72

Fig. 3.10 Influence of the grating's medium on the group time delay (GTD) of a LCG of length L=1cm. The integrated grating is represented in blue, while the fiber LCG is in black. A coupling coefficient of 1000cm^{-1} was used for the InP grating, while for the fiber one a k=100cm^{-1} was used. 72

Fig. 4.1 Three examples of different types of InP random gratings: a) a grating in which the width of each layer is random; b) a grating in which the refractive index of each layer has a random value; c) a grating in which both the width and the refractive index of each layer are random. 76

Fig. 4.2 Diagram of the genetic algorithm used throughout this manuscript for the generation of Bragg gratings. 81

Fig. 4.3 Spectrum of an individual grating, along with the mesh used for the calculation of the fitness function corresponding to that individual grating. 82

Fig. 4.4 Generation of two child-gratings after applying the uniform crossover method on two parent-gratings 84

Fig. 4.5 Representation of the analogy between a digital filter and a Bragg grating for which all the layers have the same optical path length 86

Fig. 4.6 Example of a type of ideal response used as input for the DLP algorithm. The black pointed line represents the desired reflectivity, while the blue pointed one is the desired GTD 87

Fig. 4.7 Specter of a genetic grating obtained after 10 iterations by a genetic algorithm which searches for a steep negative GTD grating of 200 layers on InP. The reflectivity amplitude is shown in black, while the GTD in blue 89

Fig. 4.8 Comparison between the efficiencies of the genetic algorithm for the case of two populations of (a) fiber and (b) InP gratings. Both populations are comprised of gratings of M=200layers. To the top, the evolution of the best fitness value in function of the number of new generations created by the algorithm. To the bottom, the best spectra obtained in the 10^{th} new generation. 91

Fig. 4.9 The variation of the fitness-value of the fittest grating in a population of N = 1000 InP gratings in function of the number of layers of the gratings in that population. The black line is for the initial random population, while the grey line corresponds to the 10^{th} generation created by a genetic algorithm (G.A.). 93

Fig. 4.10 Results after running the genetic algorithm on a population of N=1000 gratings of M=1000 layers each: to the left, the evolution of the best fitness value in function of the number of new generations created by the algorithm; to the right, the best spectrum obtained after 10 iterations of the genetic algorithm. In the plot at right, the reflection amplitude is represented in black, while the GTD in function of wavelength is displayed in blue. 93

Fig. 4.11 Refractive index variation of the 200-layer grating synthesized by the genetic algorithm and whose spectrum was plotted in Fig. 4.8(b) 94

Fig. 4.12 Reflection spectrum of a 200-layer genetic grating and the resonant emission of a continuum cavity formed with that grating as a mirror. 96

Fig. 4.13 Reflection spectrum of a 200-layer (100-period) uniform InP grating and the resonant emission of a resonant cavity formed with that grating as a mirror. The coupling coefficient of the grating is $k=1000cm^{-1}$. 96

Fig. 4.14 The group time delay of the synthesized structure (GTD_r) created by a DLP algorithm, when it is fed with different ideal responses having different desired GTD (GTD_d). 98

Fig. 5.1 The hybrid cavity model used in the experimental measurements. The metallic mirror which formerly bordered one side of the cavity was replaced by a second identical LCG. 102

Fig. 5.2 Plots showing typical spectral characteristics of SOA and LCG. To the left, the amplification of the SOA in function of wavelength is plotted for different source currents and for very low levels of signal power. To the right, the reflectivity amplitude of the LCG is measured in function of the wavelength. The LCG is a fiber grating of chirp C=100nm/cm, coupling coefficient $k=80cm^{-1}$ and R=50%.. 103

Fig. 5.3 Schematic of a tunable laser formed between two LCG. Inside the cavity a filter is used to manually set up the desired wavelength.. 104

Fig. 5.4 Figure showing superposed emission spectra obtained by manually adjusting the filter of Fig. 5.3 for different wavelengths of the ITU grid. 104

Fig. 5.5 Superposed emission spectra of the cavity in Fig. 5.3 when an external laser is injected inside the cavity: a. no external power (black); b. 3mW external power (blue); c. 5mW external power (red).....105

Fig. 5.6 Electrical spectra plotted by a fast photodiode receiving as input the optical radiation exiting the cavity of Fig. 5.3. An external laser is injected into the cavity from the other side, having: a. no external power (black); b. 3mW external power (blue); c. 5mW external power (red).....106

Fig. 5.7 Plots showing amplitude of the external laser in function of wavelength, after passing through the resonant amplifier of Fig. 5.1. Two different levels (marked in a red dashed line) of the external laser have been used as inputs: a. 0.5mW; b.10mW. 108

Fig. 5.8 Plots showing the injection locking phenomenon observed in the integrated cavities experiments of Wu. At the left the external laser (blue flash) is not close enough to a cavity peak to lock it, while at the right the cavity emission drops abruptly as a consequence of the locking. The SMSR increases from left (13dB) to right (34dB) as a consequence of the locking. 111

Symbols and Abbreviations

BG − Bragg Grating

DLP – Discrete Layer Peeling

FP – Fabry-Perot

FSR − Free Spectral Range

GA – Genetic Algorithm

GTD – Group Time Delay

KDP − Potassium Dihydrogen Phosphate

LCBG or LCG − Linearly Chirped (Bragg) Grating

LCFBG − Linearly Chirped Fiber Bragg Grating

PCF − Photonic Crystal Fiber

RF – Radiofrequency

SC − Supercontinuum

SOA − Semiconductor Optical Amplifier

TMM – Transfer Matrix Method

WDM − Wavelength Division Multiplexing

λ_0 – Wavelength corresponding to the first Bragg period of a LCG

Λ_0 – First Bragg period of a LCG

Λ, Λ_B – Bragg period

L_0 – Length of the resonant cavity

L – Length of the grating

n_0 – Refractive index of the resonant cavity

n_{eff} – Effective refractive index of the grating

n_1 – Refractive index of odd layers in genetic structures

n_2 – Refractive index of even layers in genetic structures

m – Mode number, supposed constant for all wavelengths of a Continuum spectrum

z – Longitudinal axis of the grating

$z(\lambda_k)$ – Coordinate of the reflection plane for a wavelength λ_k

$z_{eff}(\lambda)$ – Coordinate of the effective reflection plane for a wavelength λ_k

C_Λ – Physical chirp of a grating, considered constant for a LCG

C_λ – Spectral chirp of a grating, considered constant for a LCG

q – Complex coupling coefficient

k – Modulus of the coupling coefficient

c – Speed of light

$u(z)$, $v(z)$ – Amplitude of the forward, respectively backward propagating waves

β – Propagating constant

$r(\lambda)$, $t(\lambda)$ – Reflection and transmission coefficients

R – Reflectivity of a grating, equal to $r(\lambda)\cdot r^*(\lambda)$

P_j, I_j – Propagating and Interface matrices

B – Grating's reflection bandwidth

F – Fitness function

f_i – Value returned by applying the fitness function F to a grating

N – Number of gratings in a population

M – Number of layers in each grating

$w_{i,j}$ – Widths of the layers of a random grating

f_{max} – Maximum value of the fitness function in a certain grating-population

GRIGORE ADRIAN IORDACHESCU

M, Born 06th of August 1984
Virgil Tempeanu nr 7, Pitesti, Romania
Phone: +40740015024
E-mail: adi_iord@yahoo.com

EXPERIENCE

Since October 2010	PhD Student SUPELEC, 57070 Metz, France *Synthesis of enlarged resonance optical cavities formed between chirped Bragg gratings*
November 2009 to June 2010	Internship SUPELEC, 57070 Metz, France *Study of Linearly Chirped Gratings*
November 2008 to May 2009	Internship OPTOELECRONICA, Magurele, Romania *Analyze of different fiber laser patents*
March 2008 to July 2008	Internship SUPELEC, 57070 Metz, France Matlab implementation of a tunneling current model for different media

EDUCATION

2008 to 2010	Master in Optoelectronics Polytechnic University of Bucharest *Graduation: 9,81(2nd out of 14 graduates)*
2003 to 2008	Bachelor of Engineering in Micro-technologies Polytechnic University of Bucharest *Graduation: 9.39 (2nd out of 62 graduates)*
1999 to 2003	I.C. Bratianu National Highschool - Pitesti Intensive Math and Computers Class *Graduation: 9.74 / Bacalaureat: 9.48*
Distinctions	1st Prize at National Astronomy Olympiad 2003 2nd Prize at National Physics Olympiad 2001 3rd Prize at National Physics Olympiad 2000

ABILITIES

Foreign Languages	Writing	Speaking	Reading
English	Advanced	Advanced	Advanced
French	Medium	Advanced	Advanced

Computer Programming	C++	Java	Perl	ASMx86	Matlab
	Labview	Verilog	JavaScript	PHP	MySQL

Other Interests	Photography	Web design	Skating
	Video editing	Astronomy	Travelling

Communications

[1] G.A. Iordachescu, X. Wu, J. Jacquet - *Synthesis of Negative Group Time Delay Bragg Gratings for Continuum Generation*. **Proceedings of NUSOD 2011** Rome, 5-8 September 2011

[2] G.A. Iordachescu, X.Q. Wu, J. Jacquet - *Broad-band laser emission and optical mode-locking of a Fabry-Perot laser formed between two Linearly Chirped Fiber Bragg Gratings*. **Proceedings of SPIE 2012 San Francisco**, 21-26 January 2012

[3] G.A. Iordachescu, J. Jacquet - *Design of Bragg gratings having negative group time delay for continuum generation*. **Proceedings of SPIE 2012 San Francisco**, 21-26 January 2012

[4] J. Jacquet, X. Wu, G. A. Iordachescu, « *CONTINUUM : un nouveau concept de laser à cavité intégrée incluant un miroir de bragg à pas variable ",* **INTERREG IV A NANODATA** JOURNEES SUR LES NANOTECHNOLOGIES, Poster n°18, Metz (France), (2010 – 11 – 24)

[5] J. Jacquet, G.H. Duan, A. Garnache, G. Millot , X. Wu, A. Iordachescu « *Continuum : Concept de laser à cavitté CONTINUUM et ses applications",* **J3N 2010, Journées Nationales en nanosciences et en Nanotechnologies,** Lille (France), (2010 – 11 – 8)

[6] J. Jacquet, G.H. Duan, A. Garnache, G. Millot, X. Wu, A. Iordachescu, « *Continuum : Concept de laser à cavité CONTINUUM et ses applications »*, **Conférence SEE – groupe Est**, Metz (France), September 2011

[7] G.A. Iordachescu, J. Jacquet – Verification of Continuum Condition for the case of Linearly Chirped Gratings – **ITSS Metz,** 3-9 Jully 2010 (ORAL)

[8] G.A. Iordachescu, J. Jacquet – Design of a Continuum Filter using Fiber Bragg Gratings Synthesis Algorithms – **ITSS Darmstadt,** 9-15 Jully 2011 (ORAL)

[9] A. Iordachescu, J. Jacquet – Continuum Gratings Design using the Genetic Algorithm – **European Doctorials Ventron,** 16-21 October 2011 (POSTER)